REACTIVELY SINTERED MOLYBDENUM DISILICIDE-BASED COMPOSITES
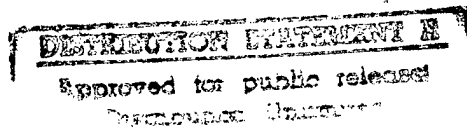
Final Report

submitted to

Dr. A.K. Vasudevan, Code 332

Office of Naval Research

Arlington, VA 22227

April, 1997

Principal Investigator

K.K. Chawla

Department of Materials & Met. Eng.
New Mexico Tech
Socorro, NM 87801

19971027 089

Abstract

The objective of this research was to identify the phases formed and determine some mechanical properties of reactively sintered $MoSi_2$ and $MoSi_2$ composites with carbon additions. The carbon additions were added via polymeric coatings on $MoSi_2$ particles. The purpose of adding carbon was to form silicon carbide particles (SiC_p) in situ and reduce the inherent presence of SiO_2 in $MoSi_2$. Carbon was added by two processes followed by pressureless sintering. The idea was to obtain a more uniform distribution of carbon by coating the $MoSi_2$ particles than by simply mixing carbon powder with $MoSi_2$ powder. The in situ formation of SiC_p would increase the low temperature toughness of $MoSi_2$ by using it as a reinforcement and also reduce the high temperature creep by reducing grain boundary sliding caused by viscous flow of SiO_2 at elevated temperatures.

The carbon coating of the $MoSi_2$ powder was obtained by: *p*henolic *r*esin *b*ased *c*arbon by *s*olvent *e*vaporation (PRBCSE) and *a*queous *d*ispersion *f*locculation (ADF). The sintering temperatures and times ranged from 1600 to 1800 °C and 1 to 100 h, respectively. The addition of carbon did reduce the presence of SiO_2 and there was formation of SiC_p. However, the SiC_p formation was less than expected and, therefore, did not increase toughness significantly. The Nowotny phase ($Mo_{\leq 4.8}Si_3C_{\leq 0.6}$) was also found in less than expected amounts.

Fracture toughness did not increase appreciably in the composite samples because a maximum of 1.4 vol% SiC_p was formed. But observation of crack/SiC_p interaction showed promise in that if a sufficient amount of SiC_p could be formed, an appreciable increase in toughness could result.

Table of Contents

List of Figures

List of Tables

x

1. Introduction

Molybdenum disilicide has been predominantly used for furnace heating elements, but recently there has been interest in its use for high temperature structural applications [1,2]. The reason for this increased interest stems from its desirable characteristics which are a high melting point, relatively low density, good oxidation resistance, relatively good thermal conductivity and is electrically conductive [1]. The melting point of $MoSi_2$ is approximately 2030 °C as compared to a melting point of 1340 °C for the Ni-based superalloys (See Table 1) [3,4]. This could potentially give $MoSi_2$ a big advantage over the Ni-based superalloys in turbine applications because the operating temperature can be increased resulting in an increase in turbine efficiency and reduced emissions. The relatively low density (6.25 g/cm^3) compared to the Ni-based superalloys (8.9 g/cm^3) is an important advantage in turbine applications because of the need for low weight [3]. Good oxidation resistance stems from the ability of $MoSi_2$ to form a protective SiO_2 surface layer when exposed to oxygen. Another advantageous feature of $MoSi_2$ is its thermal conductivity which is superior to Ni-based superalloys at low temperatures and comparable to the Ni-based superalloys at high temperatures. This allows heat to be

Table 1:   Comparison of the properties of $MoSi_2$ and Ni-based superalloys [3, 4].

Property	$MoSi_2$	Ni-based superalloy
Density (g/cm^3)	6.25	8.9
Melting Temperature (°C)	2030	1340
Resistance to oxidation	To 1500 °C	To 1175 °C uncoated To 1230 °C coated
Thermal Conductivity (W/cm K)	0.635 at R.T. 0.285 at 1100 °C	0.108 0.288
Thermal Expansion Coefficient (10^{-6} °C^{-1})	8.5 at 1200 °C	10 at 1200 °C
Elastic Modulus (GPa)	380	131

dissipated at a rate better than ceramics and comparable to metals. $MoSi_2$ is electrically conductive allowing it to be electro discharge machined. This is desirable since conventional ceramics are not generally conductive and thus cannot be machined in this way.

An important characteristic of $MoSi_2$ is its tendency to form SiO_2 when exposed to air [1, 5]. Although, in the case of a consolidated component, the ability of $MoSi_2$ to form a protective SiO_2 surface layer is advantageous, in the powder form the SiO_2 forms on the surface of almost all powder silicide particles [6]. The SiO_2 on the surface of the powder particles ends up at grain boundaries in the microstructure after consolidation, causing easy grain boundary sliding at elevated temperatures. This contributes to the low creep resistance at elevated temperatures. From a processing point of view one can eliminate the presence of the deleterious SiO_2 in the microstructure of the consolidated component by two methods. The first would be to simply minimize the exposure of the starting powder to air. This is not economically desirable because great care would have to be taken to avoid air exposure. The second route would be to eliminate the SiO_2 just before consolidation. Removing the SiO_2 using some sort of a cleansing process would have the same handling problems as before. But if an element could be added to the starting powder which would eliminate the SiO_2 and form a desirable phase one could produce a composite. Carbon is a prime candidate for such use because it could reduce SiO_2 by converting it to SiC particles (SiC_p). The SiC_p would be an excellent second phase because it is a high temperature refractory material that has been used as a reinforcement and it is thermodynamically stable with $MoSi_2$ [4, 7].

2

2. Objective

The objective of this research was to identify the phases and examine the microstructure of reactively sintered $MoSi_2$ and $MoSi_2$ with in situ additions of carbon. Microstructural analysis techniques were used on samples made with different starting powders and sintering conditions. Some mechanical characterization by Vickers hardness testing was also done.

3. Literature Review

3.1 General

As pointed out in Chapter 1, $MoSi_2$ is potentially an important structural material for use at high temperatures in air. A summary of some of the important characteristics is provided below.

Molybdenum disilicide has a tetragonal crystal structure (a = 0.3205 nm and c = 0.7845 nm), shown in fig. 1[8]. It can be described as a borderline ceramic-intermetallic because the atomic bonding is a mixture of covalent and metallic.
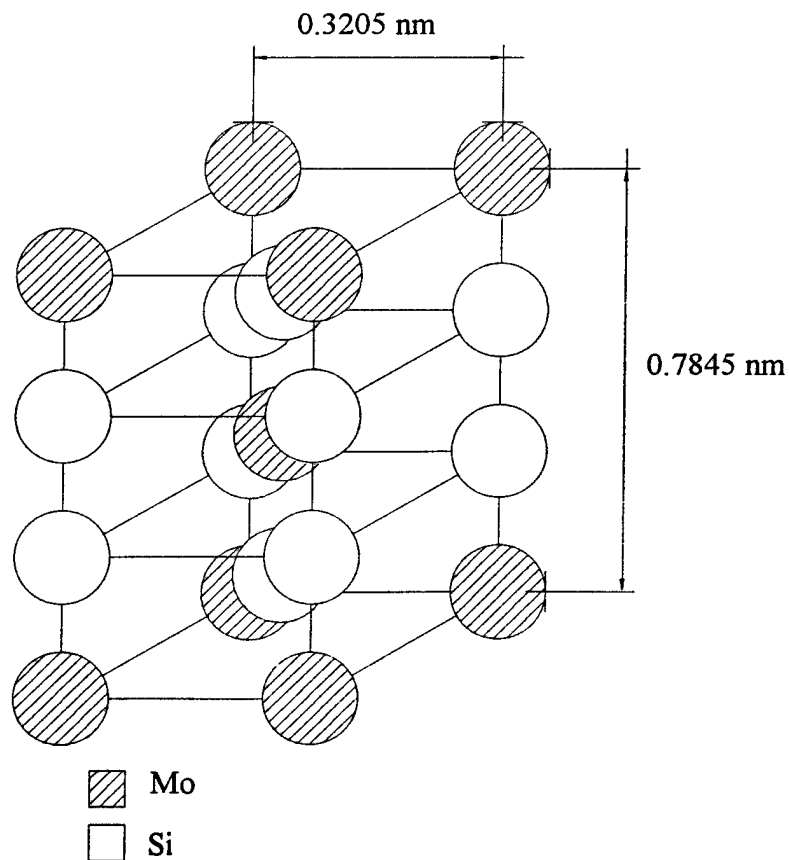
Figure 1:   Tetragonal I4/mmm unit cell of $MoSi_2$ [8].
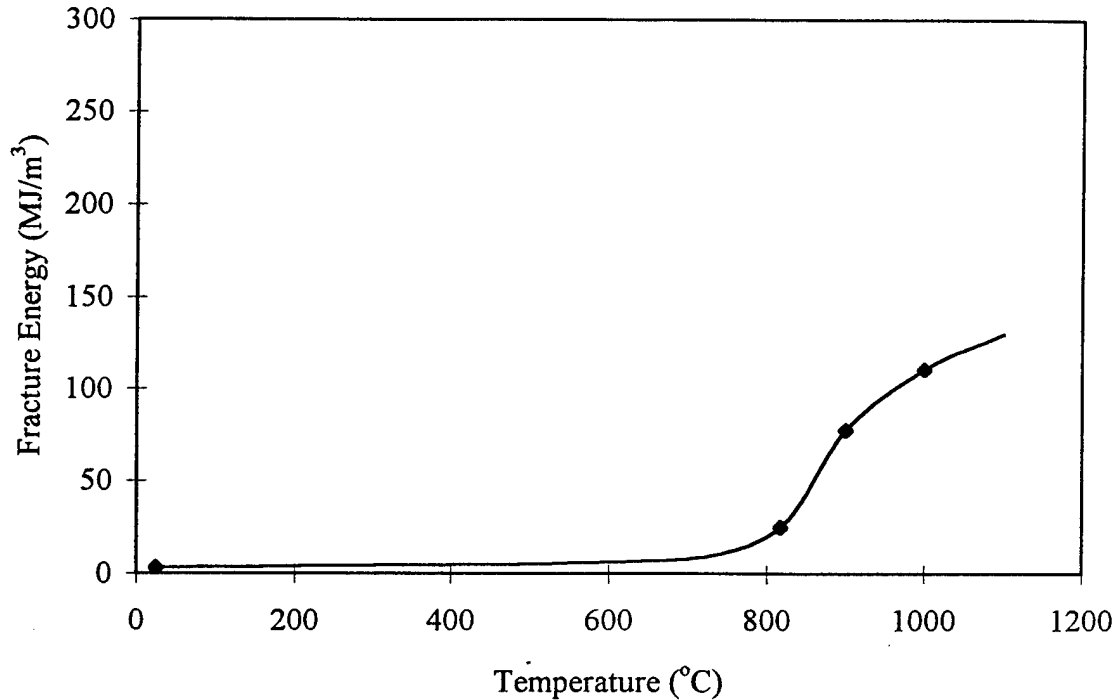
Figure 2: Fracture Energy vs. loading temperature for pure $MoSi_2$. Notice the fracture energy increases starting at 800 °C indicating the onset of the transition from brittle to ductile behavior [9].

3.1.1 Brittle-to-Ductile Transition Temperature

Molybdenum disilicide shows brittle failure at low temperatures and ductile failure at high temperatures. Its brittle-to-ductile transition temperature (BDTT) is approximately 1000 °C. Below the BDTT, strength is limited by brittle fracture and above the BDTT strength is limited by plastic flow [1]. Ghosh *et al.* [9] studied the ductility of $MoSi_2$ which was hot-pressed at a temperature of 1700 °C for 2 h under 28 MPa pressure followed by hot isostatic pressing (HIPing) at 1700 °C for 90 min under 200 MPa pressure. Figure 2 shows the fracture energy as a function of loading temperature obtained from compression tests done at temperatures ranging from room temperature to 1000 °C. The values were calculated from the area under the stress vs. strain curves. One

can clearly see the transition from brittle behavior (i.e., low fracture energy) to ductile behavior (i.e., high fracture energy).

3.1.2 Oxidation Problems: PEST

An oxidation phenomenon, called PEST, occurs in $MoSi_2$ at temperatures between approximately 400 and 600 °C. It was first discovered by Fitzer [10] in 1955. PEST causes $MoSi_2$ to completely disintegrate into a powder by the formation of MoO_3 at pores and preexisting cracks. PEST has been found to be directly related to the volatility of MoO_3 [11]. The disintegration is caused by the large volume changes in going from Mo to MoO_3 which corresponds to a volume increase of 340 % [11]. Since the MoO_3 is found at pores and preexisting cracks, it tends to wedge open pores and cracks causing more cracking eventually completely disintegrating the material.

3.1.3 Important Phases in Mo-Si and Mo-Si-C Systems

Crystallographic information of important phases in the Mo-Si and Mo-Si-C systems is given in Table 2. Silicide compounds have an affinity for O_2 resulting in the formation of amorphous silica (SiO_2) giving the silicide materials their excellent oxidation resistance. $MoSi_2$ forms SiO_2 and a Mo rich compound, Mo_5Si_3. Mo_5Si_3 is a refractory compound (m.p. = 2160 °C) with a tetragonal crystal structure. MoO_3 is an important compound in both systems because of its importance to the PEST phenomenon.

The Nowotny phase ($Mo_{\leq4.8}Si_3C_{\leq0.6}$) is a variable stoichiometry compound commonly found in Mo-Si-C ternary systems. The factors determining the variation have not been determined and relatively little is known about any of its properties. For this research the Nowotny phase is significant because it is one of the products of the reaction

6

Table 2:   Crystallographic information for relevant phases in the Mo-Si and Mo-Si-C systems.

Phase	Space Group	a (nm)	b (nm)	c (nm)
$MoSi_2$ [13]	I4/mmm	0.3205	-	0.7845
Mo_5Si_3 [13]	I4/mcm	0.9648	-	0.491
$Mo_{\leq4.8}Si_3C_{\leq0.6}$ [14]	$P6_3$/mcm	0.7286	-	0.5046
α-SiC [15]	$P6_3$mc	0.3073	-	0.1508
β-SiC [16]	F43m	0.4360	-	-
MoO_3 [17]	P21/c	0.7122	0.5374	0.5565

between $MoSi_2$ and C. This can be seen in the Mo-Si-C ternary phase diagram developed by Nowotny et al. [12], see fig. A1 in Appendix A.

3.2 Effects of Processing Temperature on MoSi₂

Wade and Petrovic [6] studied the effects of hot pressing temperature on the grain size, fracture toughness, Vickers hardness and mode of fracture (transgranular or intergranular) of $MoSi_2$. Their results are summarized in Table 3.

The grain size of $MoSi_2$ increased linearly with increasing hot-pressing temperature except for temperatures above 1800 °C where the grain size increased much faster. This was probably caused by the increased surface reactivity of $MoSi_2$ due to SiO(g) volatilization [6]. The SiO(g) was produced by the decomposition of SiO_2 at temperatures above approximately 1750 °C. Both the toughness and the hardness values decreased with increasing hot pressing temperature except for 1600 °C.

Table 3: Effect of hot-pressing temperature on the microstructural characteristics and mechanical properties of $MoSi_2$ [6].

Hot press Temperature (°C)	Grain Size (μm)	Fracture Toughness K_c (MPa m$^{0.5}$)	Vickers Hardness H_v (GPa)	Transgranular Fracture (%)	Intergranular Fracture (%)
1500	13.5	3.0	9.73	66.0	34.0
1600	15.3	3.6	9.87	70.9	29.1
1700	18.4	2.7	9.07	64.1	35.9
1800	20.5	3.0	9.08	67.3	32.7
1880	22.2	2.9	9.12	84.6	15.4
1920	31.9	2.3	8.92	97.0	3.0

The percentage of transgranular fracture increased linearly with hot-pressing temperature except for the 1920 °C sample where it increased rapidly. The transgranular fracture was thought to occur on weak cleavage planes, (110), in $MoSi_2$ [18].

Above approximately 1750 °C, solid Mo_5Si_3 was formed from $MoSi_2$. Above 1900 °C, a $MoSi_2$-Mo_5Si_3 eutectic liquid was formed [19,20]. The Mo_5Si_3 may have been the Nowotny phase, $Mo_{\leq4.8}Si_3C_{\leq0.6}$, but this was not verified experimentally.

3.3 Effects of Carbon on $MoSi_2$

Maloy et al. [21] studied hot-pressed $MoSi_2$ with carbon additions. The carbon was added in amounts of 1, 2, and 4 wt%. These samples were hot pressed at 1830 °C and 41.4 MPa. They observed that, as the amount of carbon increased, SiC formation increased while SiO_2 content decreased (Table 4). This was advantageous because SiC has a higher melting point than the spheroidization temperature of the SiO_2 (1700 °C) [22] and the elimination of SiO_2 would improve the creep resistance by minimizing grain boundary sliding. The disadvantage was that the carbon caused the material to become

Table 4: Effect of carbon additions on the formation of SiO_2 and SiC and the weight loss in $MoSi_2$ [21]. Large weight loss was attributed to the formation and volatilization of MoO_3.

wt% C	vol% SiO_2	vol% SiC	Weight Loss (%)
0	14	0	0
1	5	<5	0
2	1	8	20
4	<1	14	47

more porous and lose weight during hot pressing. The increased porosity and weight loss was attributed to the volatilization of MoO_3, a heavy and volatile oxide.

Figure 3 shows Vickers hardness as a function of temperature obtained from a high temperature Vickers hardness tester. The $MoSi_2$ with carbon showed higher hardness values at all temperatures compared to the monolithic $MoSi_2$. The increase in hardness was attributed to the increase in SiC content. Figure 4 shows the fracture toughness as a function of temperature obtained from four point bend tests. The fracture toughness increased with increasing carbon content. The $MoSi_2/SiC_p$ composite showed an increase in toughness with increasing temperature instead of a decrease as was the case with monolithic $MoSi_2$ (fig. 4). The increase in toughness was attributed to the reduction of SiO_2 at the grain boundary with the carbon addition which changed the cracking mode from intergranular to transgranular.

3.4 Oxidation of $MoSi_2$ Matrix Composites

Cook *et al.* [4] studied the high and low temperature isothermal oxidation, the thermal cycling behavior and the PEST phenomenon found in $MoSi_2$ and $MoSi_2$-based composites. The composite consisted of 30 vol% SiC and was then either HIPed or hot-pressed and then HIPed.

9
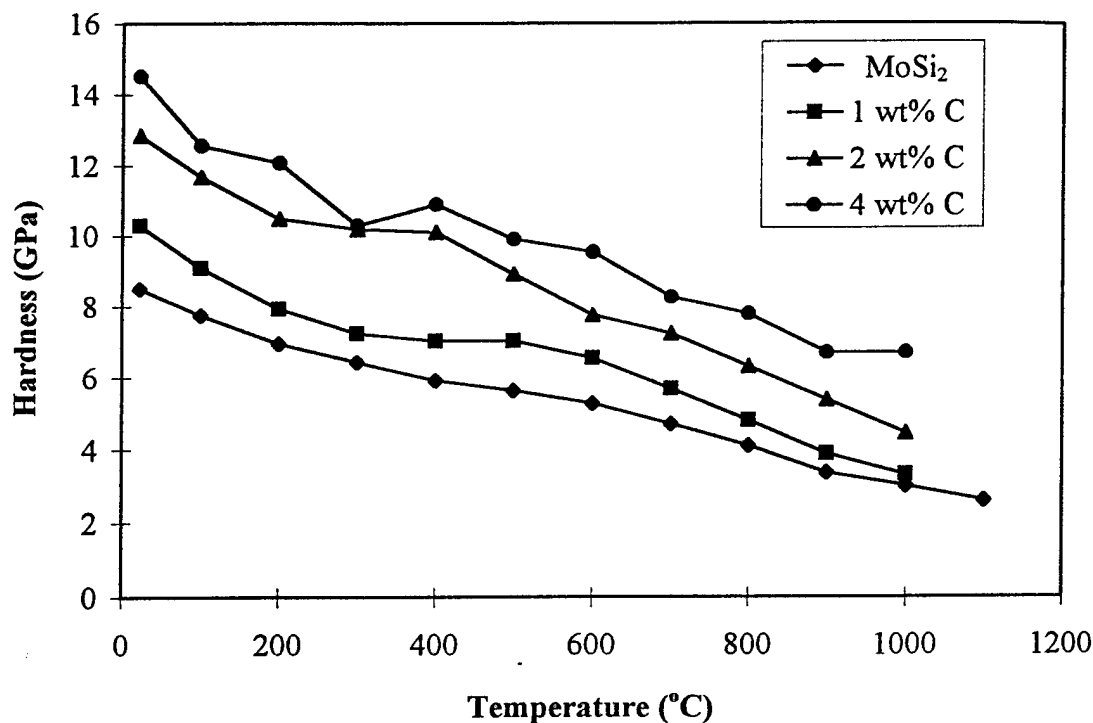
Figure 3: Effect of carbon additions on the hardness of $MoSi_2$ as a function of temperature [21]. Notice that the hardness increases with increasing carbon content.

The excellent oxidation resistance of $MoSi_2$ stems from its ability to form a protective layer of SiO_2 at temperatures below 1700 °C in air. But above 1700 °C the SiO_2 tended to spheroidize or ball-up which decreased the oxidation resistance above 1700 °C [22]. Below 1700 °C the SiO_2 coating was said to appear transparent and adherent to the composite. The high temperature oxidation (1700 °C>T>750 °C) of $MoSi_2$ was said to be controlled by the following reaction [23],

$$5 \ MoSi_2 + 7 \ O_2 \rightarrow Mo_5Si_3 + 7 \ SiO_2$$
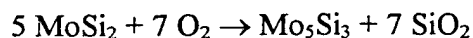
The low temperature (<750 °C) oxidation was said to be controlled by the following reaction [23],

$$2 \ MoSi_2 + 7 \ O_2 \rightarrow 2 \ MoO_3 + 4 \ SiO_2$$

10
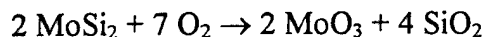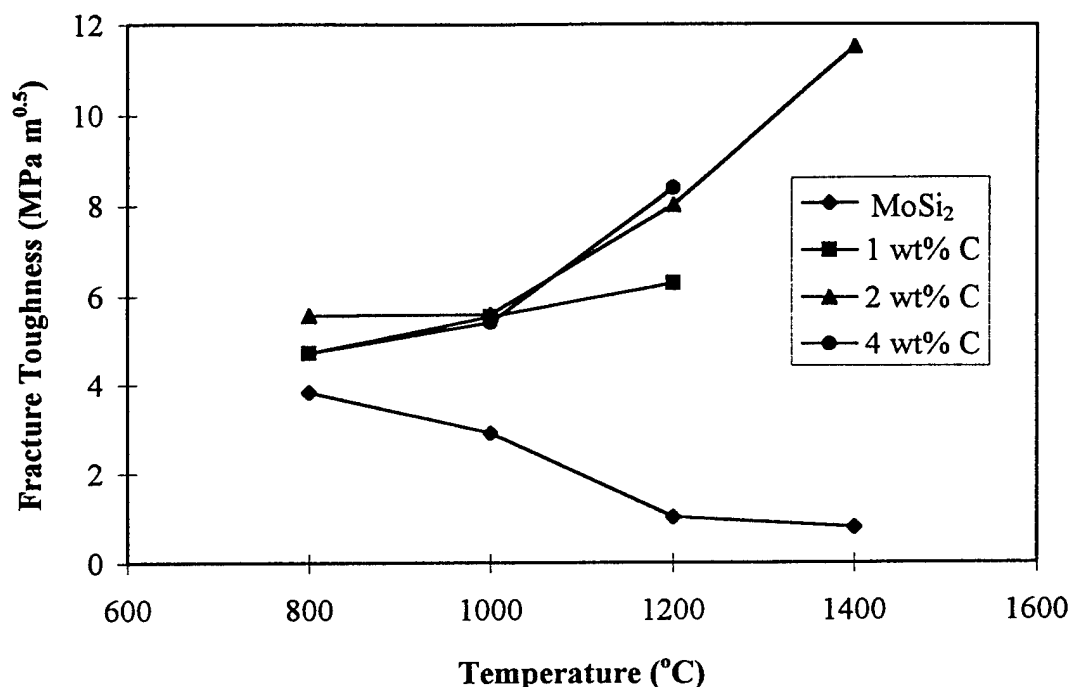
Figure 4: Effect of carbon additions on the fracture toughness as a function of temperature [21]. Notice that fracture toughness increases with carbon content and the fracture toughness increases with temperature for the samples with carbon additions.

This latter reaction is thought to be responsible for the PEST problem found in $MoSi_2$.

Thermogravimetric analysis was also done at 1500 °C for 48 h [4]. The results indicated that the square of the mass weight gain per unit area was a linear function of time (fig. 5). This implied that the oxidation rate was parabolic as a function of time which meant the oxidation was rate-limited by diffusion of oxygen ions through the SiO_2 surface layer. Figure 5 shows that the $MoSi_2$ with SiC exhibited a lower mass gain as a function of time than the monolithic $MoSi_2$ indicating an improved oxidation resistance.

Two cyclic oxidation experiments were then done in air by inserting the samples into a furnace (1200 °C and 1500 °C) for 55 min and then cooling down at room temperature for 5 min. This was done for 144 cycles. The results showed that both the reinforced and unreinforced samples showed minimal weight gain.

11
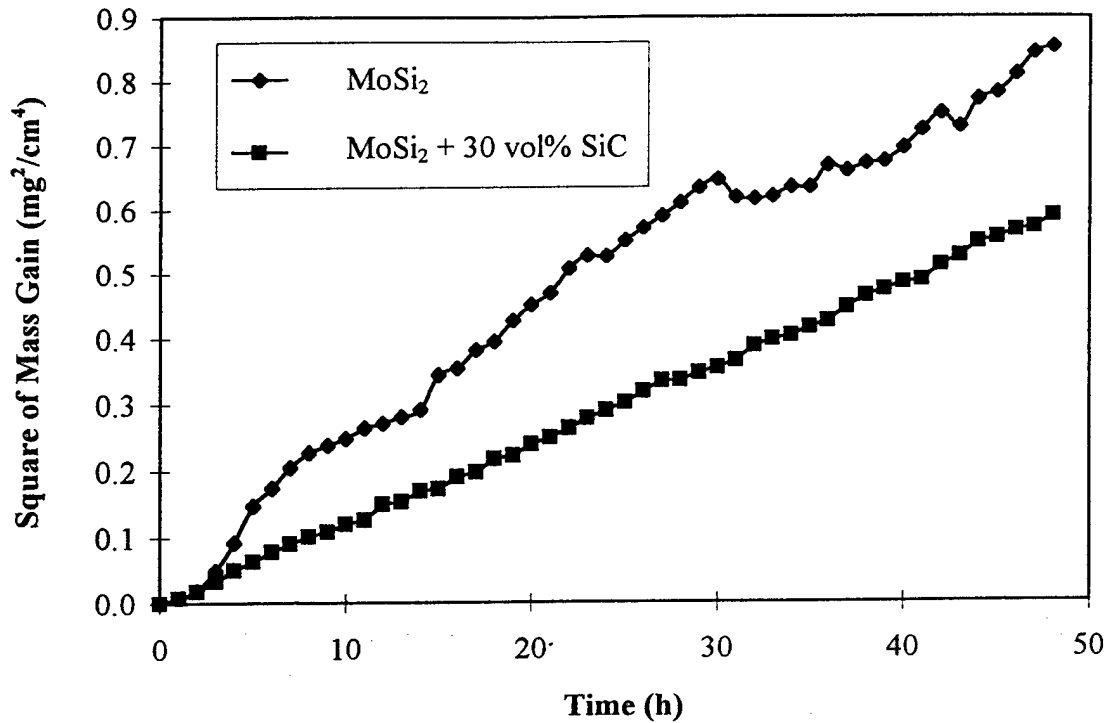
Figure 5: Thermogravimetric analysis of the square of the mass gain per unit area vs. time for monolithic $MoSi_2$ and $MoSi_2$ - 30 vol% SiC (1500 °C for 48 h) [4]. A linear relationship in the chart implies a parabolic oxidation indicating that oxygen is diffusing through the SiO_2 surface layer.

These samples were then exposed to 500 °C in air to induce PEST in the material. The results showed that the pure $MoSi_2$ had minimal weight loss after 160 h in the samples that were cycled at both 1200 °C and 1500 °C. The composite sample cycled at 1200 °C showed minimal weight loss during the PEST experiment, but the composite sample cycled at 1500 °C had just under 16 % weight gain and completely disintegrated before 160 h. This probably resulted from microcracking induced during thermal cycling from the thermal mismatch between SiC (α=4.8 10^{-6} K^{-1} at 1200 °C) and $MoSi_2$ (α=8.5 10^{-6} K^{-1} at 1200 °C) [4]. The microcracks produced during thermal cycling allowed O_2 to diffuse into the microcracks forming voluminous MoO_3 which tended to wedge open cracks

12
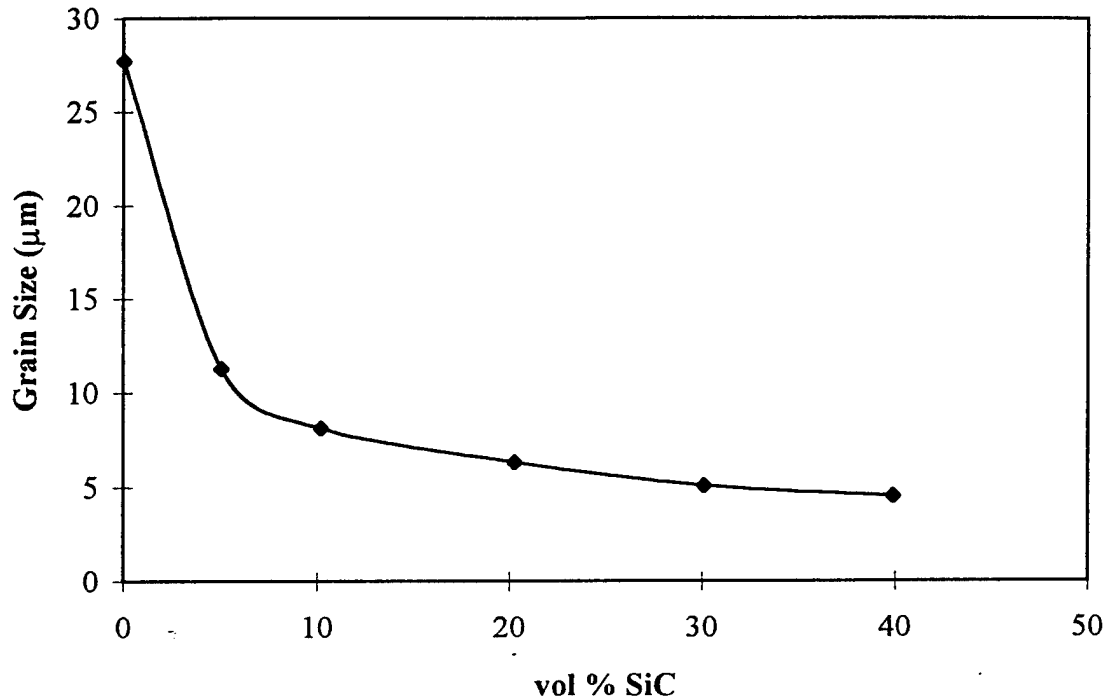
Figure 6: Variation of $MoSi_2$ grain size with increasing SiC_p content [7]. The grain size decreases with increasing SiC_p content indicating that the SiC_p inhibited grain growth.

exposing more of the internal $MoSi_2$ structure. This eventually lead to total disintegration of the material.

3.5 Properties of SiC Reinforced $MoSi_2$

Reinforcement of $MoSi_2$ with SiC_p was investigated by Bhattacharya and Petrovic [7]. The SiC_p content in the composites ranged from 0 to 40 vol%. These samples were hot pressed in argon at 1850 °C at a pressure of 30 MPa. The densities of the hot-pressed samples ranged from 93% to 96% of theoretical density. The grain size of the $MoSi_2$ matrix decreased with increasing SiC_p content (fig. 6) which indicated that the SiC_p inhibited the grain growth. Figure 6 also indicates that the effect of the SiC_p inhibiting grain growth stabilized at approximately 20 vol% SiC_p.

13
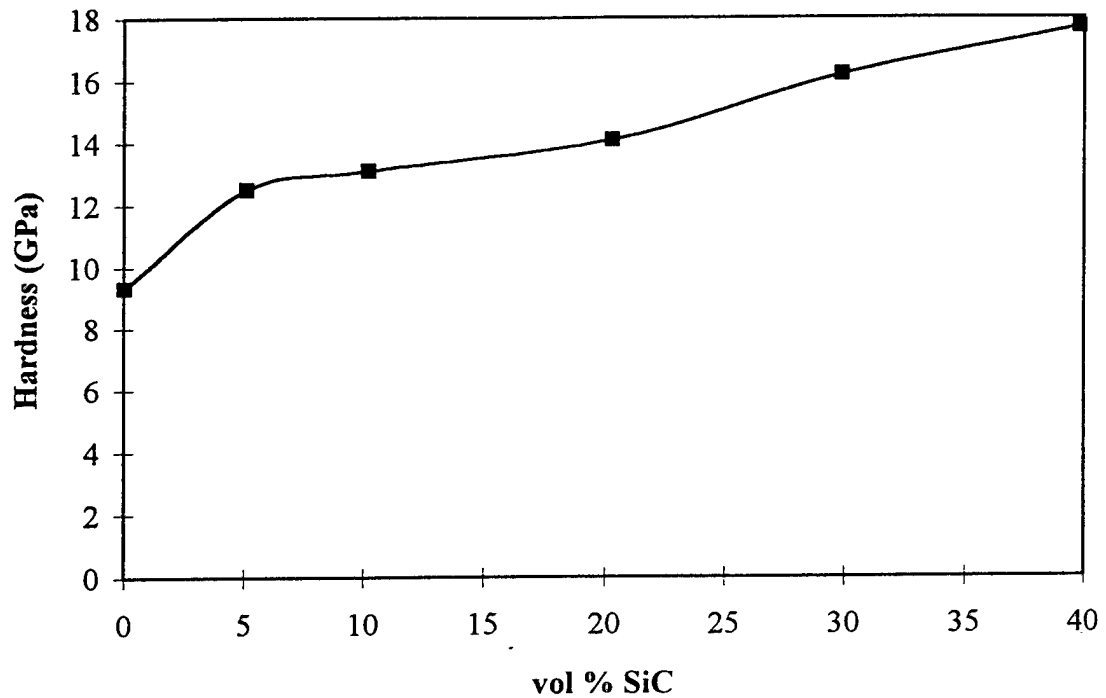
Figure 7:   Variation of MoSi$_2$ hardness with increasing SiC$_p$ content [7]. The hardness
increased with increasing SiC$_p$ content because of the presence of SiC$_p$ and
the smaller grain size found in the samples with SiC$_p$.

The hardness and fracture toughness of the composite increased with increasing

SiC$_p$ content as shown in figs. 7 and 8. Figure 7 shows that hardness increased with

increasing SiC content which was attributed to the presence of the SiC and a smaller grain

size with increasing SiC content. The monolithic MoSi$_2$ sample used in the fracture

toughness tests was hot pressed at 1600 °C, as opposed to 1850 °C, because the

indentation cracks were not well formed in the 1850 °C sample. Figure 8 also indicates

that the toughness reached a maximum value with the 40 vol% SiC$_p$ sample. The different

indentation crack lengths were obtained by varying the indentation loads.

Richardson and Freitag [24] examined SiC platelet (SiC$_{pl}$) reinforced MoSi$_2$. The

reinforcement in this case was hexagonal α-SiC$_{pl}$, approximately 17 μm in diameter and

2.3 μm thick and at 20 vol%. The MoSi$_2$ powder used was in two forms: 16.0 μm

14
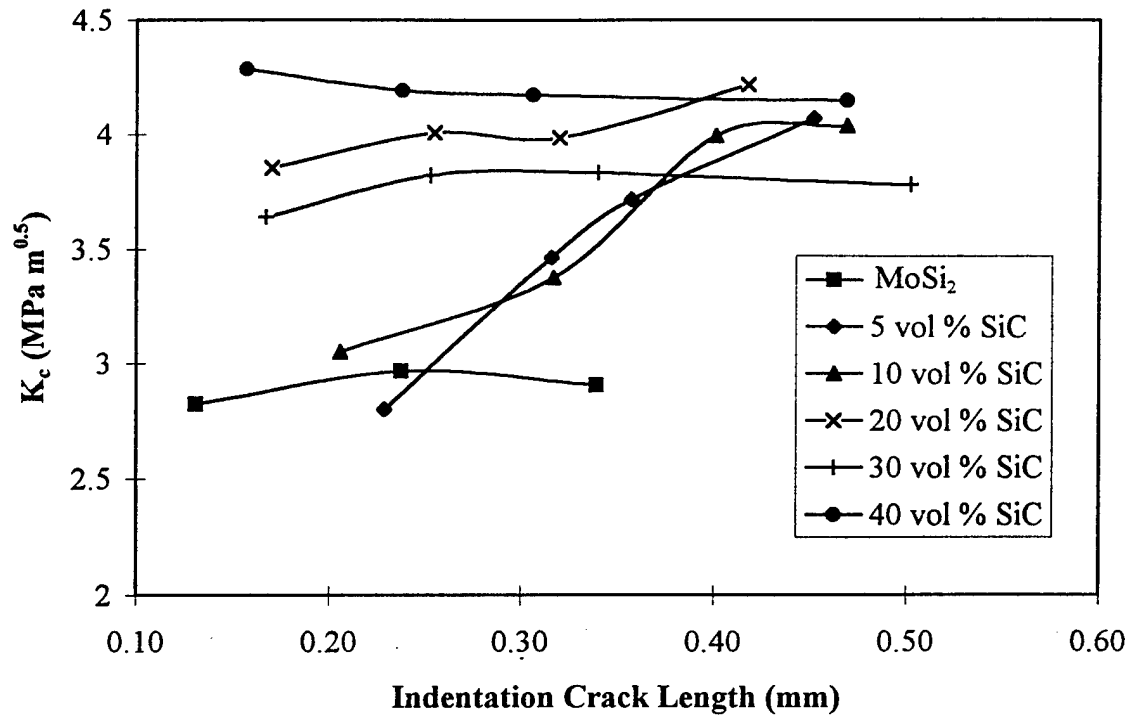
Figure 8: Fracture resistance vs. indentation crack length for SiC_p / $MoSi_2$ composites [7]. Different indentation crack lengths were obtained by varying the indentation load. The fracture toughness increases with increased SiC_p content.

average particle size (99.5% pure) and 8.6 μm average particle size (99.95% pure). The materials were hot pressed in helium at 1700 °C and 34.5 MPa for 90 min.

Flexure bars and chevron notch bars for four-point bend tests were used to determine the flexure strength and fracture toughness, respectively. The reinforced samples showed higher flexural strength than the monolithic sample studied by Carter *et al.* [25] (fig. 9). The composite made with the 16.0 μm particle size $MoSi_2$ exhibited higher flexural strength than the 8.4 μm particle size $MoSi_2$ at temperatures above approximately 900 °C but under 900 °C the behavior was reversed. The 8.4 μm particle size $MoSi_2$ sample also exhibited a lower transition temperature than the 16.0 μm particle size $MoSi_2$ because of the increased porosity found in the 8.4 μm particle size $MoSi_2$.

15

Strength (MPa)

400
350
300
250
200
150
100
50
0

—■— 20 vol% SiC$_{pl}$ / 16.0 μm MoSi$_2$
—♦— 20 vol% SiC$_{pl}$ / 8.4 μm MoSi$_2$
—▲— 99.5% Pure MoSi$_2$ Carter *et al.*

0   -200   400   600   800   1000   1200   1400   1600
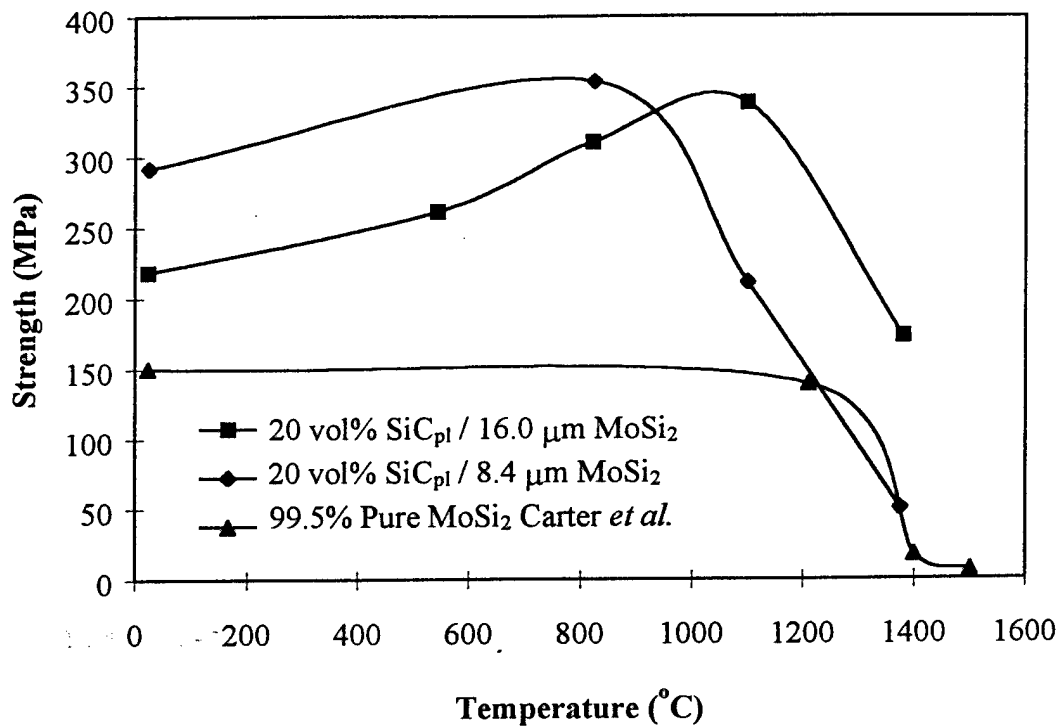
Temperature (°C)

Figure 9: Flexural strength vs. temperature for SiC$_{pl}$ reinforced MoSi$_2$ [24,25]. Notice that the 16 μm MoSi$_2$ composite shows a lower transition temperature than the 8.4 μm MoSi$_2$ composite.

Their results indicated that the fracture toughness increased with temperature until approximately 800 °C and then decreased dramatically until 1100 °C, the highest test temperature (fig. 10). The increase in fracture toughness under 1100 °C stemmed from crack deflection and pullout of the SiC$_{pl}$.

3.6 Effect of Intrinsic Second Phases in MoSi$_2$

Cotton *et al.* [26] studied the effects of the SiO$_2$ that is inherently present on the surface of MoSi$_2$ particles in commercial powders. The powders were hot-pressed into small disks in graphite dies at 1700 °C and 31 MPa for 30 min. The powders used consisted of two types: commercial MoSi$_2$ and arc melted MoSi$_2$ produced in the laboratory [27]. The commercial powder obtained from Cerac, Inc. consisted of 5 μm
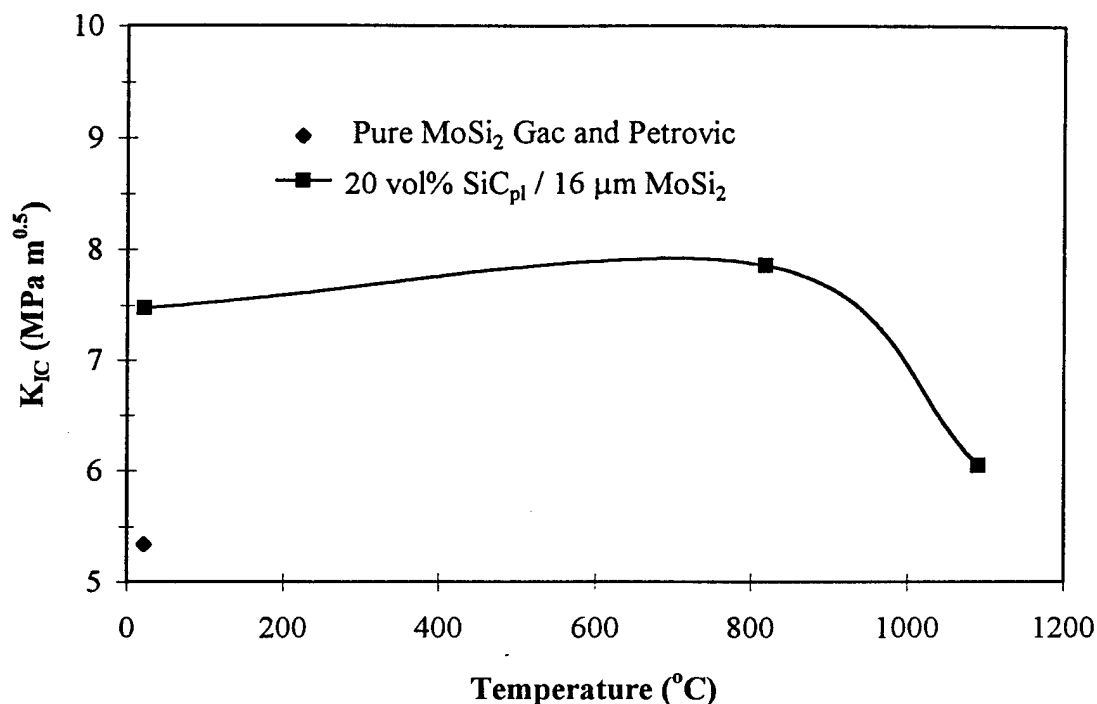
Figure 10: Fracture toughness vs. temperature for SiC$_{pl}$ reinforced MoSi$_2$ [24,28]. Notice that the room fracture toughness of the composite is higher than the monolithic MoSi$_2$.

particles. The laboratory powders were produced by arc-melting the correct proportions of pure Mo and Si, followed by roll grinding in ethanol for 170 h which yielded approximately 10 μm particles. Some of the arc-melted material was not ground to show a comparison between the hot-pressed and arc-melted material.

Energy dispersive spectrometry (EDS) and selected-area diffraction patterns (SADP) in TEM were used to determine the secondary phases present. Amorphous silica (SiO$_2$) was detected in both samples in amounts ranging from 5 to 10 vol%. It was also noted that there were small amounts of SiC and Mo$_{\leq4.8}$Si$_3$C$_{\leq0.6}$ found at the grain boundaries which were thought to be produced by carbon contamination from the graphite die.

The fracture surfaces of bend samples showed that SiO_2, SiC and $Mo_{\leq 4.8}Si_3C_{\leq 0.6}$ were present at the grain boundaries. This indicated that the presence of these phases caused the material to fracture intergranularly [26]. The arc-melted material (not ground) was also fractured and showed transgranular cleavage and the absence of SiO_2, SiC and $Mo_{\leq 4.8}Si_3C_{\leq 0.6}$ on the fracture surface. The transgranular fracture is desirable because the toughness is determined by the properties of the $MoSi_2$ and not the phases present at the grain boundaries (i.e., SiO_2, SiC and $Mo_{\leq 4.8}Si_3C_{\leq 0.6}$). This implies that the elimination of these secondary phases would allow the mechanical properties to be dominated by the $MoSi_2$ and not the secondary phases.

The contact angle between the $MoSi_2$ and SiO_2 particles was approximately 120° which indicated only slight wetting. This was consistent with their observation that the SiO_2 found in grains had a spherical shape. The SiO_2 found at the grain boundary was described as being "two spherical caps which appeared ellipsoidal in projection" [26]. Similar results were reported by Kisly and Kodash [22]. This spheroidization of SiO_2 leads to a decrease in oxidation resistance above 1700 °C for $MoSi_2$.

4. Materials and Experimental Procedure

4.1 Materials

The as-received $MoSi_2$ powder[i] consisted of the four types shown in Table 5. Grade A and Grade C were pure $MoSi_2$ with particle size of approximately 10 μm and 3 μm, respectively. Carbon coating was put on the Grade C $MoSi_2$ particles by two different processes. The actual carbon content in the powders after pyrolysis was measured at ART [29] by using a Leco carbon analyzer.

4.2 Powder Processing

The two processes used to coat Grade C $MoSi_2$ particles were: Phenolic Resin Based Carbon by Solvent Evaporation (PRBCSE) and Aqueous Dispersion Flocculation (ADF). The coating was done at ART.

The PRBCSE powder used a phenol formaldehyde resin, Polyophen 23056[ii], to apply a carbon coating on the $MoSi_2$ particles. The resin, Grade C $MoSi_2$ powder, and acetone were mixed by ball-milling. The acetone was then evaporated leaving only the resin coating on the $MoSi_2$ particles (see fig. 11). The resin coating was then pyrolyzed at 600 °C for 1 h in argon to yield a carbon coating on $MoSi_2$ particles. The coated powder was then pressed into a green compact in a steel die and sintered. Due to the nonuniformity of SiC_p found in some preliminary samples, these powders were ball-milled

---

i Advanced Refractory Technologies, Inc., Buffalo, NY
ii Durez Corp., North Tonawanda, NY

Table 5: Composition of the different powder blends by weight percent. Grade A and Grade C are pure $MoSi_2$ with powder particle sizes of approximately 10 μm and 3 μm, respectively. [29]

	Grade A (wt%)	Grade C (wt%)	Actual Carbon (wt%)
ARSE 70/30	70	30	0
ARSE 0/100	0	100	0
PRBCSE	0	98.79	1.21
ADF	0	97.12	2.88
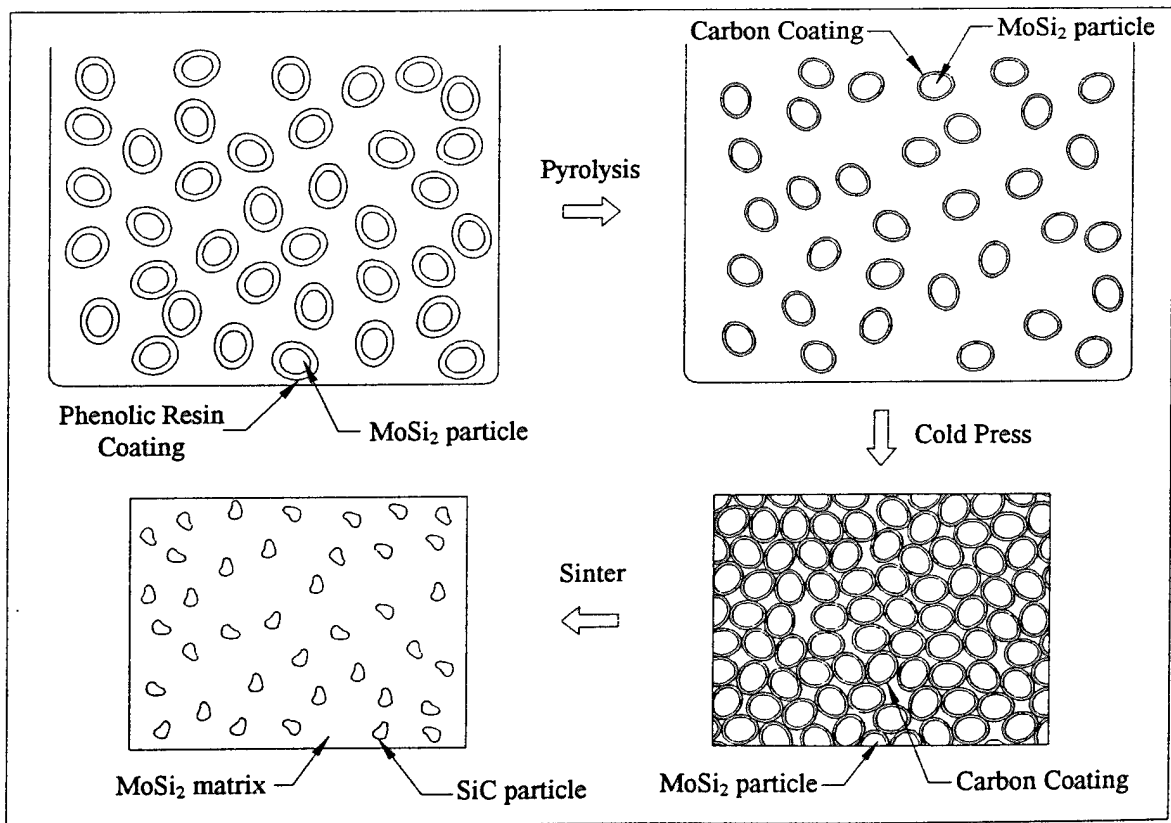
Figure 11: Schematic of the PRBCSE process.

using WC media to obtain a more uniform distribution of carbon in the $MoSi_2$ powders and SiC_p in the consolidated samples.

In the ADF process, a high carbon yielding cationic starch flocculant was electrostatically adhered to the surface of the $MoSi_2$ particles giving a move even distribution of resin compared to that obtained in the PRBCSE process. The starch used was Redibond 5320[iii] which is a liquid natural polymer with cationic quaternary amine functionality. The process involved dispersing the $MoSi_2$ powder in an aqueous system by adding an anionic dispersant and ball-milling for 1 h. The starch flocculant and glycerol plasticizer were added to the slurry and ball-milled for another 30 min. The slurry was put in a high shear blender and the pH was increased to activate the flocculant which gelled the slurry. At this point the $MoSi_2$ powder was uniformly coated with the starch. Water was added to thin the slurry and put into a vacuum forming die to remove the water. The material was dried and passed through a 100 mesh screen. The powder was pressed into a green sample and pyrolyzed at 600 °C for 1 h in vacuum to convert the starch into carbon (see fig. 12). The sample was then sintered.

4.3 Experimental Procedure

The powders were cold pressed under a pressure of 140 MPa into thin, disk shaped, green samples. These disks were approximately 2.9 cm in diameter (inside diameter of the die), approximately 0.4 cm in height, and weighed approximately 8 g. The mass, diameter, and height were measured to calculate an approximate geometric, green

---

iii National Starch and Chemical Company, Bridgewater, NJ
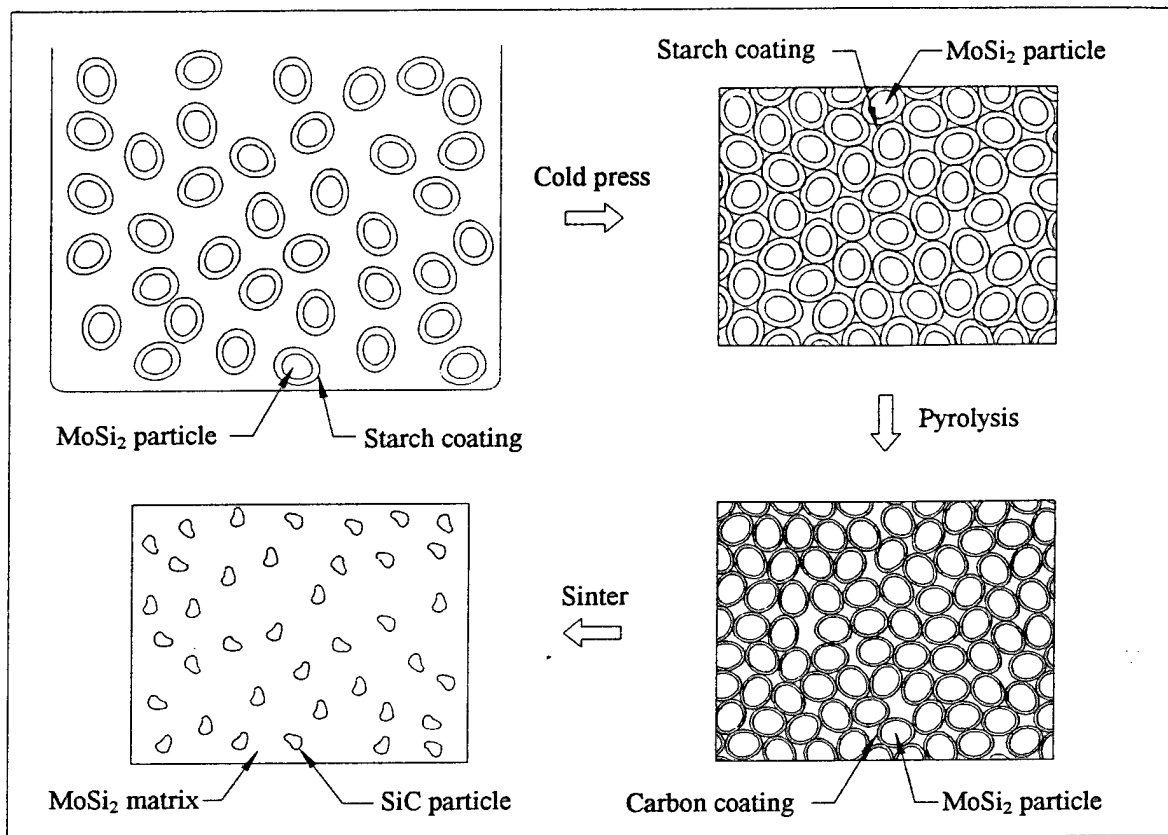
Figure 12:   Schematic of the ADF process.

density. Before sintering, the samples were embedded in a mixture of 50 wt% MoSi$_2$ / 50

wt% BN or placed on top of SiC disks. The purpose of embedding the material was to

isolate the samples from the graphite crucible, minimize volatilization of the carbon, obtain

uniform shrinkage, improve microstructural uniformity, and enhance densification [29].

BN powder was used to prevent the MoSi$_2$ bed from densifying during sintering. The SiC

disks were used to isolate the samples from the graphite crucible and to eliminate the

formation of MoB which resulted in samples which were embedded in the MoSi$_2$/BN

powder. Multiple sets of samples were sintered under nine different conditions shown in

Table 6. Samples were heated at 10 °C/min and held at 600 °C for 1 h to pyrolyze the

starch in the ADF samples; a typical sintering schedule is shown in fig. 13. The starch was

Table 6:   Work matrix for the twelve different sintering conditions.

	1 h	10 h	100 h
1600 °C	X	X	X
1700 °C	X	X	X
1800 °C	X	X	X

not pyrolyzed on the $MoSi_2$ particles before cold pressing so that it could be used as a binder in the cold pressed samples to toughen the compacts for handling.

An Astro high temperature furnace (1000-3560-FP20) that could reach temperatures in excess of 2000 °C in inert atmospheres was used. A computer controller was designed to control the temperature (fig. 14). This computer controller varied the furnace power output to match the input temperature from the axially mounted, Type C thermocouple (W-5% Re / W-26% Re) to the set point temperature. The controller could control the temperature to within ±0.1 °C of the set point during ramping and soaking and less than 5 °C overshoot going from ramp to soak and vice versa. A new furnace cooling system that used a liquid to liquid heat exchanger was also designed.

The sintered densities were determined by a nondestructive glycerol submersion method [30]. This method involves weighing a sintered sample, in air, followed by weighing the sintered sample submerged in a mixture of glycerol and distilled water (86 wt% glycerol / 14 wt% distilled water), and finally weighing the sintered sample impregnated with the glycerol mixture in air. The density was then calculated from the following expression,
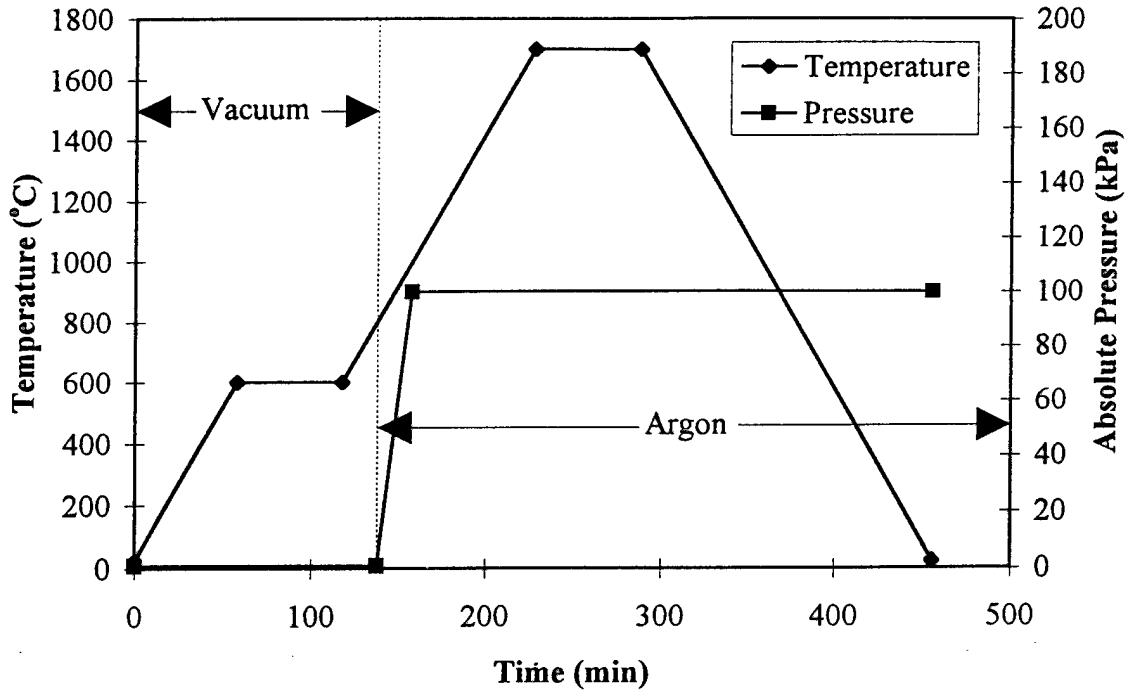
Figure 13:   Typical sintering schedule for sintering at 1700 °C for 1 h.

$$\rho_S = \rho_g \cdot \frac{M_1}{M_3 - M_2}$$

where ρ_S is the density of the sample, ρ_g is the density of the glycerol mixture, M_1 is the mass of the sample in air before submersion, M_2 is the mass of the sample while submerged in the glycerol mixture, and M_3 is the mass of the sample with the glycerol mixture impregnated, weighed in air. According to Pennings and Grellner [30], the reproducibility of density measurement by this technique is better than 0.003 g/cm^3, while the accuracy is better than 0.006 g/cm^3.

The grain size was determined using optical micrographs taken in polarized light. ASTM Standard E 112-85 comparison method [31] was used for the grain size determination.

The sintered samples were polished to a 600 grit finish using SiC grinding paper to obtain a flat surface and to remove the surface layer for X-ray diffraction (XRD). After

24
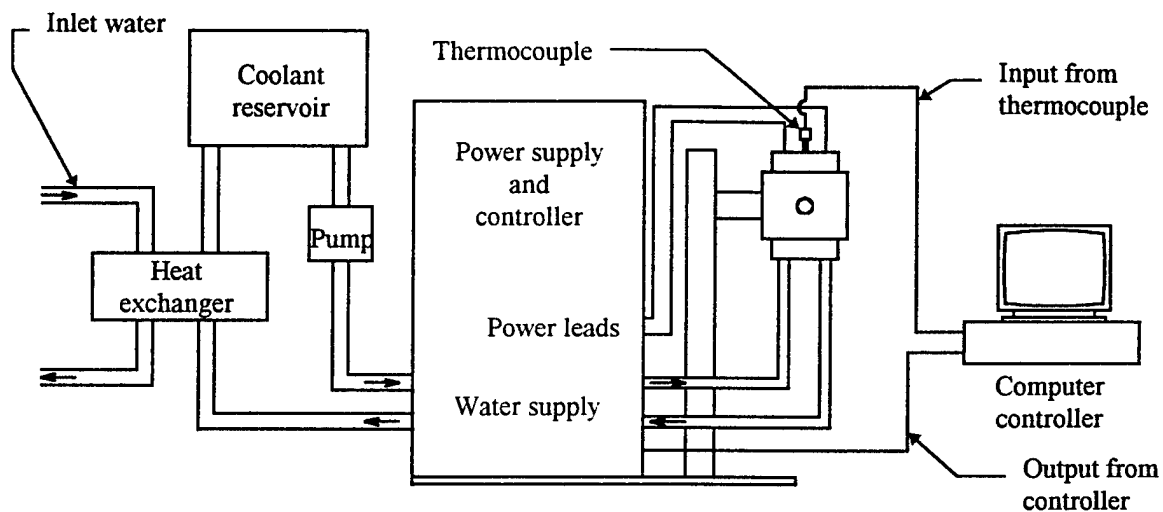
a.
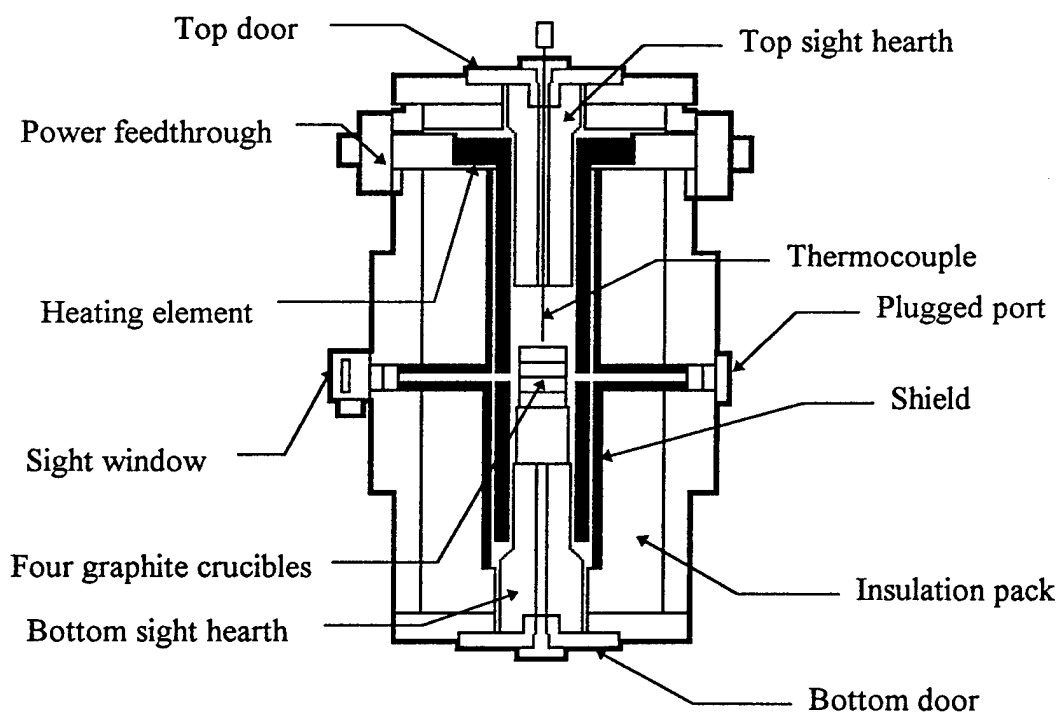
b.

Figure 14: Schematic diagrams of (a) Furnace assembly and accessories, and (b) Furnace.

Table 7: Work matrix for the analyses that will be done on all the samples with the purpose of each.

	Phase Distribution	Average Grain Size	Fracture Toughness	Hardness	Determination of Phases
OM					
Bright field	X				
Polarized		X			
Microprobe	X				X
SEM	X				
EDS					X
WDS	X				X
XRD					X
Vickers Indentation			X	X	

XRD, the samples were mounted in epoxy and polished to a 0.1 μm finish using diamond paste. Optical microscopy (OM) and scanning electron microscopy (SEM) were used to characterize the microstructure. The work matrix in Table 7 shows the analyses done, along with the purpose for each of the analyses.

A Zeiss and a Unitron Versamet-2 optical microscopes were both used to study the porosity in bright field and grain structure in polarized light. A Hitachi Hi-scan HHS-2R and JEOL high resolution SEM were used for the SEM examination. A JEOL 733 microprobe with both energy and wavelength dispersive spectrometry, EDS and WDS, attachments with low element detection capabilities was used for phase identification and distribution analysis. A Leco M-400 microhardness tester and a Leco macrohardness tester were used for Vickers indentation tests. Siemens D5000 and Philips PW-1720 X-ray diffractometers were used for X-ray diffraction analysis. A Cu target ($\lambda_{K\alpha} = 0.154$ nm) was used at an acceleration voltage of 40 kV and a current of 20 mA.

5. Results

5.1 Material Characterization

5.1.1 Density Measurements

The average green density values are shown in Table 8. The ARSE 70/30 green density was higher than the ARSE 0/100 green density which is attributed to the bimodal powder distribution of the ARSE 70/30 which resulted in higher overall sintered densities. The green density of the ARSE 0/100 was lower than that of the PRBCSE and ADF because of the lubricating effect of the carbon in the PRBCSE and starch in the ADF. The ADF powder could be handled much easier than the other samples indicating that the starch also served as a binder. The ADF samples could have been pressed at a higher pressure but for the sake of consistency the same pressure (138MPa) was used. A higher pressure on these samples could have resulted in higher green and sintered densities and possibly less porosity. The final sintered ADF samples never showed cracking whereas the others always showed cracking in the green state.

The sintered densities for all of the powders are shown in figs. 15 through 18. The densities were measured using samples that were surface ground to remove the MoB that formed on the surface of all the samples sintered in the $MoSi_2$/BN embedding powder (50 wt% $MoSi_2$ / 50 wt% BN). The MoB surface coating did penetrate into the sintering

Table 8:   Green density for all of the samples.

	ARSE 70/30	ARSE 0/100	PRBCSE	ADF
Density (g/cm³)	3.46	3.05	3.30	3.70
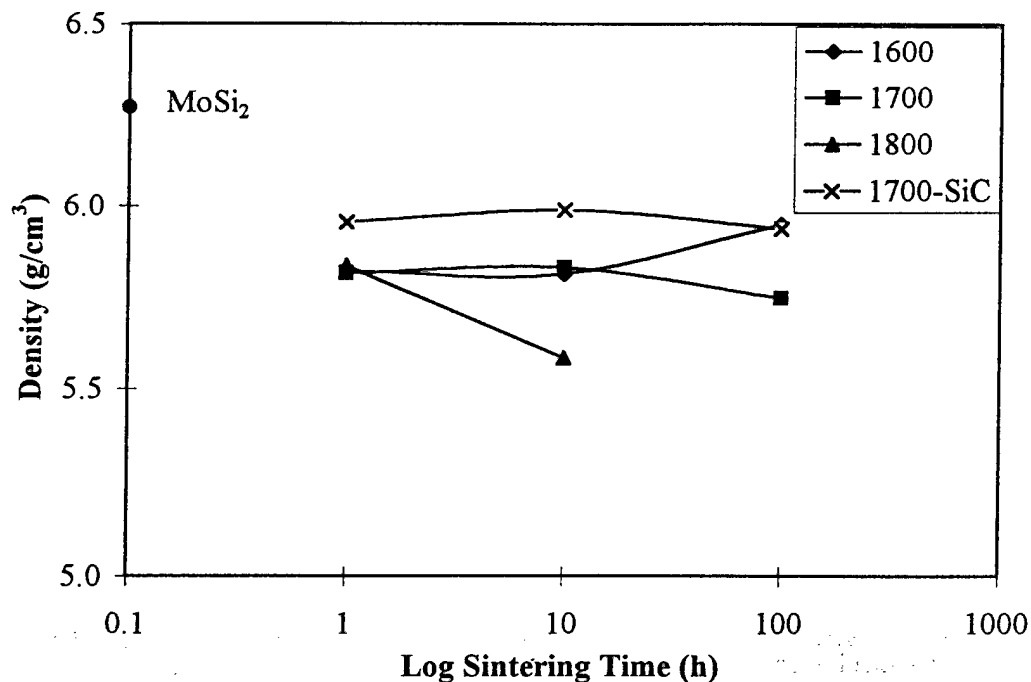
Figure 15: Density vs. sintering time for ARSE 70/30 sintered at various temperatures. Circle shows the theoretical density for $MoSi_2$. 1700-SiC represents samples sintered on SiC disks, all others were embedded in 50 wt% $MoSi_2$ / 50 wt% BN.
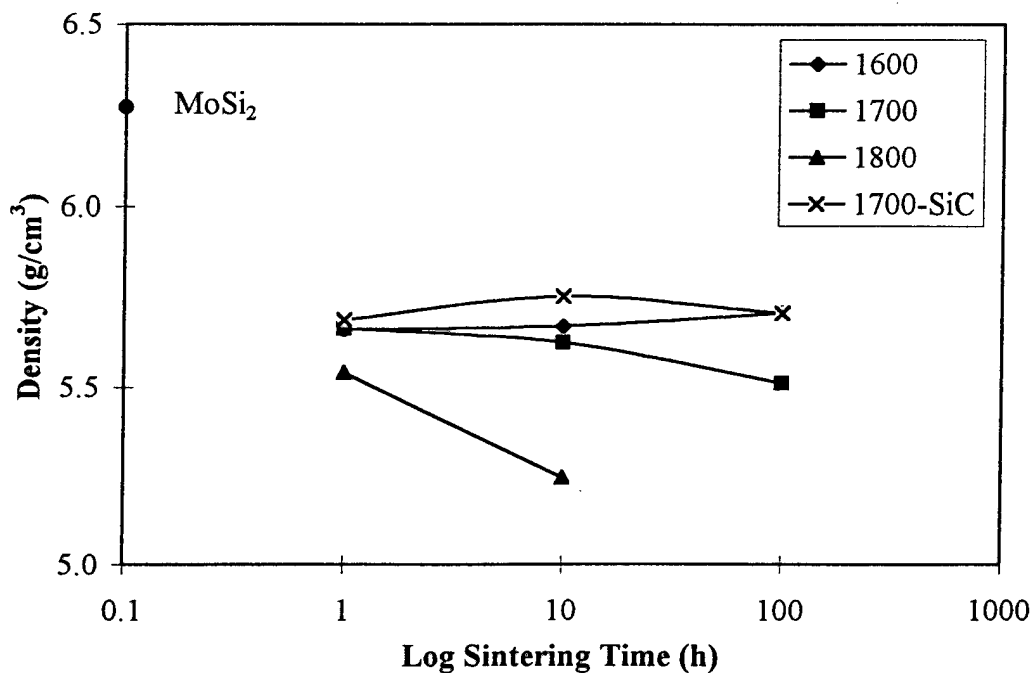
Figure 16: Density vs. sintering time for ARSE 0/100 sintered at various temperatures. Circle shows the theoretical density for $MoSi_2$. 1700-SiC represents samples sintered on SiC disks, all others were embedded in 50 wt% $MoSi_2$ / 50 wt% BN.

28
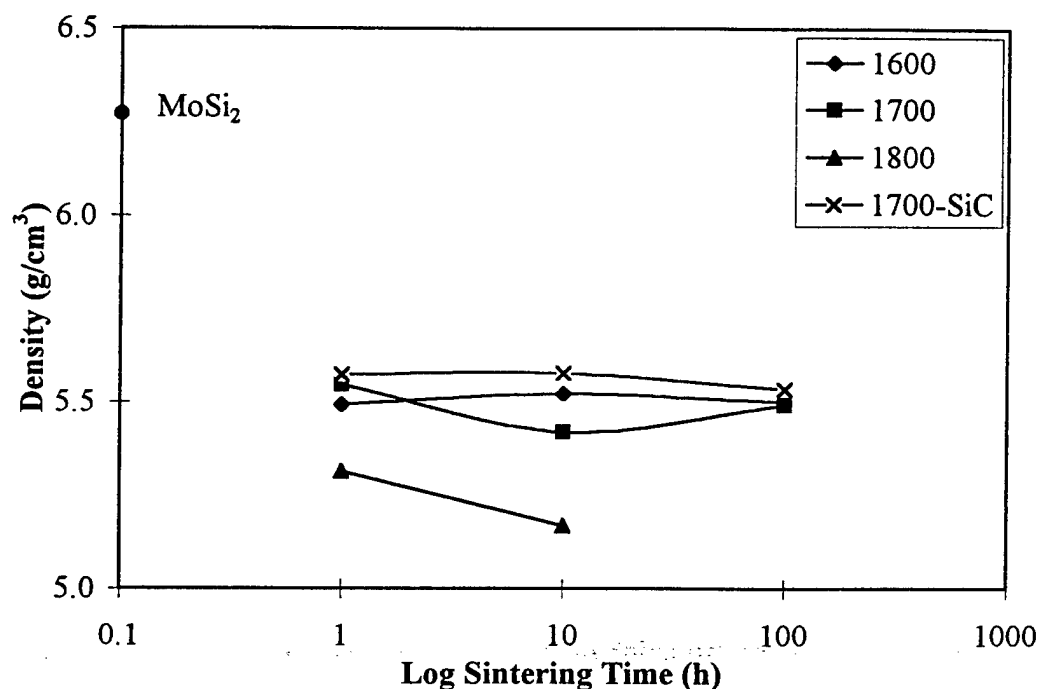
Figure 17: Density vs. sintering time for PRBCSE powder sintered at various temperatures. Circle shows the theoretical density for $MoSi_2$. 1700-SiC represents samples sintered on SiC disks, all others were embedded in 50 wt% $MoSi_2$ / 50 wt% BN.
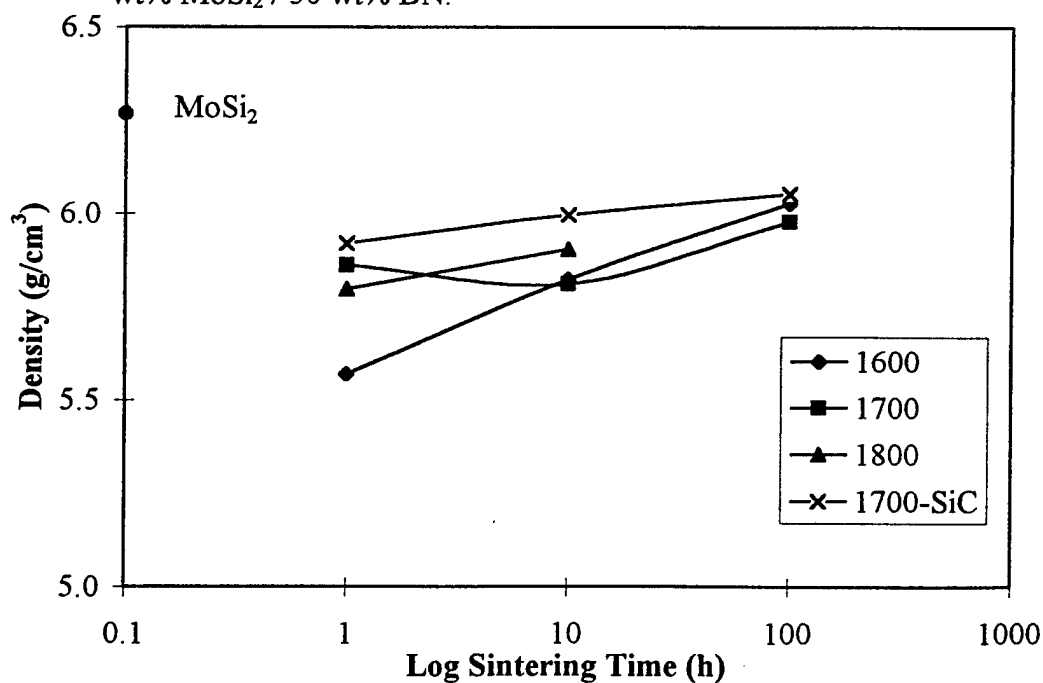
Figure 18: Density vs. sintering time for ADF powder sintered at various temperatures. Circle shows the theoretical density for $MoSi_2$. 1700-SiC represents samples sintered on SiC disks, all others were embedded in 50 wt% $MoSi_2$ / 50 wt% BN.

induced cracks leaving very small amounts of MoB in all but the ADF samples. The density of MoB (ρ_{MoB} = 8.6 g/cm^3) is higher than that of MoSi$_2$ (ρ_{MoSi2} = 6.25 g/cm^3) which would result in higher overall density values if it were not removed.

The densities of the samples sintered on SiC disks were generally higher than those sintered in the MoSi$_2$/BN embedding powder, see figs. 15 through 18. The density of all of the samples sintered at 1800 °C was lower than that of those sintered at lower temperatures which could be attributed to the higher porosity found in the samples sintered at 1800 °C. The density of the samples sintered on the SiC disks was higher than that of the samples sintered in the MoSi$_2$/BN powder indicating that the embedding powder affected the densification of the samples. The embedding powder could also be the cause for the melting of the samples sintered at 1800 °C for 100 h and the dramatic decreases in density for the samples sintered at 1800 °C for 1 and 10 h compared with those sintered at lower temperatures.

5.1.2 Grain Size

The grain size results are shown in figs. 19 through 22. The average grain size of the ADF samples was very nonuniform compared with the other samples (fig. 23). The most notable trend common to all the samples was the large average grain size found in the samples sintered at 1800 °C. The samples sintered at 1800 °C for 100 h melted and could not be studied. The melting could be due to a eutectic reaction between MoSi$_2$ and BN in the embedding powder. All the samples exhibited an increase in average grain size with increasing time and temperature as expected. The ARSE 70/30, ARSE 0/100 and PRBCSE samples sintered on the SiC disks at 1700 °C exhibited a relatively constant
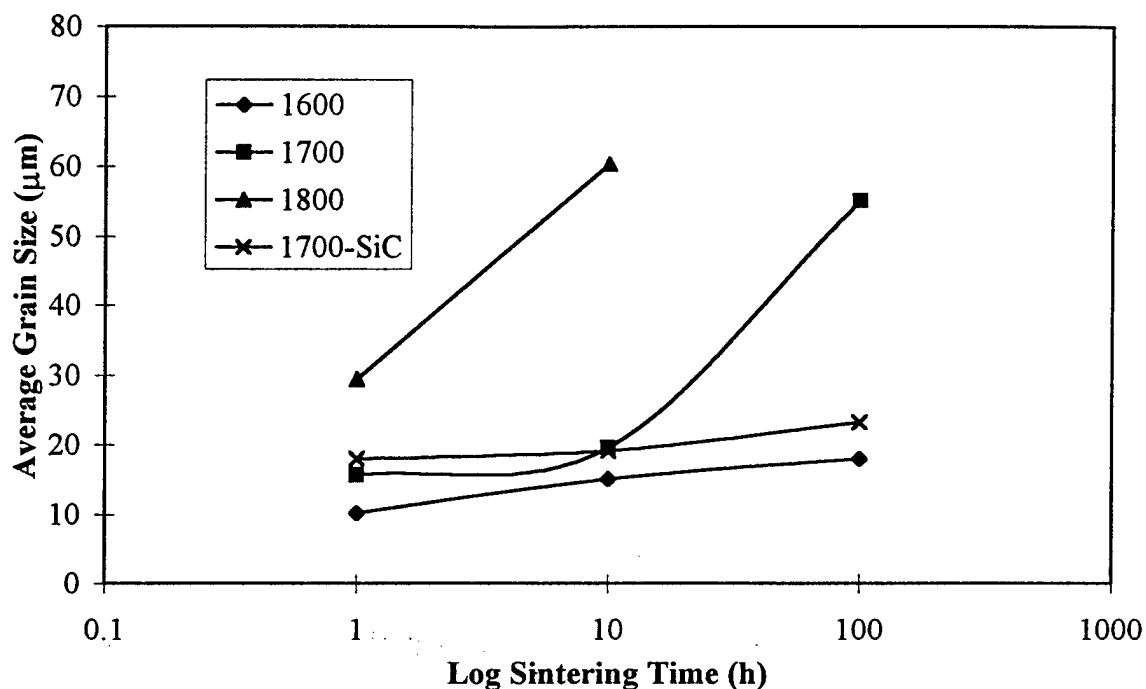
Figure 19:   Grain size vs. sintering time for the ARSE 70/30 samples sintered at various
temperatures. 1700-SiC represents samples sintered at 1700 °C on SiC
disks, all others were embedded in 50 wt% MoSi$_2$ / 50 wt% BN.

Figure 20:   Grain size vs. sintering time for the ARSE 0/100 samples sintered at various
temperatures. 1700-SiC represents samples sintered at 1700 °C on SiC
disks, all others were embedded in 50 wt% MoSi$_2$ / 50 wt% BN.

31
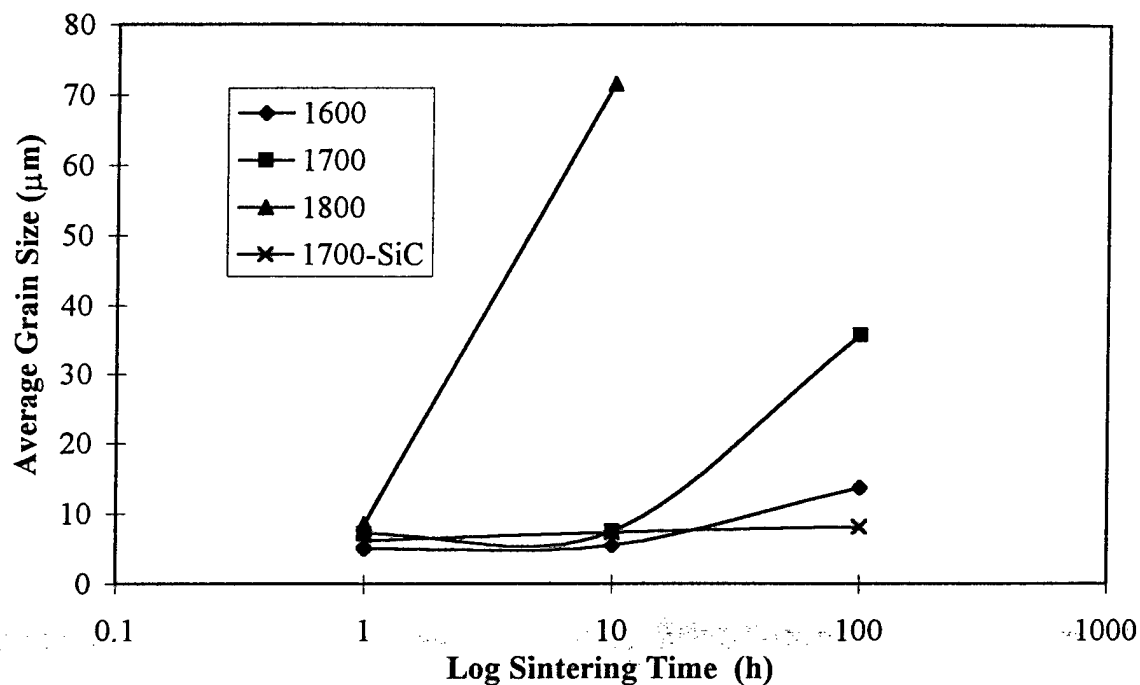
Figure 21: Grain size vs. sintering time for the PRBCSE samples sintered at various temperatures. 1700-SiC represents samples sintered at 1700 °C on SiC disks, all others were embedded in 50 wt% MoSi$_2$ / 50 wt% BN.
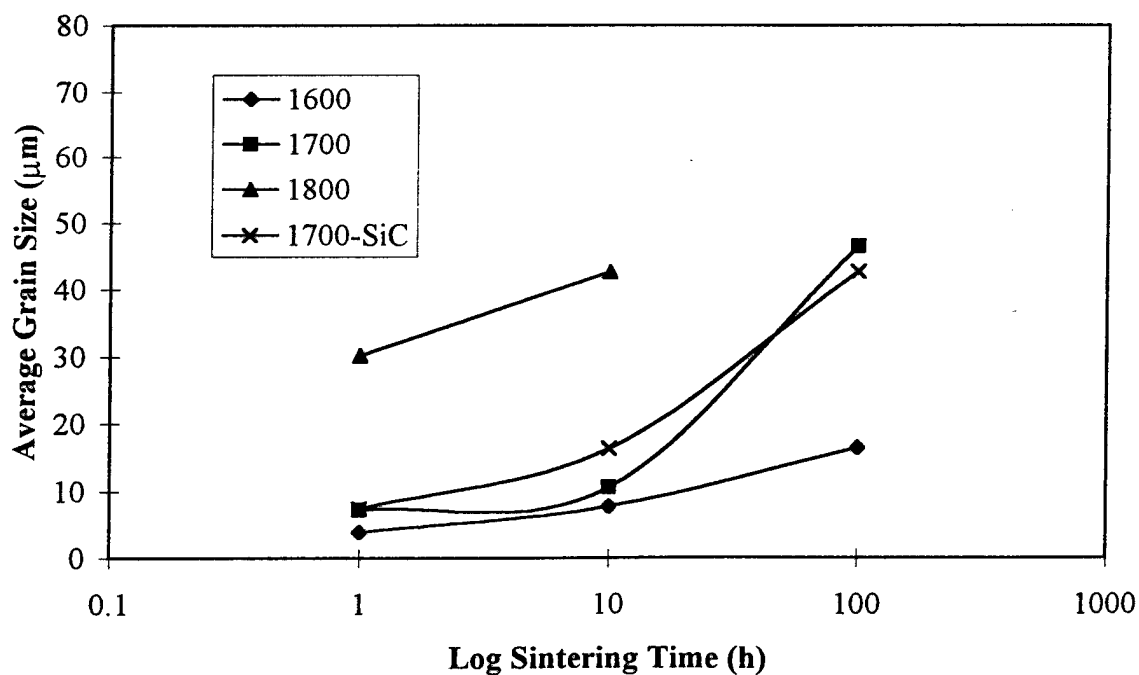
Figure 22: Grain size vs. sintering time for the ADF samples sintered at various temperatures. 1700-SiC represents samples sintered at 1700 °C on SiC disks, all others were embedded in 50 wt% MoSi$_2$ / 50 wt% BN.
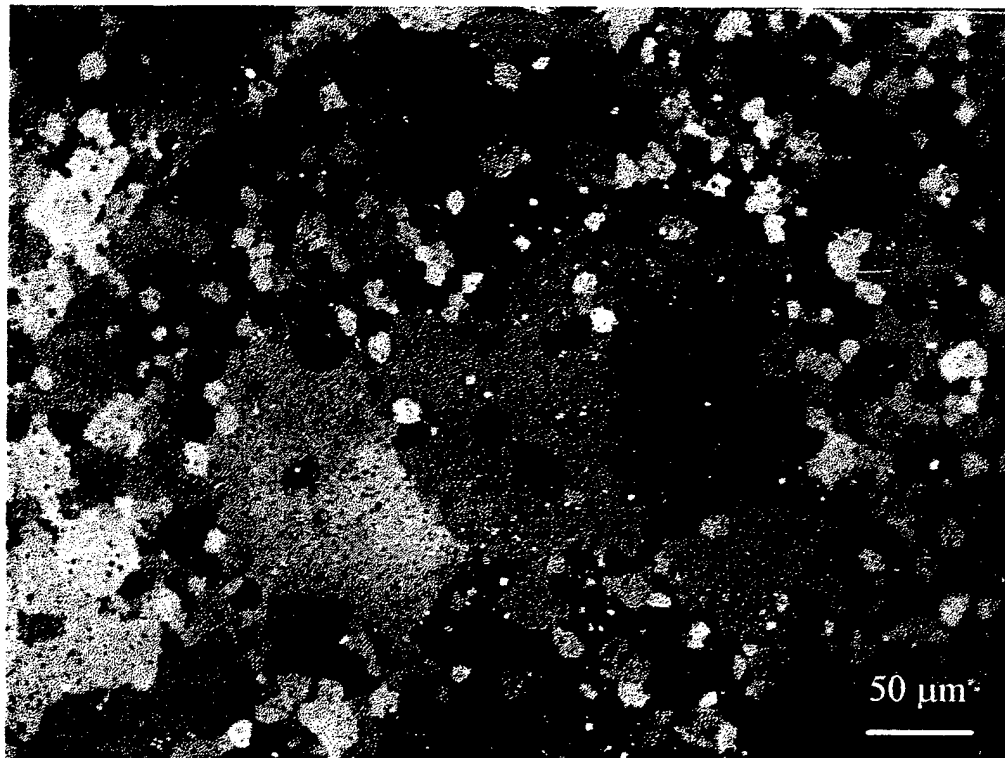
Figure 23:   Optical micrograph in polarized light of an ADF sample sintered at 1800 °C for 1h. Notice the highly nonuniform grain size.

average grain size with increasing time (figs. 19 through 21). This may be a result of grain

boundary pinning by the SiO_2 particles at the grain boundaries inhibiting grain growth.

The ADF sample contained almost no SiO_2 and exhibited a quite large increase in grain

size with increasing sintering time indicating that indeed the SiO_2 may have inhibited grain

growth (fig. 22). The spheroidization temperature for the SiO_2 is approximately 1700 °C

[22]. The average grain size was relatively constant at 1600 °C (i.e., below the

spheroidization temperature) in the ARSE 70/30, ARSE 0/100 and PRBCSE samples.

But at 1700 and 1800 °C the average grain size increased more rapidly indicating that the

spheroidizing of SiO_2 allowed the grains to grow more freely. The ARSE 70/30 contained

a combination of 10 μm and 3 μm particle size $MoSi_2$ and the ARSE 0/100 contained only

3 μm particle size $MoSi_2$, thus the SiO_2 content was higher in the ARSE 0/100 because of

the greater overall surface area. The spheroidization of the SiO_2 in the ARSE 70/30 was

less prominent than the ARSE 0/100 because there was less SiO_2 present allowing grain

growth to occur more freely in the ARSE 70/30 samples. Figure 19 shows a large

increase in average grain size at 1700 °C and 1800 °C with increasing sintering time

indicating the spheroidizing of SiO_2. Figure 20 does not show such a dramatic increase at

1700 °C indicating that the SiO_2 in this sample was controlling the grain growth.

5.1.3 SiO₂ and Porosity

Oxygen maps obtained by energy dispersive X-ray analysis were used to determine

if the carbon addition reduced the presence of SiO_2 (figs. 24 and 25). Figure 24b and 25b

show the EDS oxygen maps for the ARSE 0/100 (3 μm particle size $MoSi_2$) and the ADF

(3 μm particle size $MoSi_2$ with 2.88 wt% carbon) sintered on SiC disks at 1700 °C for 100
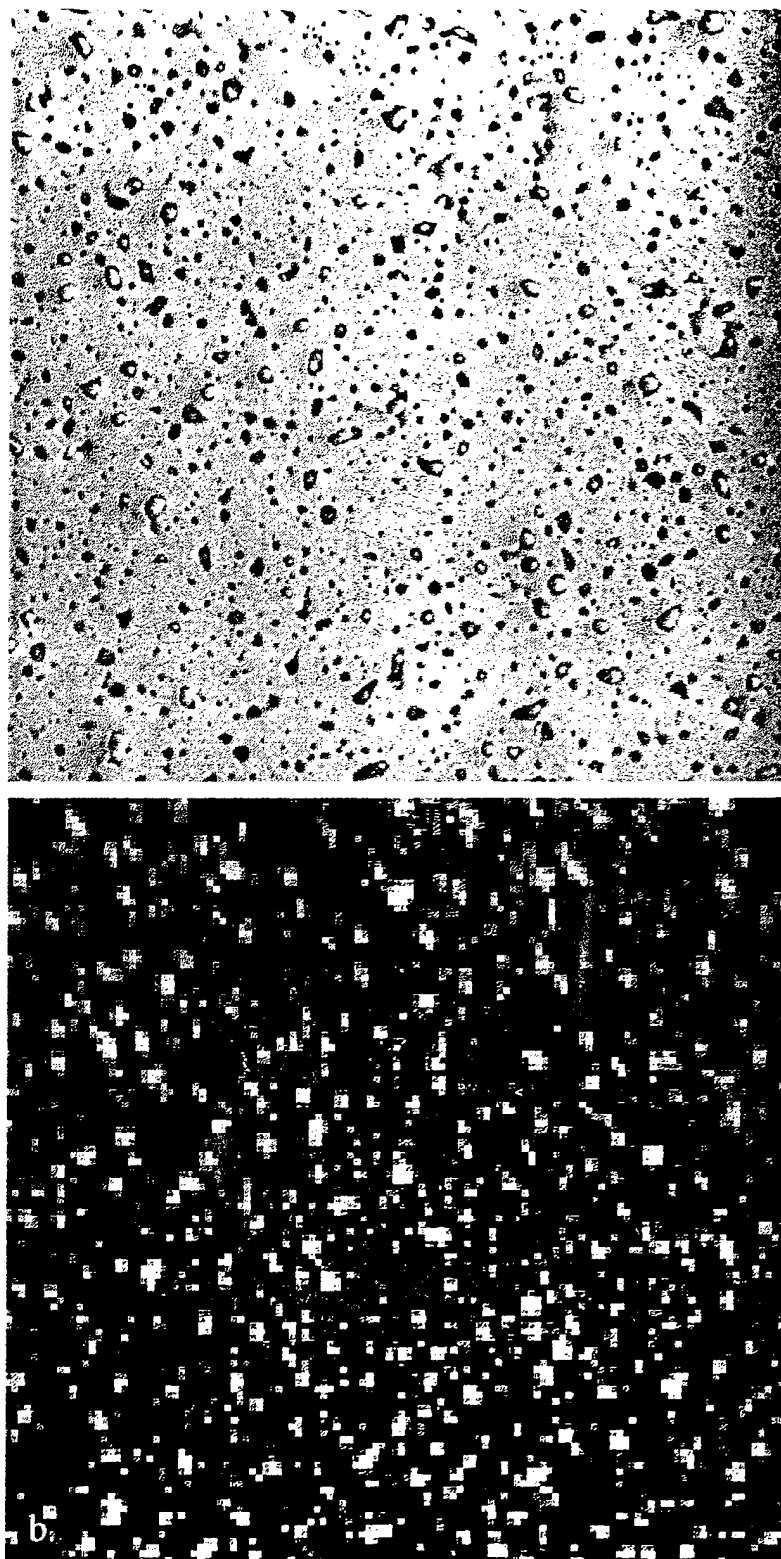
Figure 24: ARSE 0/100 sample sintered at 1700 °C for 100 h on SiC disks **(a) SEM** micrograph and (b) EDS oxygen map of that area shown in (a). **Note the** high oxygen content.
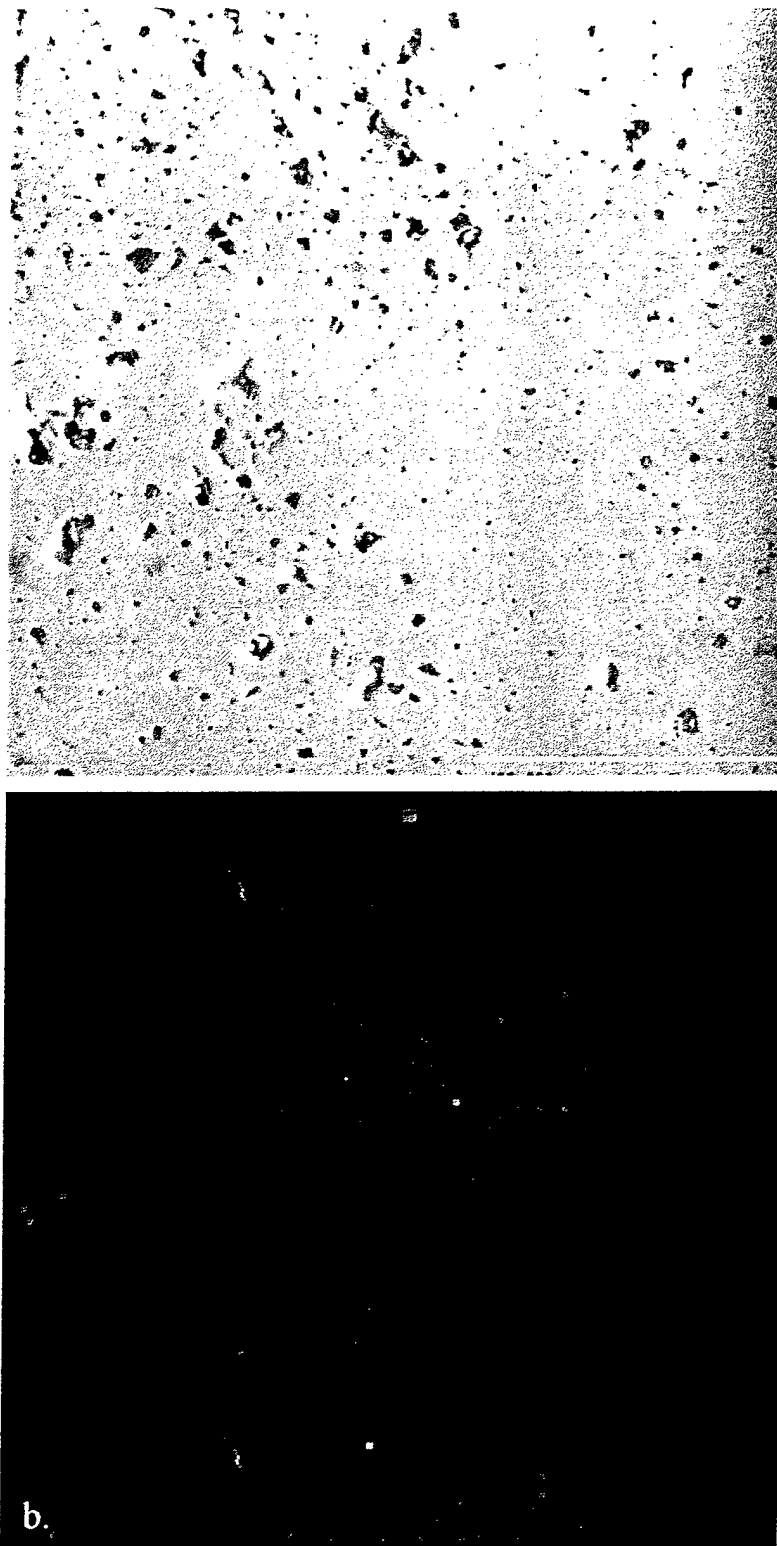
Figure 25: ADF sample sintered at 1700 °C for 100 h on SiC disks (a) **SEM micrograph** and (b) EDS oxygen map of that area shown in (a). Note the **low oxygen** content.

h. The oxygen maps indicate that indeed the SiO_2 content was reduced by the addition of carbon.

Optical micrographs and image analysis software were used to obtain a volume percentage of porosity plus SiO_2 content (figs. 26 through 29). EDS maps of oxygen were then used to obtain a volume percentage of SiO_2, assuming it was the only oxide compound present in the material (fig. 30). This number was then subtracted from the volume percentage of porosity plus SiO_2 obtained using the optical micrographs giving the volume percentage of porosity (fig. 31). This analysis was only done for the samples sintered on top of the SiC disks because these were the only samples used for EDS oxygen mapping. Figure 30 shows that the addition of carbon did reduce the presence of SiO_2 by comparing the ARSE 0/100 samples with the ADF samples. The PRBCSE samples showed much higher SiO_2 which was a result of the ball-milling and this will be explained in Section 5.1.4. The ADF samples showed higher porosity compared to that of the ARSE 0/100 samples caused by the porosity in the ADF samples left after the pyrolysis of the starch before sintering. The porosity in the PRBCSE samples exhibited a similar trend as the ARSE 0/100 but was lower indicating that the high SiO_2 content reduced the porosity found in the sintered samples.

5.1.4 Effects of Ball-milling

Ball-milling was done on the PRBCSE powder to obtain a more even distribution of carbon in the starting powder because the as-received PRBCSE samples all formed SiC_p at pores as shown in fig. 32. The powders were designed so that after pyrolyzing the phenolic resin, the $MoSi_2$ particles would be evenly coated with carbon. Because the
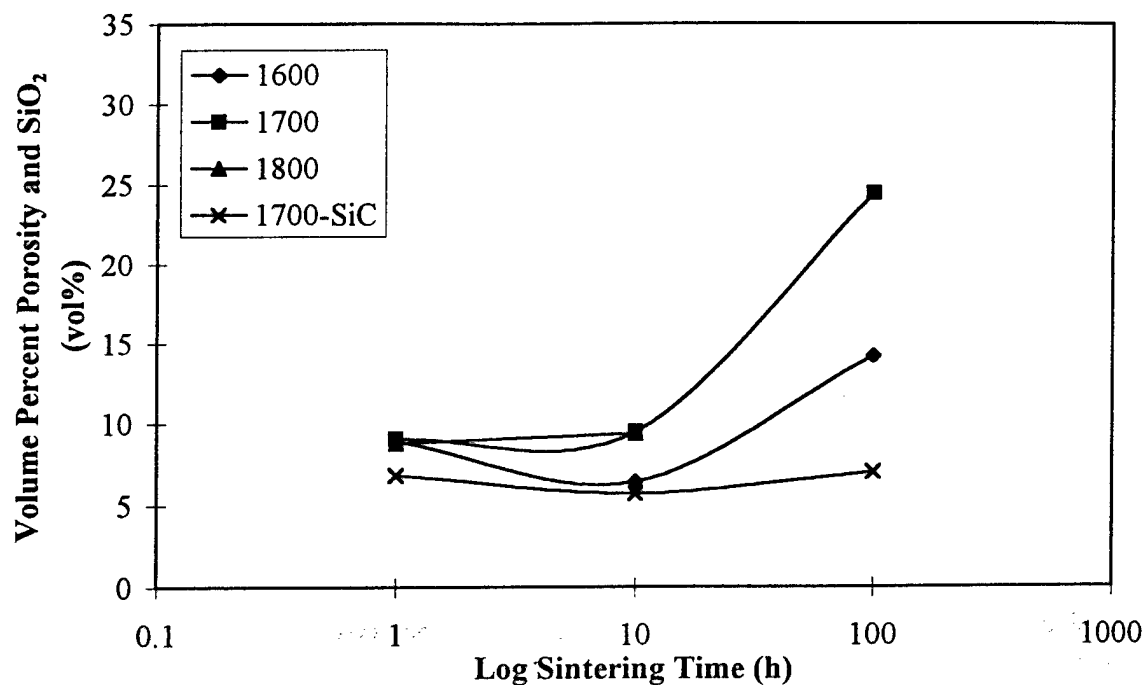
Figure 26: Volume percent porosity and SiO_2 vs. sintering time for the ARSE 70/30 sampies sintered at various temperatures. Obtained using optical micrographs. 1700-SiC represents samples sintered at 1700 °C on SiC disks, all others were embedded in 50 wt% $MoSi_2$ / 50 wt% BN.
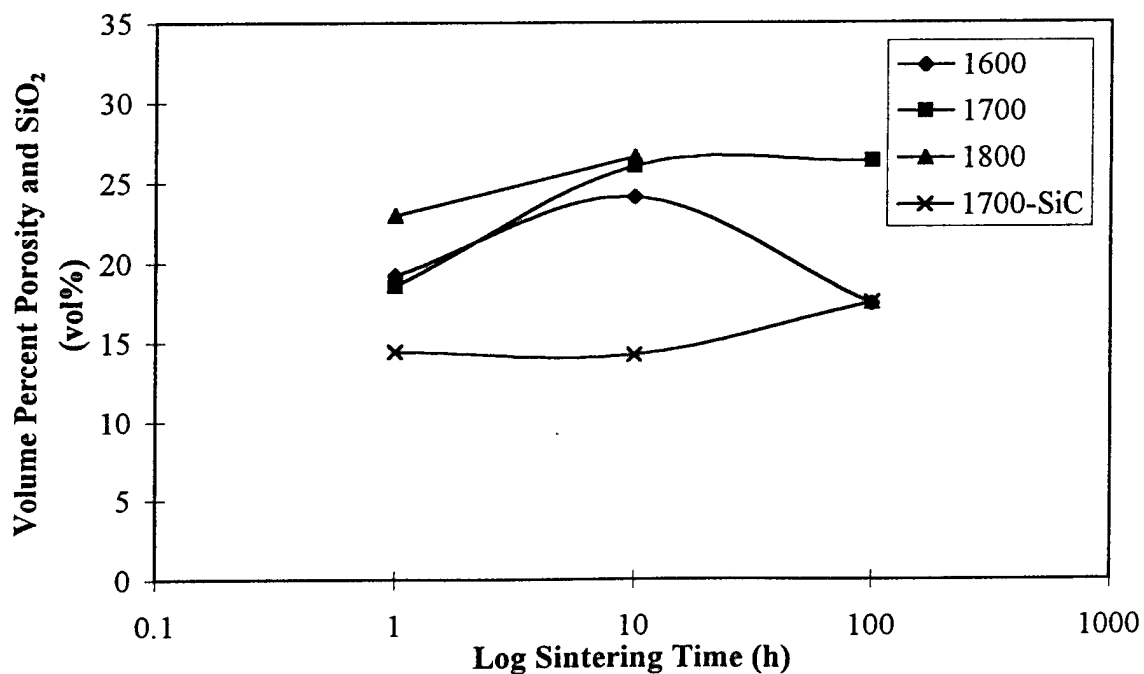
Figure 27: Volume percent porosity and SiO_2 vs. sintering time for the ARSE 0/100 samples sintered at various temperatures. Obtained using optical micrographs. 1700-SiC represents samples sintered at 1700 °C on SiC disks, all others were embedded in 50 wt% $MoSi_2$ / 50 wt% BN.
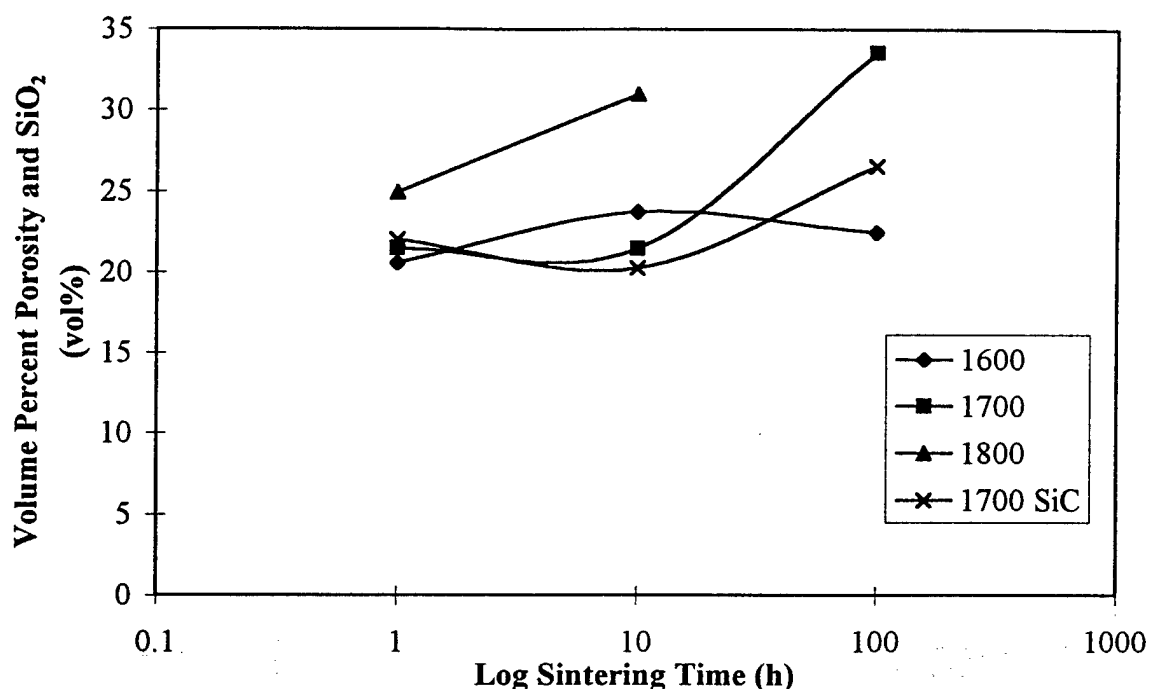
Figure 28: Volume percent porosity and SiO₂ vs. sintering time for the PRBCSE
samples sintered at various temperatures. Obtained using optical
micrographs. 1700-SiC represents samples sintered at 1700 °C on SiC disks,
all others were embedded in 50 wt% MoSi₂ / 50 wt% BN.
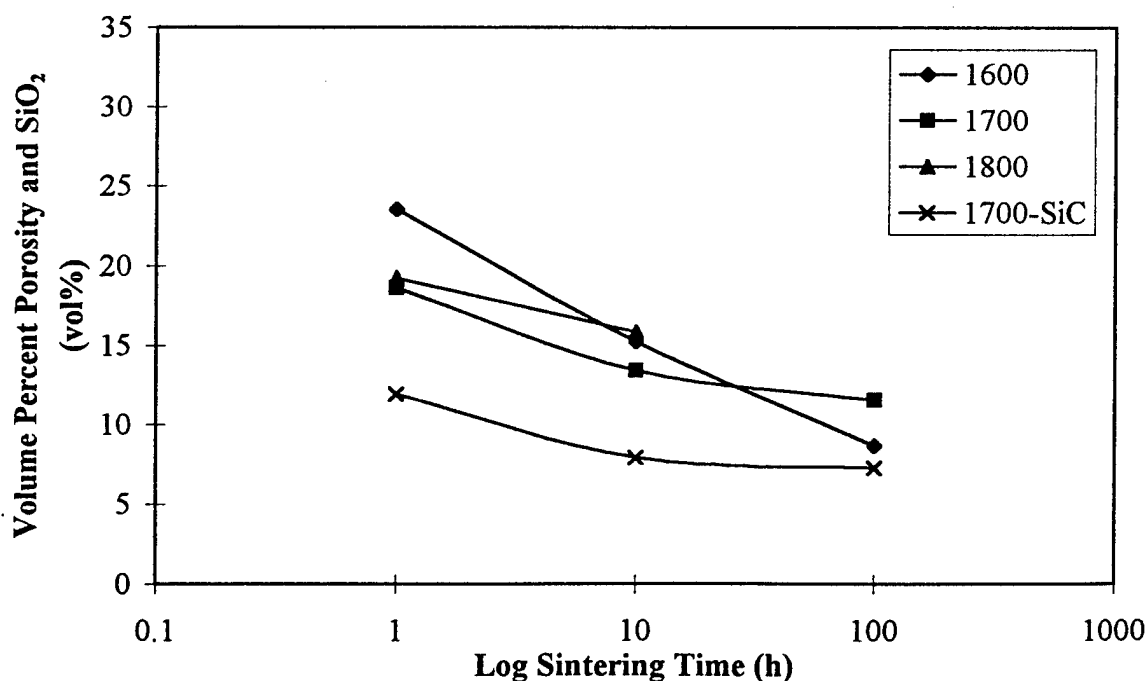
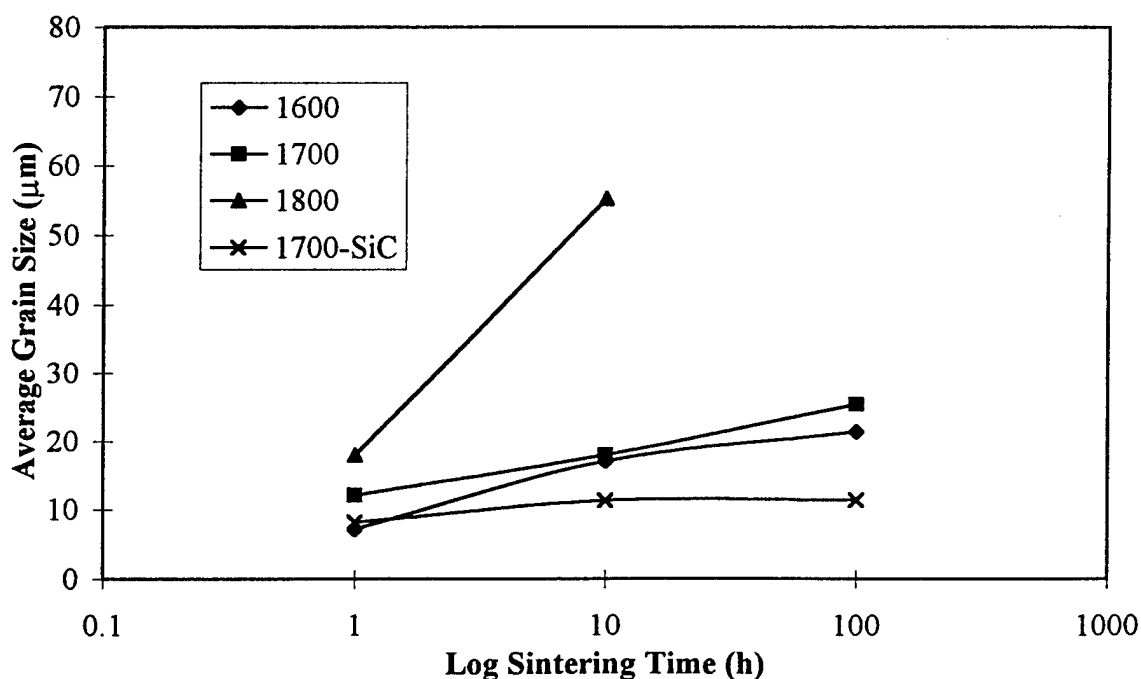Figure 29: Volume percent porosity and SiO₂ vs. sintering time for the ADF samples
sintered at various temperatures. Obtained using optical micrographs. 1700-
SiC represents samples sintered at 1700 °C on SiC disks, all others were
embedded in 50 wt% MoSi₂ / 50 wt% BN.
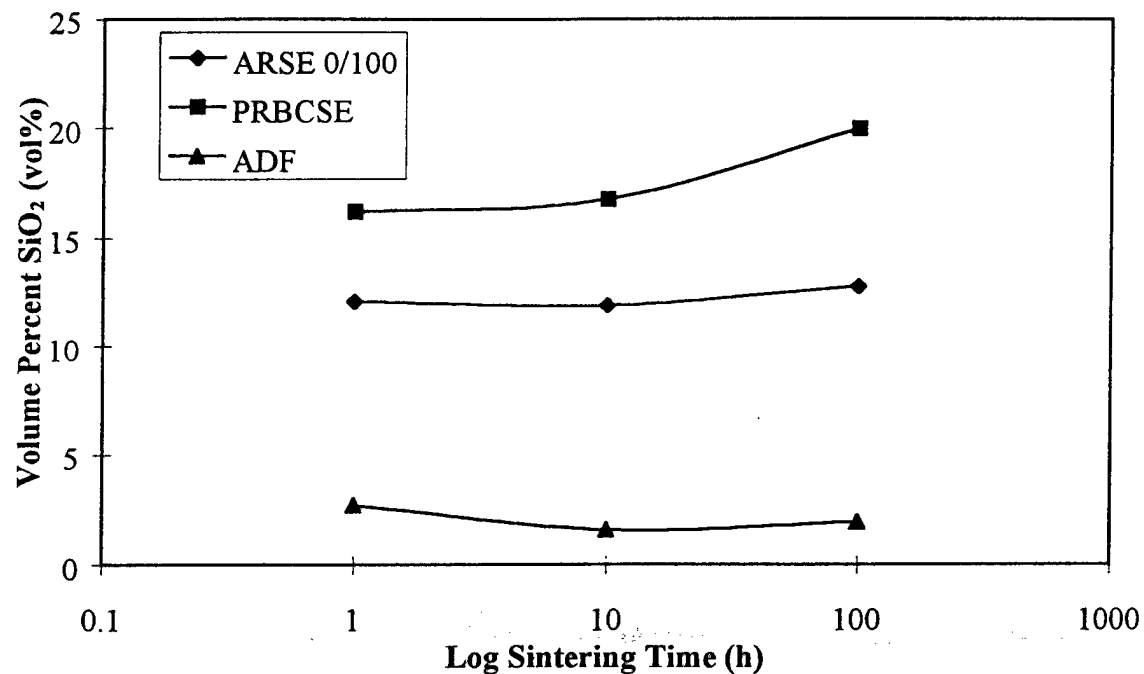
Figure 30: Volume percent SiO_2 vs. Sintering time for the samples sintered on SiC disks at 1700 °C. Obtained from oxygen EDS dot maps.
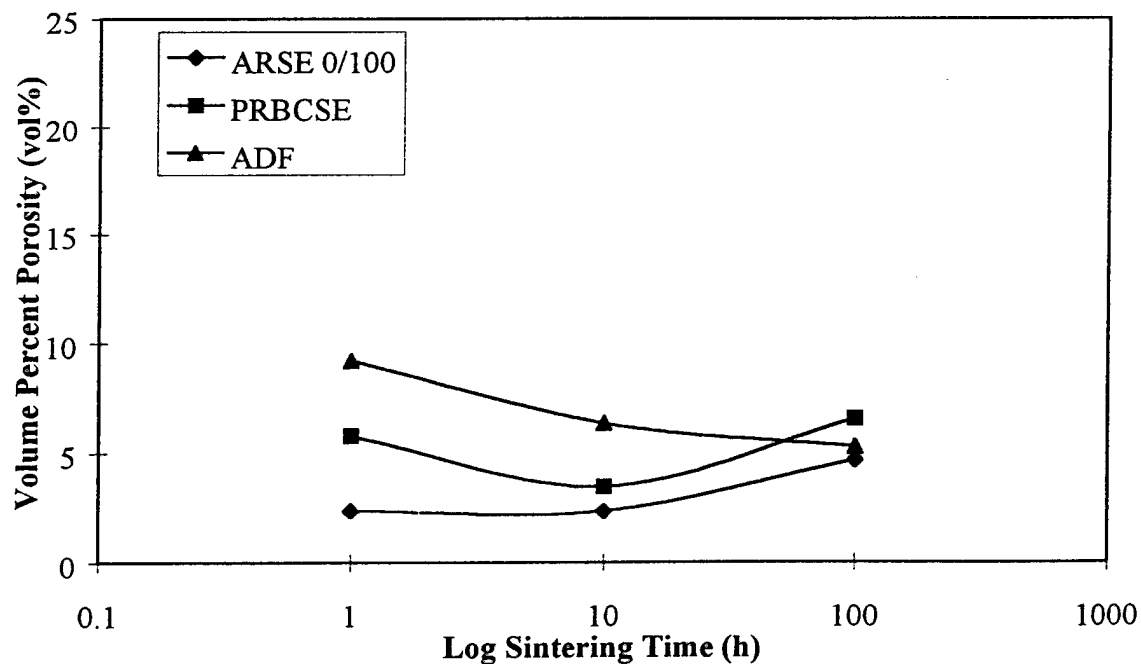
Figure 31: Volume percent porosity vs. Sintering time for the samples sintered on SiC disks at 1700 °C. Calculated by subtracting the SiO_2 volume percent obtained by oxygen EDS dot mapping from the SiO_2 and pore volume percent obtained by optical microscopy.
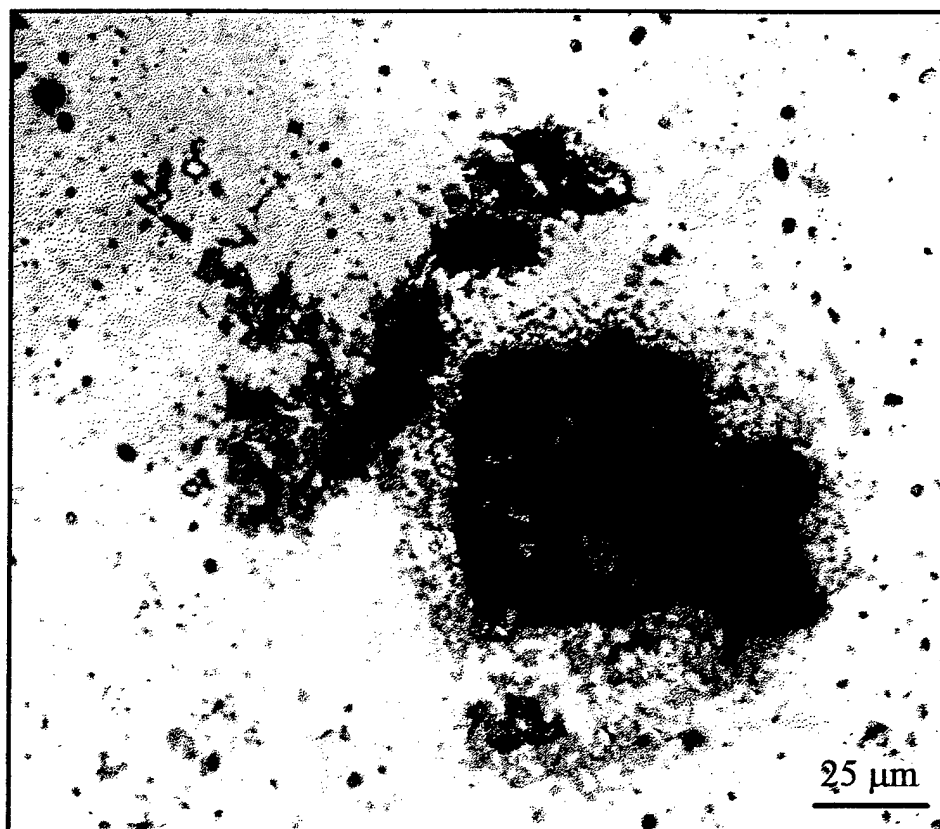
Figure 32: Optical micrographs of as-received, PRBCSE, sintered at 1700 °C for 1 h. Notice that the SiC (gray phase) forms at pores.

41

powder was made using a slurry process there was probably some agglomeration of the resin before pyrolysis leaving an uneven distribution of C. Figure 32 shows that the carbon did not evenly coat the $MoSi_2$ particles because the SiC_p (gray phase) formation occurred at a pore.

The grain size of the ball-milled PRBCSE samples was much smaller and more uniform than the not ball-milled samples (fig. 33). This can be attributed to the more evenly dispersed carbon and smaller $MoSi_2$ particle size observed in the ball-milled samples. Ball-milling reduced the particle size, broke up the SiO_2 layer that was present in the starting powder and produced more SiO_2 on the smaller ball-milled $MoSi_2$ particles giving a higher SiO_2 content in the final sintered samples.

5.2 Phase Identification

Scanning electron microscopic and EDS observations on an as-received PRBCSE sample sintered at 1700 °C for 1 h are shown in fig. 34. Figure 34a shows a region near a sintering induced void at which SiC formed preferentially because of an uneven distribution of carbon in the starting powder which was explained in section 5.1.4. Spot EDS spectra of regions marked 1, 2, and 3 in fig. 34a are shown in fig. 34b. Region 1 is Si rich and there is no Mo, which implies that this could be one of two phases, either SiO_2 or SiC. Since the sample was not coated for SEM examination, one can eliminate the possibility of SiO_2 because it is not conductive and thus would cause charging. Since no charging was observed, it would appear that region 1 was SiC. Region 2 is likely to be $MoSi_2$ because this was the most abundant phase found in the sample. The EDS spectrum of this region shows that the intensity of the Si peak is higher than that of the Mo peak, implying that qualitatively there was more Si than Mo

42
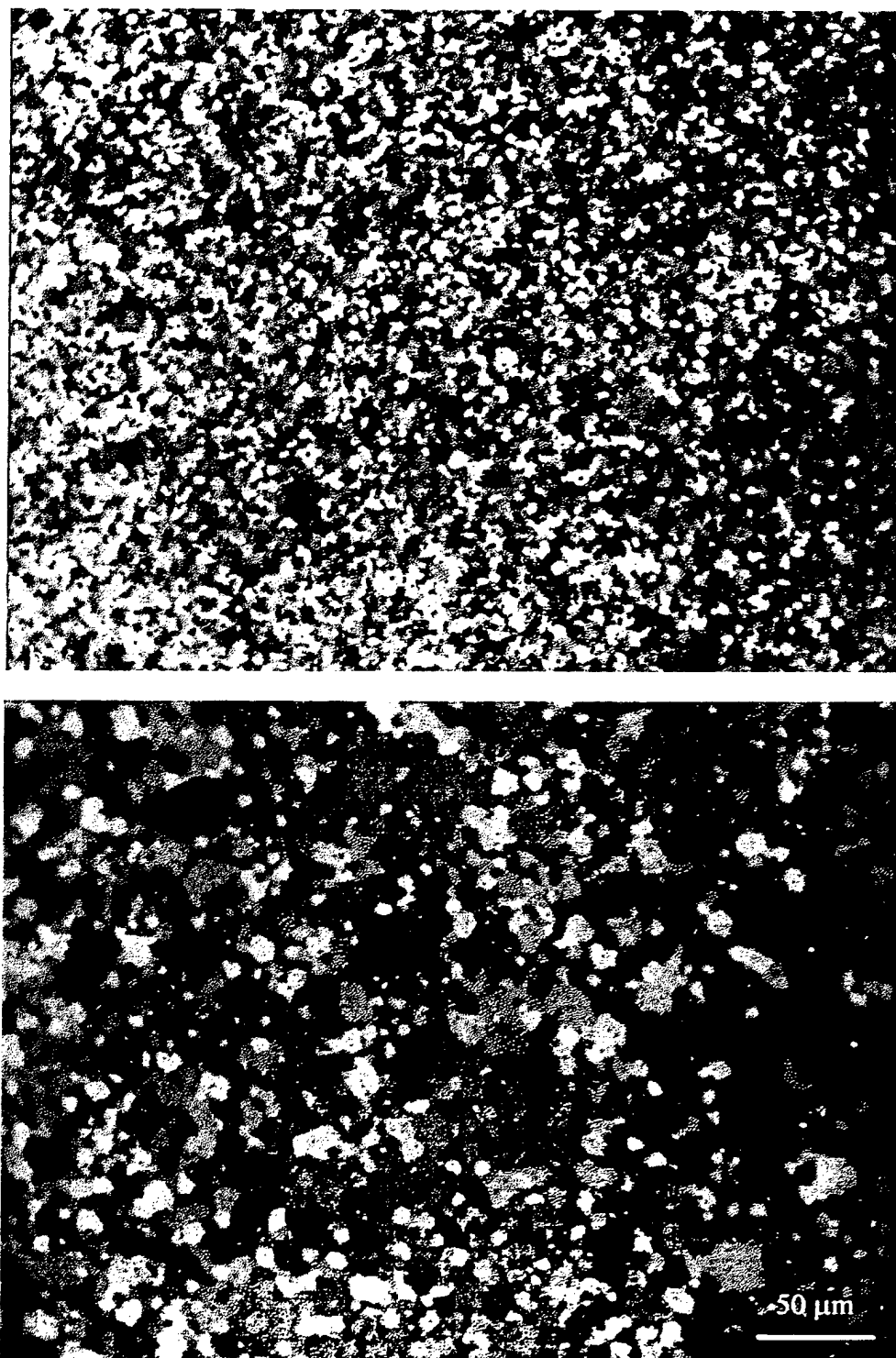
Figure 33: Optical micrographs of PRBCSE sample sintered at 1700 °C for 1h, **a. ball-milled** and b. not ball-milled. Notice the smaller and more consistent **grain** sizes found in the ball-milled sampled compared to the not ball-milled sample.
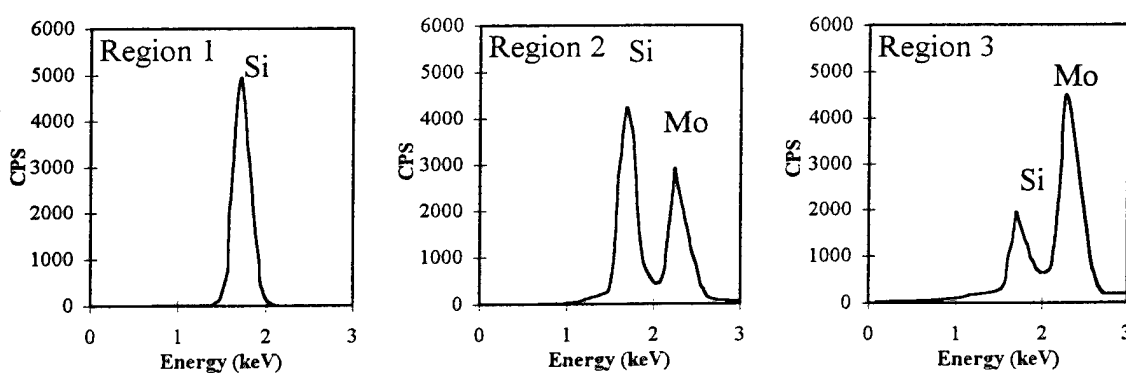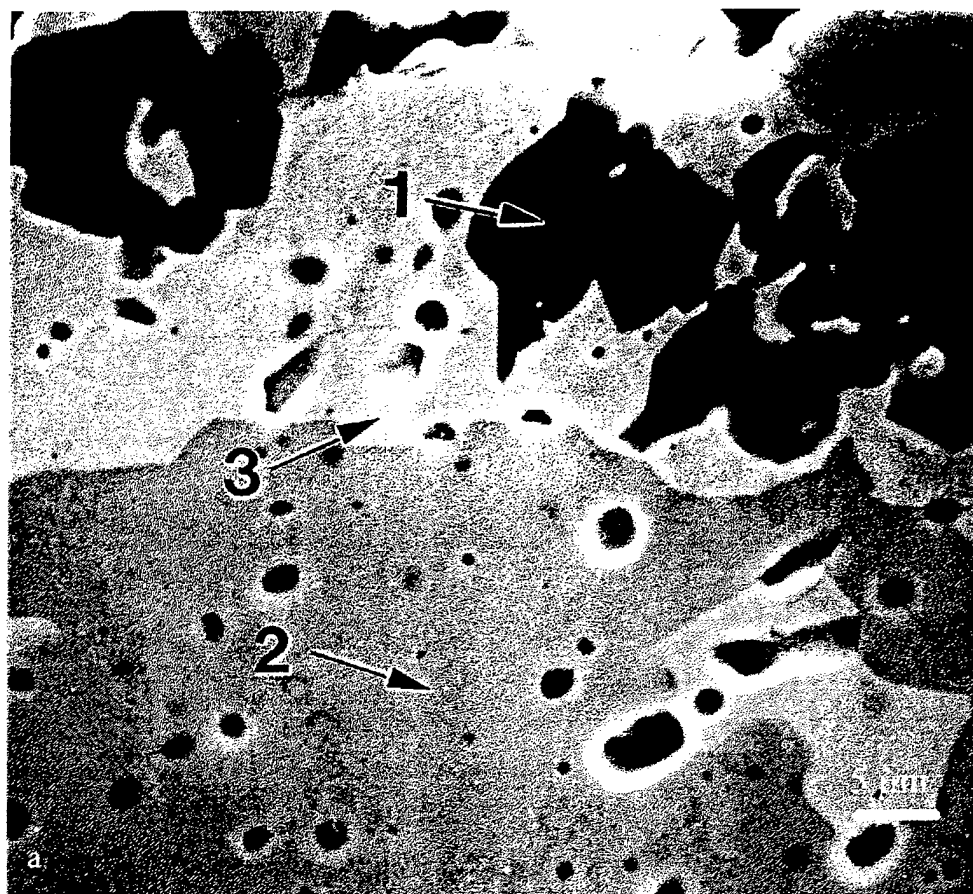
Figure 34: a. SEM micrograph of the PRBCSE, as-received, sintered at 1700 °C for 1 h.
EDS spectra for regions marked 1, 2, and 3 in a. and b. Regions 1, 2, and 3
probably correspond to SiC, $MoSi_2$, and $Mo_{\sim4.8}Si_3C_{\sim0.6}$, respectively.

in region 2 which would be the case for $MoSi_2$. Keeping this in mind, if we examine the EDS

spectrum for region 3, we can see that the Mo peak is higher than the Si peak, which implies

that there is more Mo in this region than Si which could correspond to Mo_5Si_3 or the Nowotny

phase, $Mo_{\leq4.8}Si_3C_{\leq0.6}$. The yield of secondary electrons increases with increasing average

atomic number, Z, which means that the intensity will increase with increasing Z. Region 3

was brighter than the region 2 which confirmed the fact that region 2 had a lower average

atomic number than region 3 which would be the case if region 2 were $MoSi_2$ (average atomic

number for $MoSi_2$ is 23.3), and region 3 was Mo_5Si_3 (average atomic number is 31.5) or

$Mo_{\leq4.8}Si_3C_{\leq0.6}$ (average atomic number is 29.4). If one compares the brightness of region 1

(i.e., possibly SiC) to regions 2 and 3 one can see that it is much darker indicating that this

region has a much lower average atomic number (average atomic number for SiC is 10) which

is consistent with the possibility that this is SiC. One can thus tentatively say that regions 1, 2,

and 3 correspond to SiC, $MoSi_2$, and $Mo_{\leq4.8}Si_3C_{\leq0.6}$ or Mo_5Si_3, respectively, but light element

detection EDS and WDS was needed to verify these results, which are presented below.

Electron microprobe analysis involving both light element detection EDS and WDS

was done on an ADF sample sintered at 1700 °C for 10 h. Specta software developed by

Oxford Analytical was used for the WDS analysis which uses a ZAF (atomic number,

absorption, and fluorescence) correction to determine atomic percentages of elements in

compounds. The light element detection EDS results showed that the brightest phase (i.e.,

Region 3 in the previous micrograph) in the secondary electron micrographs contained Mo, Si,

and C which indicated that this phase was the Nowotny phase and not Mo_5Si_3 (see fig. 35).

Similar results were obtained by Costa e Silva *et al.* [32] for powder compositions in the same

region on the ternary phase diagram (i.e., $MoSi_2$, SiC, and $Mo_{\leq4.8}Si_3C_{\leq0.6}$). The light element

45
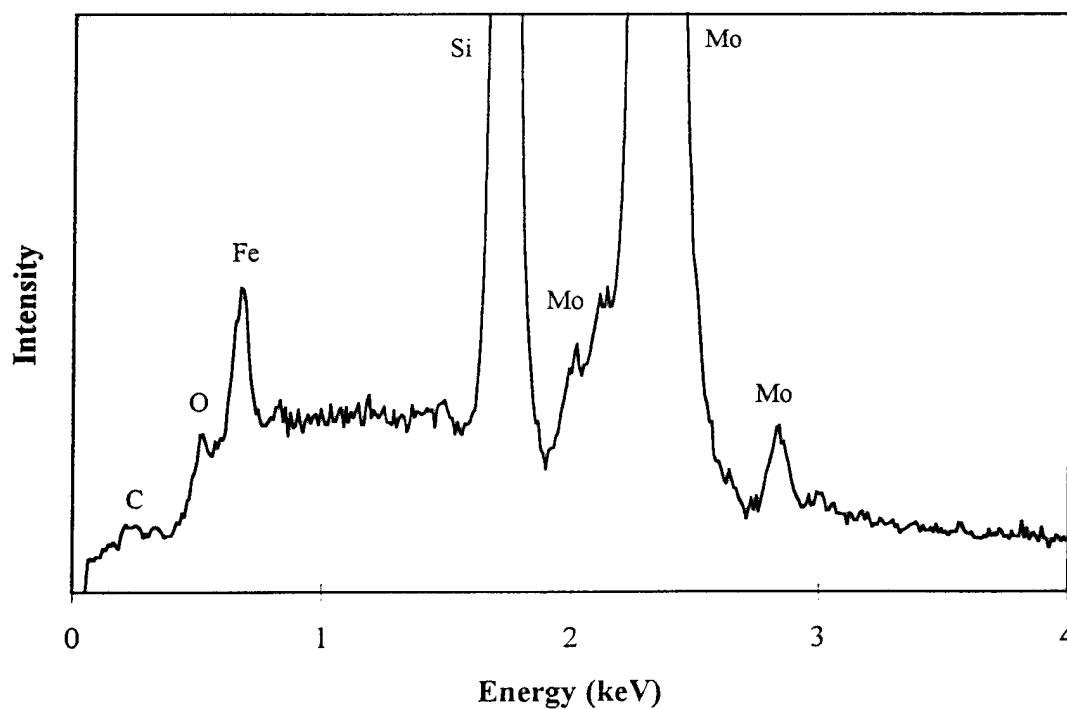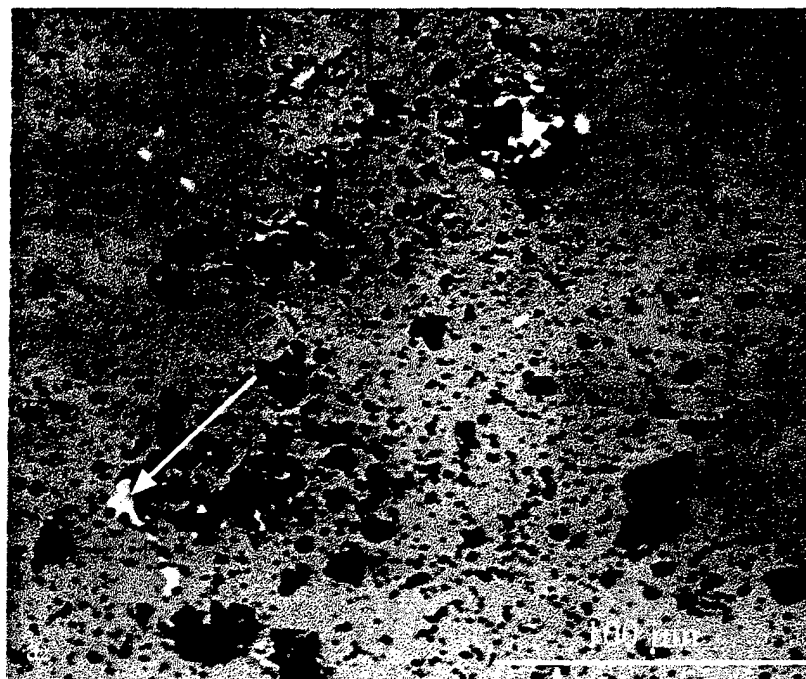
b.

Figure 35: a. SEM micrograph of aqueous dispersion flocculation powder sintered at
1700 °C for 10 h. Arrow indicates area analyzed. b. EDS spectrum of the
region analyzed. The spectrum shows that there is Mo, Si, and C indicating
that this region is the Nowotny phase.

46

detection WDS results from this same compound indicated that it was indeed the Nowotny phase with $Mo_{4.7}Si_3C_{0.56}$ stoichiometry, see Table 9. The darkest region in fig. 34a which was thought to be SiC showed only Si and C using the light element detection EDS (see fig. 36). The light element detection WDS analysis of the same region indicated that the stoichiometry was not perfect but was $SiC_{0.86}$. This may be caused by noise coming from the matrix which would lead to a higher Si in the compound. Although SiC and $Mo_{\le 4.8}Si_3C_{\le 0.6}$ were not detected by XRD, the ternary phase diagram developed by Nowotny [12] indicates that the compositions for the powders used should produce these phases at a temperature of 1600 °C (See Appendix 1, fig. A1).

The powder compositions and the Nowotny phase diagram were used to calculate the theoretical final composition of the sintered samples. Oxygen (O_2) content that was used for the calculation was determined by Kruse [33] and was reported to be 2.41 wt%. The details of this calculation are given in Appendix 1 and the results are shown in fig. 37. The results indicate that there should be a significant amount of both SiC and $Mo_{\le 4.8}Si_3C_{\le 0.6}$. The actual samples showed only trace amounts of each phase compared to what was calculated. The chemical reaction used in the calculation assumed that O_2 gas would

Table 9: Compositional data obtained by WDS. Note the composition for SiC is slightly off stoichiometry possibly caused by signal coming from the matrix.

At% Mo	33.726	-	56.935
At% Si	62.692	53.263	36.304
At% C	-	45.670	6.761
Theoretical Composition	$MoSi_2$	SiC	$Mo_{\le 4.8}Si_3C_{\le 0.6}$
Actual Composition	$MoSi_{1.9}$	$SiC_{0.86}$	$Mo_{4.7}Si_3C_{0.56}$
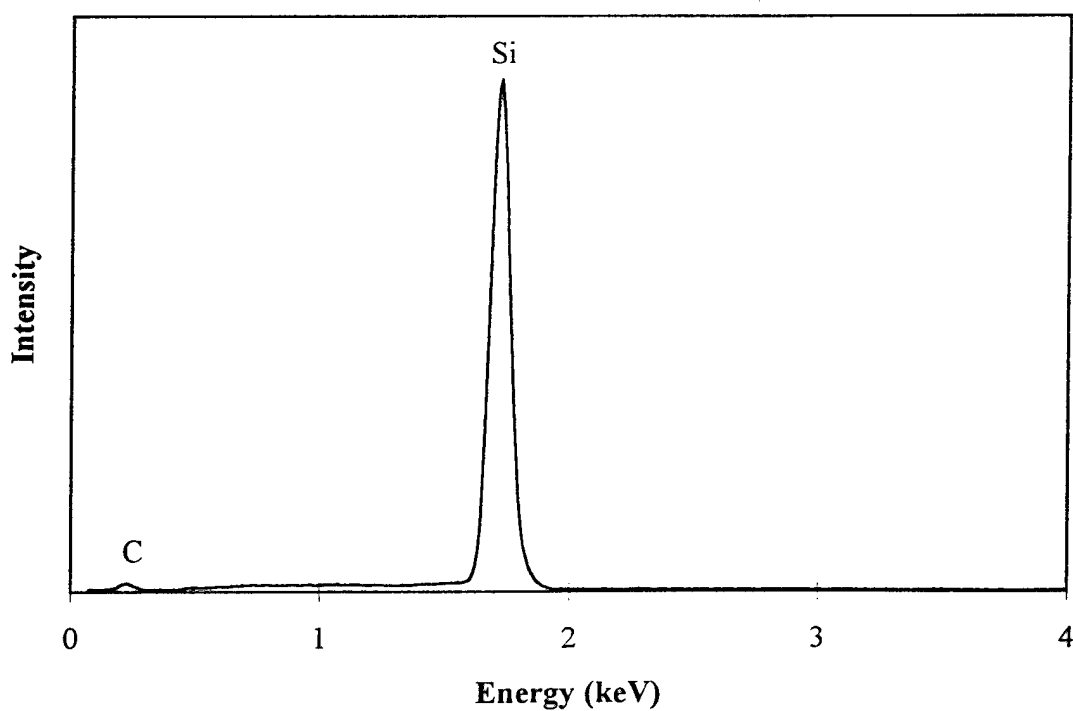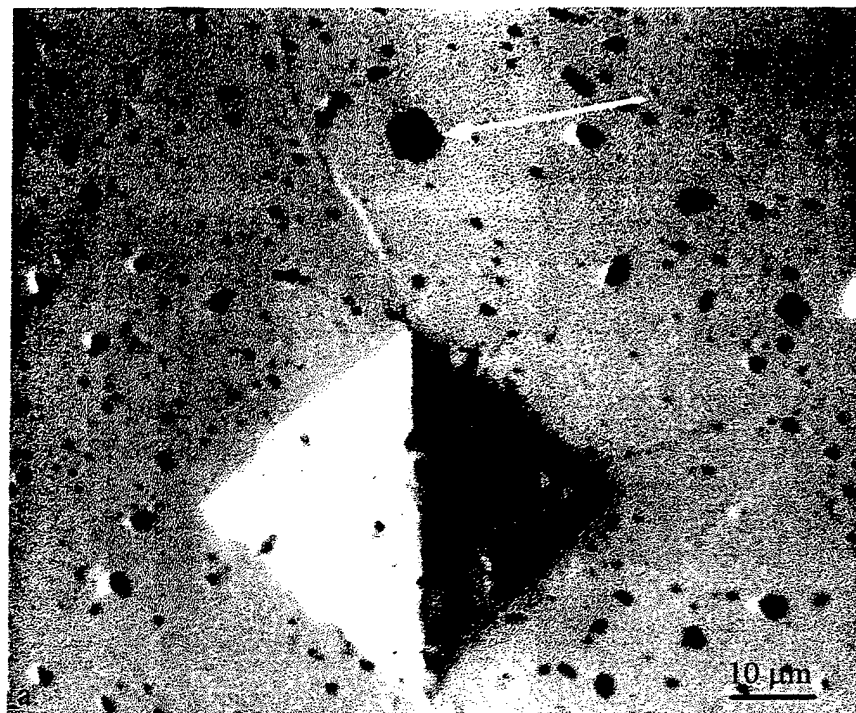
b.

Figure 36:   a. SEM micrograph of aqueous dispersion flocculation powder sintered at 1700 °C for 10 h. Arrow indicates area analyzed. b. EDS spectrum of the region analyzed. The spectrum shows that there is Si, and C indicating that this region is $SiC_{0.86}$.
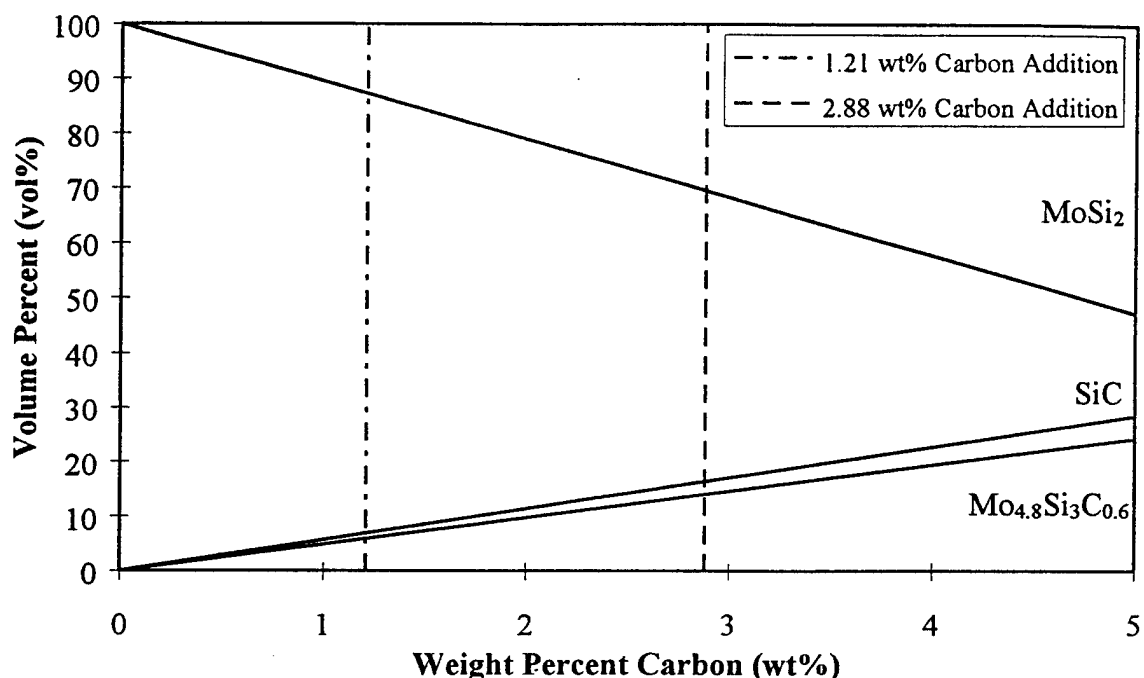
Figure 37:   Volume percentage of phases vs. weight percentage of carbon content
calculated by using the Nowotny ternary phase diagram.

be produced from the reaction and the production of CO or CO_2 was not considered. The

thermodynamics of the reaction could not be quantified because the reaction took place in Ar

and most thermodynamic data are for reactions in air. Thermodynamic data concerning the

Nowotny phase are also not available indicating that only a guess could be made about the

reaction. The carbon in the starting powders could have been oxidized by trace amounts of O_2

in the vacuum used thus reducing the amount of carbon. This would give a lower amount of

SiC and the Nowotny phase.

Optical micrographs were used to determine how much SiC was formed in the ADF

samples sintered at 1700 °C for 100 h (fig. 38). This sample contained more SiC_p than all of

the other samples and contained only 1.4 vol%. This indicates that the reaction used in the
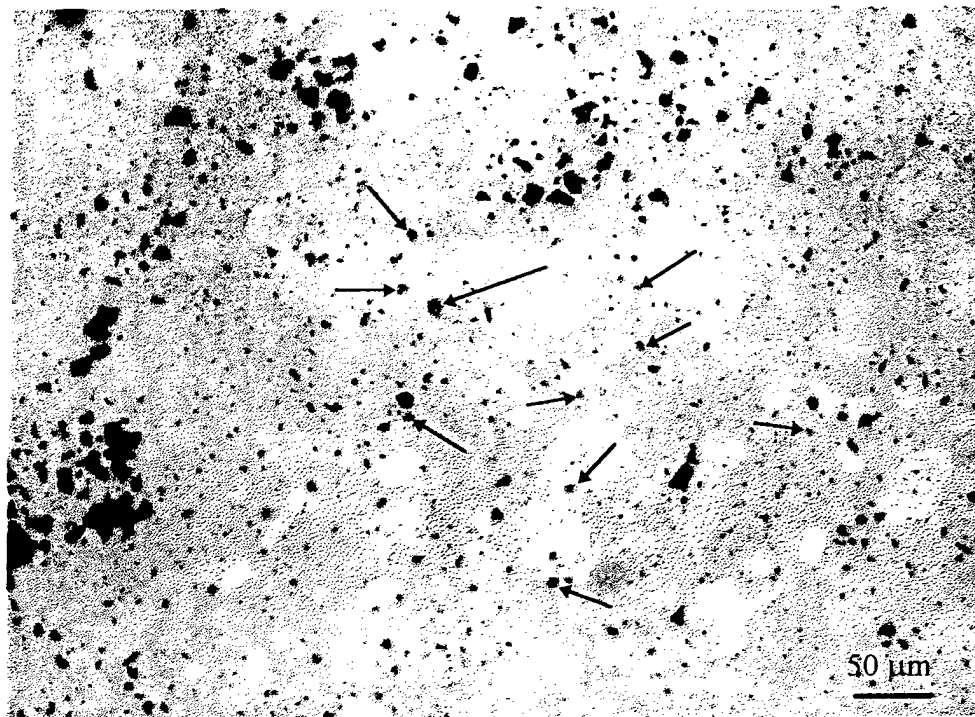
Figure 38:   Typical micrograph used to determine the volume fraction of SiC_p in an ADF processed sample sintered at 1700 °C for 100 h. The average volume percentage was 1.4 % SiC_p. Arrows show SiC_p.

theoretical analysis probably needs to be considered for CO and CO_2 or a combination of O_2, CO, and CO_2.

5.3 Mechanical Properties

5.3.1 Vickers Hardness

The results of Vickers indentation tests are shown in figs. 39 through 41. The ADF samples were not evaluated for hardness because of microstructural problems which consisted of inconsistently sized grains and an uneven distribution of porosity. All of the samples sintered at 1800 °C showed dramatic decreases in hardness with increasing

50

Figure 39:   Vickers hardness vs. sintering time for the ARSE 70/30 samples sintered at various temperatures. 1700-SiC represents samples sintered at 1700 °C on SiC disks, all others were embedded in 50 wt% $MoSi_2$ / 50 wt% BN.

Figure 40:   Vickers hardness vs. sintering time for the ARSE 0/100 samples sintered at various temperatures. 1700-SiC represents samples sintered at 1700 °C on SiC disks, all others were embedded in 50 wt% $MoSi_2$ / 50 wt% BN.

Figure 41: Vickers hardness vs. sintering time for the PRBCSE samples sintered at various temperatures. 1700-SiC represents samples sintered at 1700 °C on SiC disks, all others were embedded in 50 wt% $MoSi_2$ / 50 wt% BN.

sintering time. This was clearly caused by an increase in grain size with increasing sintering time associated with these samples (figs. 19 through 21).

The hardness of all the ARSE 70/30 samples embedded in the $MoSi_2$/BN powder and on the SiC disks sintered at 1600 and 1700 °C was more or less constant. This was attributed to relatively slow grain growth at these temperatures. The hardness of the ARSE 0/100 and the PRBCSE samples sintered in the $MoSi_2$/BN embedding powder decreased with sintering time. The decreases in hardness with increasing sintering time can be directly attributed to the increases in grain size with increasing sintering time (figs. 19 through 22). The ARSE 0/100 and PRBCSE samples sintered on the SiC disks showed rather slow grain growth at 1600 and 1700 °C which explains the relatively constant hardness with increasing sintering time.
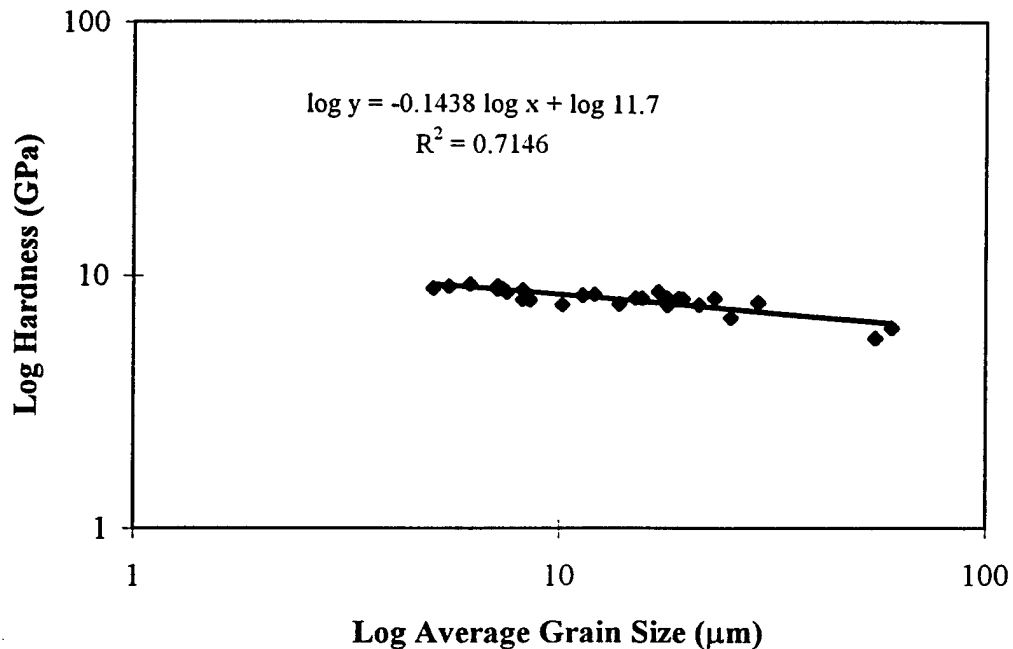
Figure 42: Vickers hardness vs. Grain size for all the samples. Note that hardness decreased with increased grain size, as expected.

In general, mechanical properties such as hardness and strength decrease with increasing grain size [34]. In order to evaluate the effect of grain size on hardness, a log-log plot is shown in fig. 40. The trend seems to follow,

$$H = 11.7 \, d^{-0.14}$$

H is the hardness, and d is the grain size. Spriggs *et al.* [35] studied the effect of grain size on the strength of hot pressed polycrystalline Al_2O_3 and found that the exponential term varied from -0.25 to -0.5. A correlation between the exponential term and a physical mechanism was not established. All that fig. 42 indicates is a decrease in hardness with increasing grain size, which is a fairly well accepted experimental fact. If SiC_p are present in sufficient amounts and act as grain boundary pinning agents, then one could expect a strengthening effect. The exponential term will also be affected by the presence of porosity but the equation used does not account for this.

5.3.2 Fracture Toughness

Fracture toughness was determined using a method developed by Anstis et al. [36]. This method uses various material properties, the diameter and the length of crack emanating from a Vickers indentation. The formula used is as follows,

$$K_C = A\left(\frac{E}{H}\right)^{0.5}\left(\frac{P}{c^{1.5}}\right)$$

where A is a constant for a Vickers indentor which is 0.016, E is the elastic modulus for polycrystalline $MoSi_2$ which is 440 GPa [37], P is the indentation load, c is the average length of the four radial cracks plus half the average indentation diameter produced by the indentation, and H is the hardness given by,

$$H = \frac{P}{0.5d^2}$$

where d is the average of the two indentation diameters measured from one corner to the opposite corner of the indentation. Figure 43 shows two typical indentations used to determine the crack lengths and indentation diameter. Figure 44 shows two indentations which exhibited microcracking making any measurement for the fracture toughness invalid, thus the fracture toughness of these samples and others similar to this were not evaluated. This method requires that the cracks be straight and unaffected by microstructure and that $c \geq 2a$. Anstis et al.[36] also reported a nominal accuracy better than 30-40% for polycrystalline materials. The values obtained from this analysis should only be used as a comparison with the other fracture toughness values obtained by the same method due to the nature of the method (affected by grain size and porosity).
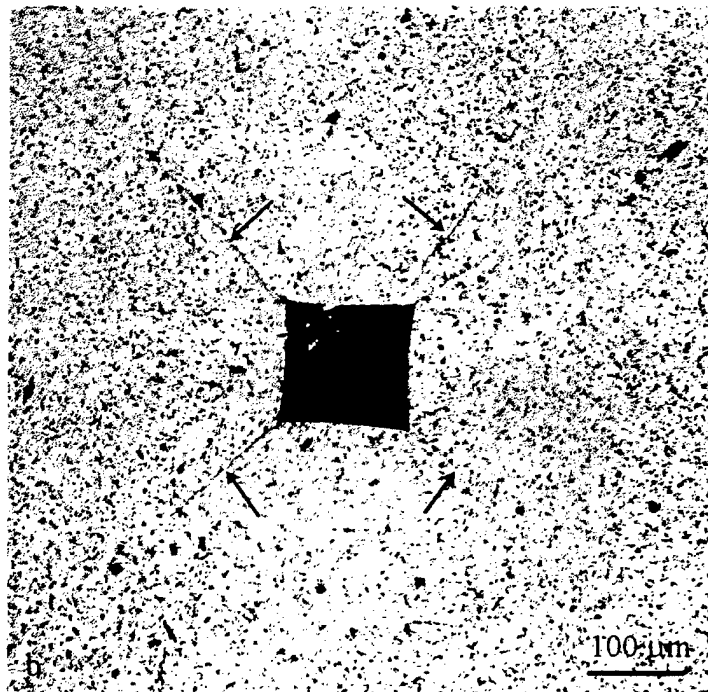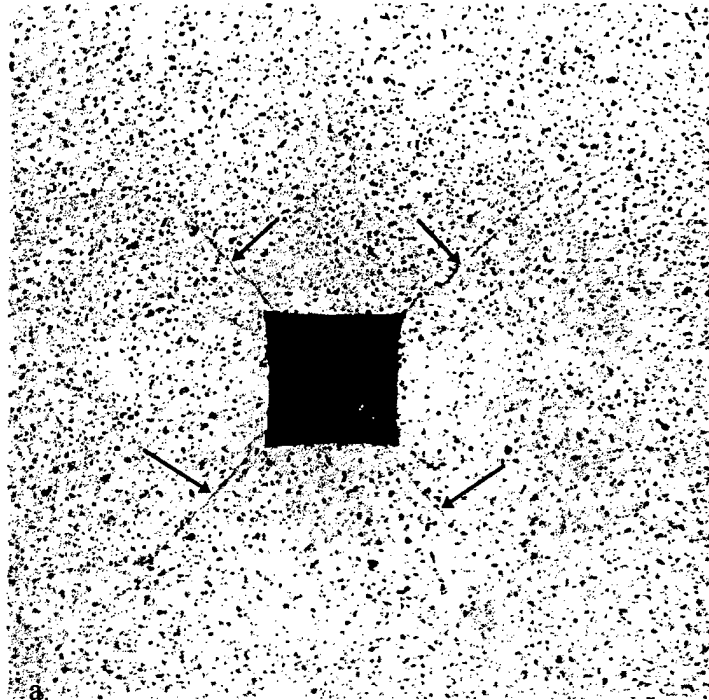
Figure 43: Optical micrographs of Vickers indentations (196 N, 15 s), a. ARSE 0/100, and b. PRBCSE. These cracks were used to calculate the fracture toughness. Arrows show the cracks that were used for the fracture toughness calculation
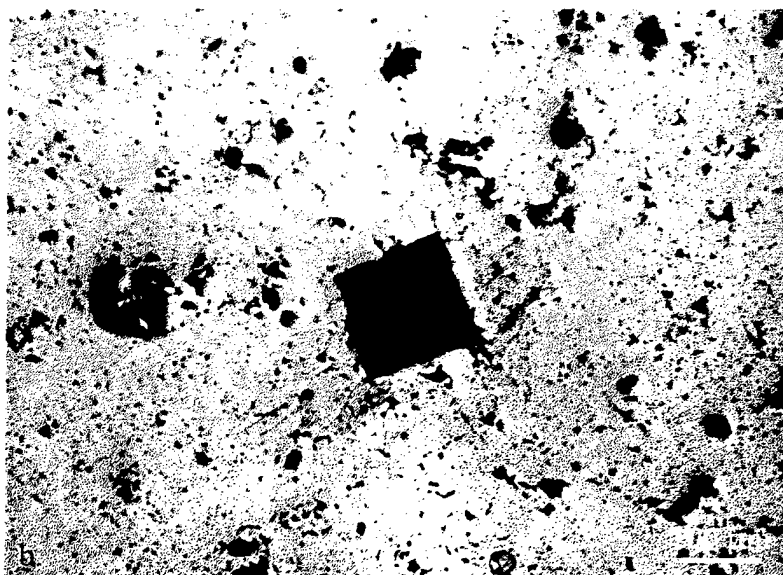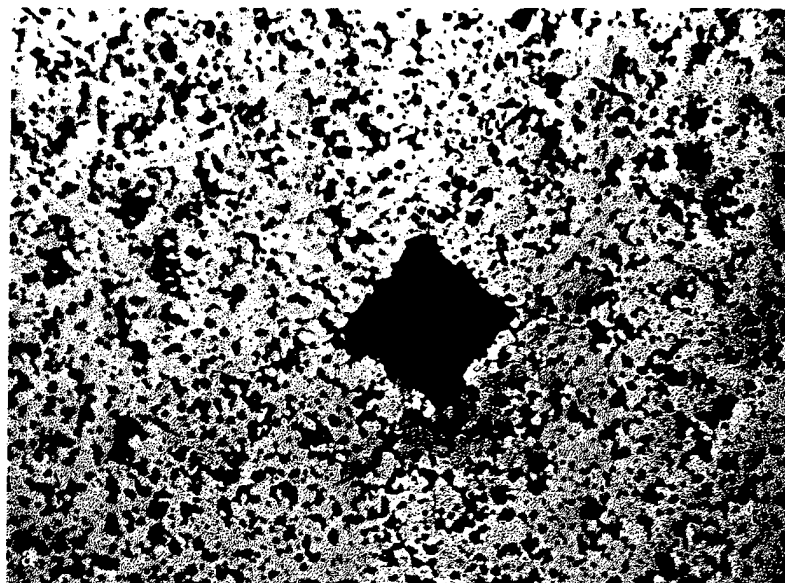
Figure 44: Optical micrographs of Vickers indentations (196 N, 15 s) on samples sintered at 1700 °C for 100 h, a. ARSE 0/100, and b. ADF

The fracture toughness of all the samples, shown in figs. 45 through 47, were relatively constant and near values reported by Bhattacharya *et al.* [7] (see fig. 8). It is clear from these observations that there were not enough SiC_p to affect the fracture toughness of the PRBCSE samples. Increasing the amount of C in the starting sample could yield a higher amount of SiC_p resulting in a higher toughness.

Figure 48 shows interaction between a variety of particles in $MoSi_2$ and a crack formed by a Vickers indentation (1 kg, 15 s). The first unidentified particle stopped the crack and the crack reinitiated on the opposite side. After the crack was reinitiated, it encountered another unidentified particle and the crack deflected around this particle. The crack then penetrated the SiC_p and was arrested there. A new crack was then formed in the SiC_p that propagated into the $MoSi_2$. Such crack deflection and reinitiation would enhance the toughness of the composite.

Figure 49 shows SEM micrographs of two Vickers indentations on an ADF sample sintered at 1700 °C for 100 h. The first micrograph shows a SiC_p that seems to have prevented crack formation. One can see cracks propagating from regions near the corners of the indentation indicating that there may be a compressive stress field surrounding the particle. This would imply that the composite should be tougher than the monolithic sample. The second micrograph shows a crack that propagated through the SiC_p but branched into two cracks. This would indicate a toughening effect of SiC_p because of crack branching, i.e., it needs more energy to drive two cracks than one.
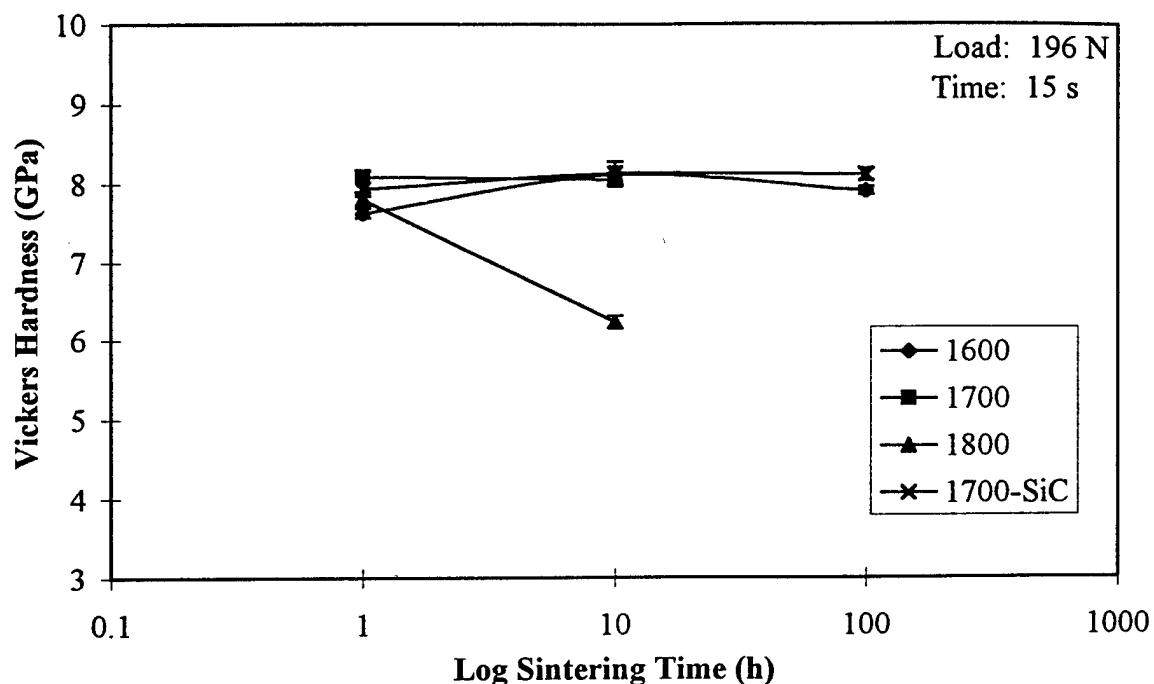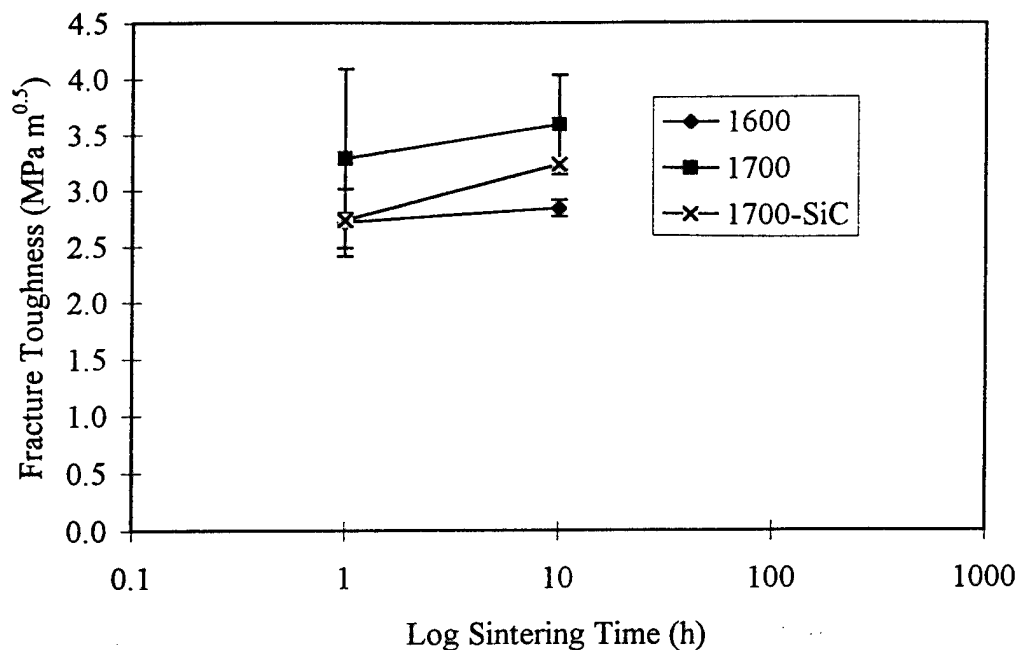
Figure 45: Fracture toughness vs. sintering time for the ARSE 70/30 samples sintered at various temperatures. 1700-SiC represents samples sintered at 1700 °C on SiC disks, all others were embedded in 50 wt% $MoSi_2$ / 50 wt% BN.
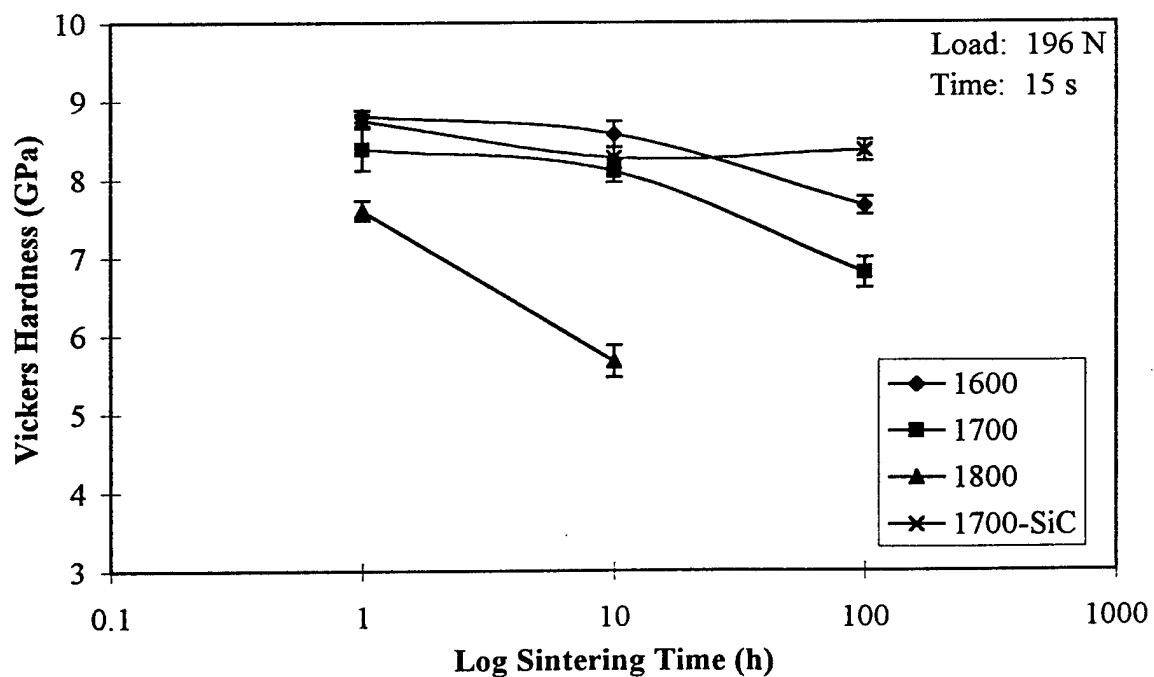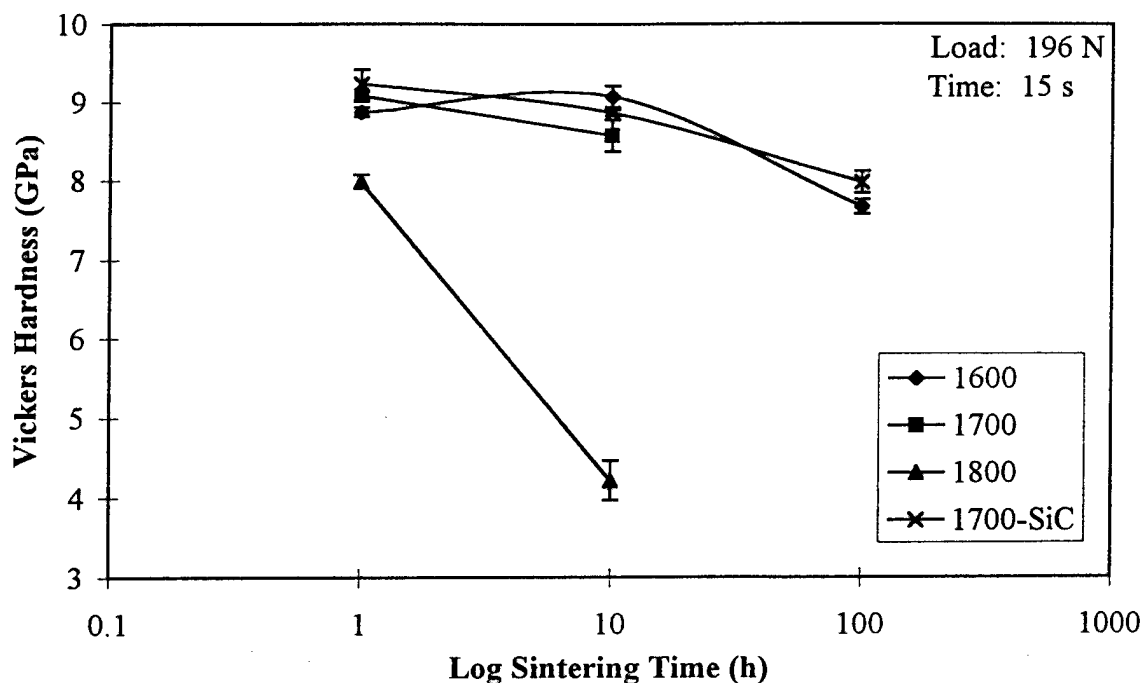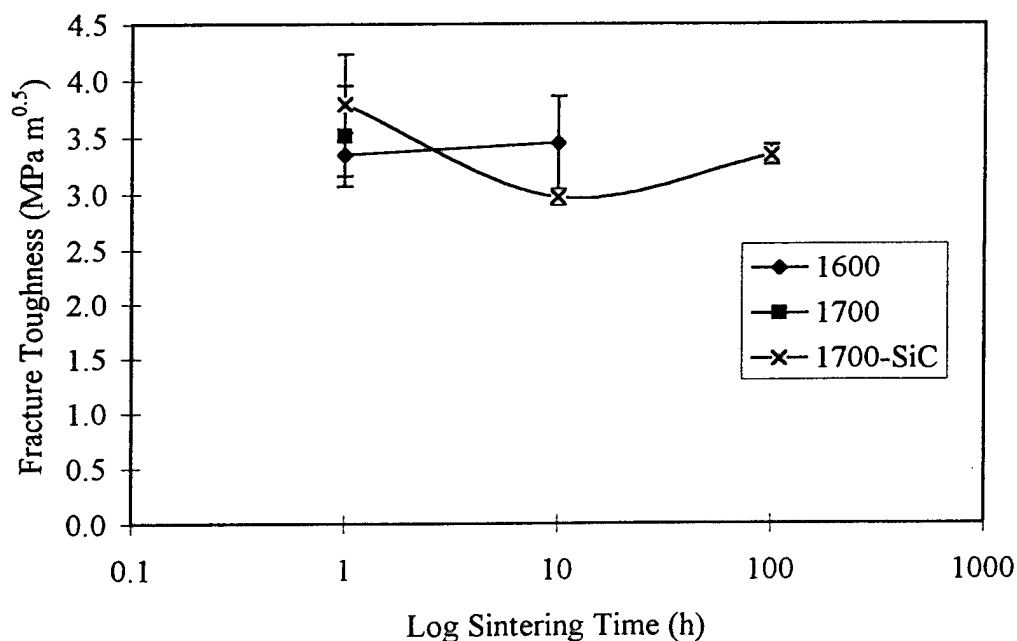

Figure 46: Fracture toughness vs. sintering time for the ARSE 0/100 samples sintered at various temperatures. 1700-SiC represents samples sintered at 1700 °C on SiC disks, all others were embedded in 50 wt% $MoSi_2$ / 50 wt% BN.
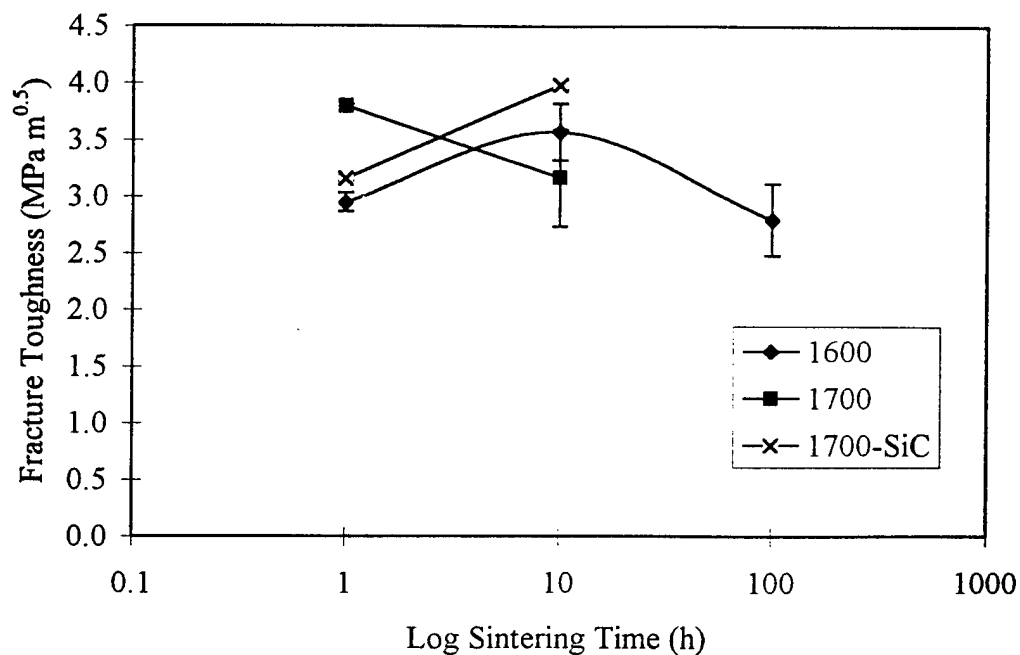
Figure 47: Fracture toughness vs. sintering time for the PRBCSE samples sintered at various temperatures. 1700-SiC represents samples sintered at 1700 °C on SiC disks, all others were embedded in 50 wt% $MoSi_2$ / 50 wt% BN.
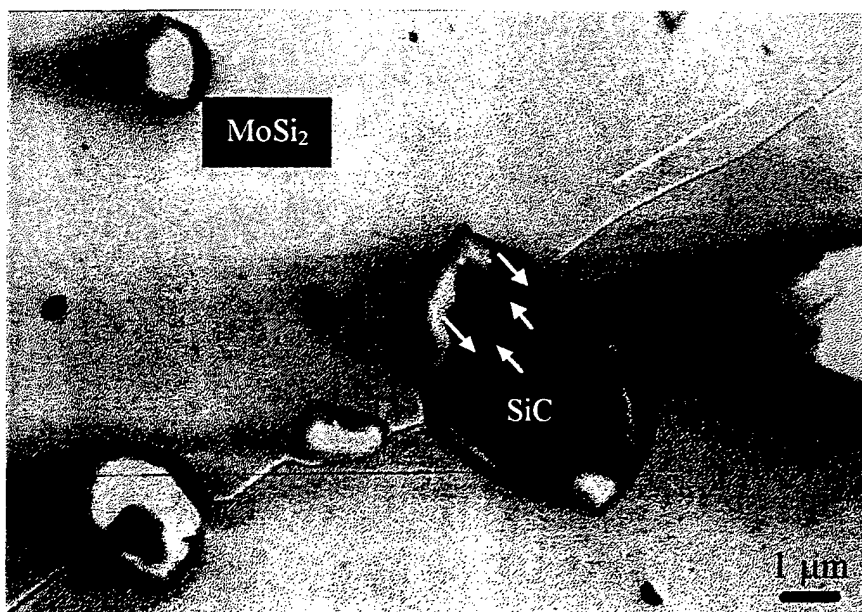
Figure 48: SEM micrograph of a crack produced using a Vickers indentor. Notice that the SiC_p deflects the crack. The arrow in the optical micrograph points to the SiC_p in the SEM micrograph. Long arrow indicates the direction of the crack propagation.

59
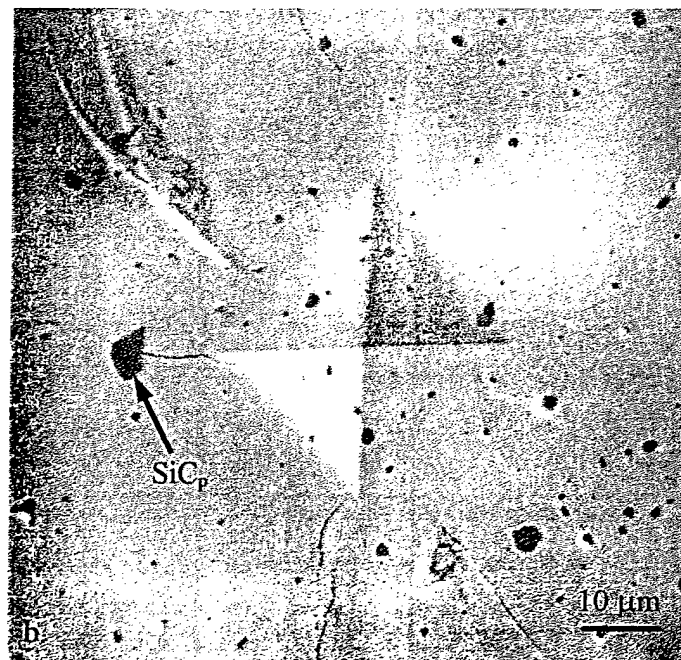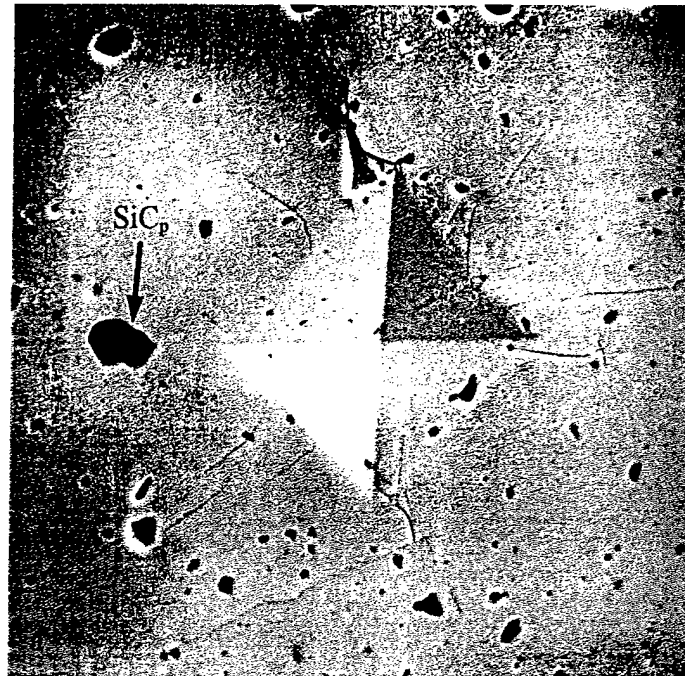
Figure 49: Vickers indentations used to observe SiC_p crack interaction in an ADF sample sintered at 1700 °C for 100h. a. shows cracks avoiding the SiC_p possibly caused by a stress field. b. shows crack propagating straight through an SiC_p

60

6. Discussion

The idea of reactive processing of $MoSi_2$ to reduce SiO_2 formation and produce a SiC_p reinforced composite is a promising one, but more work needs to be done to realize the potential. The elimination of SiO_2 was certainly accomplished with minimal amounts of carbon. However, the SiC_p was not formed in amounts large enough to consider the resultant product a true composite. The reactive processing can certainly be used as a scavenging process to reduce the amount of SiO_2 which should improve creep resistance by eliminating easy grain boundary sliding. The pressureless sintering approach, although more economical, produced large macrocracks in the sintered monolithic material and in the PRBCSE processed samples. However, the ADF processed samples showed promise in terms of macrocracking but need to be cold-pressed to a higher pressure which may reduce some of the excessive porosity found in those samples.

The Nowotny phase ($Mo_{\leq 4.8}Si_3C_{\leq 0.6}$) was identified using EDS and WDS and had a stoichiometry of $Mo_{4.7}Si_3C_{0.56}$. Although increasing the carbon addition would increase the amount of SiC_p, it is also likely to increase the amount of the Nowotny phase.

The bimodal ARSE 70/30 powder showed higher green and sintered densities and look promising with pressureless sintering. If used in conjunction with either the PRBCSE or ADF processing it would probably yield a better sample than the monomodal powder used.

The effects of ball-milling were detrimental in terms of SiO_2 content because the ball-milling reduced the particle size of the powders, exposing more surface area resulting in higher SiO_2 content in the starting powder.

The MoSi$_2$/BN embedding material caused the samples to form a MoB surface coating and caused the samples to melt when sintered at 1800 °C for 100 h. The samples sintered at 1800 °C for 1 and 10 h showed significantly higher grain growth rates than the samples sintered at 1600 and 1700 °C. The MoB contamination could be reduced by using less BN in the embedding powder which was added to prevent the MoSi$_2$ embedding powder from sintering. The SiC disks exhibited no contamination and a more consistent microstructure making this the embedding material of choice over the MoSi$_2$/BN embedding powder.

The indentation technique to determine fracture toughness was designed for unreinforced ceramics. Thus, the values obtained in this work can only be used as an approximation. Inaccuracies can also be attributed to the cracks not generally initiating from the corners of the indentation, microcracking, and the fact that the cracks were generally not straight and there were significant amounts of porosity. To accurately determine the fracture toughness more large scale testing would need to be done (i.e., 4-point bend or 3-point bend with a chevron-notch). The fracture toughness values obtained were in the range of unreinforced MoSi$_2$. This is due to the fact that there was not enough SiC$_p$ to make an appreciable difference in fracture toughness and more C needs to be added to the starting powder to produce more SiC$_p$.

A qualitative assessment of the effect of the SiC$_p$ showed that cracks either deflect away from SiC$_p$ indicating that the SiC$_p$ may have a stress field associated with it, or crack branched, thus contributing to dissipation of energy in the fracture. Both of these situations should enhance the fracture toughness of the bulk material, provided there is enough reinforcement present.

The sintered ADF samples exhibited an uneven distribution of porosity probably left after the pyrolysis of the starch. The sintered ADF samples were first cold pressed with the starch present. The cold pressed samples were then pyrolyzed leaving carbon and voids. In the case of the sintered PRBCSE samples, the phenolic resin was pyrolyzed leaving a carbon coated $MoSi_2$ powder. It was then cold pressed and sintered, thus the porosity was not formed by pyrolysis. The grain size of the sintered ADF samples was also very nonuniform possibly caused by the uneven distribution of porosity. The hardness and fracture toughness results of the ADF samples showed very inconsistent values, attributable to the inhomogeneous microstructure (i.e. porosity and grain size). These results were not included. However, the sintered ADF samples showed much less cracking than all the other samples (probably because of the starch working as a binder). Thus, in principle, it should be possible to use higher pressure levels during cold pressing of ADF samples and produce better material in sufficient quantity to make flexure samples for strength and fracture toughness measurements.

7. Conclusions

From this research the following conclusions can be drawn. The content of SiO_2 was reduced by the reaction of the carbon with SiO_2 as the EDS and WDS results showed. SiC_p and the Nowotny phase were both formed as the Mo-Si-C ternary phase indicated, this was also verified using EDS and WDS.

The bimodal ARSE 70/30 samples showed a higher green density, a higher sintered density, less porosity, and less SiO_2 than the monomodal ARSE 0/100 samples. This indicated that improvements could be attained by using a bimodal base $MoSi_2$ powder instead of the monomodal powder that was used in the powders with carbon.

Ball-milling was detrimental in terms of SiO_2 content because the reduction in particle size produced more overall surface area. This increased the amount of SiO_2 present in the starting powder making it more difficult to reduce its presence appreciably.

Observation of the crack/SiC_p interaction qualitatively indicated that the SiC_p would increase the fracture toughness in the composite samples. However, to obtain a significant increase in bulk fracture toughness more carbon would have to be added to obtain more SiC_p.

8. Suggestions for Future Work

More research needs to be done to obtain an accurate assessment of how the C reacts with $MoSi_2$ (i.e., if O_2, CO, or CO_2 is produced).

More SiC_p needs to be formed to increase the fracture toughness appreciably by increasing the C content in the starting powder or adding SiC artificially.

The Nowotny phase may affect the bulk properties of the composite so more research on its properties needs to be addressed. This will give an assessment of how it will affect the properties of the composite.

Creep experiments need to be carried out to determine if the reduction of SiO_2 and the presence of SiC_p indeed improves the high temperature creep properties.

A more detailed assessment of the effect of porosity on the hardness should be done to determine its effects on the properties of the samples. Three-point and four-point bend tests should be carried out to obtain a more accurate assessment of the fracture toughness than by simply using the Vickers indentation.

9. References

1. Vasudevan, A. K., and Petrovic J. J., editors, "High Temperature Structural Silicides: Proceedings of the First High Temperature Silicides Workshop," Elsevier Science Publishers, Amsterdam, (1992).

2. Bizzari, V., Linder, B., and Lindskog, N. "Molybdenum Disilicide Heating Elements: Meeting Advanced Ceramics Requirements," American Ceramic Society Bulletin, Vol. 68, pp. 1834-1841 (1989).

3. Bose, S., "Engineering Aspect of Creep Deformation of Molybdenum Disilicide," Materials Science and Engineering, Vol. A155, pp. 217-225 (1992).

4. Cook, J., Khan, E. L., and Mahapatra, R. "Oxidation of $MoSi_2$-based Composites," Materials Science and Engineering, Vol. A155, pp. 183-198 (1992).

5. Cook, J., Mahapatra, R., Lee, E. W., Khan, A. and Waldman, J., "Oxidation Behavior of $MoSi_2$ Composites," Ceramic Engineering Science Proceedings, Vol. 9-10, pp. 1656-1670 (1991).

6. Wade, R. K. and Petrovic, J. J. "Processing Temperature Effects on Molybdenum Disilicide," Journal of American Ceramics, Vol.75, pp. 3160-62 (1992).

7. Bhattacharya, A. K., and Petrovic, J. "Hardness and Fracture Toughness of SiC-particle Reinforced $MoSi_2$ Composites," Journal of American Ceramic Society, Vol. 74, pp. 2700-703 (1991).

8. Boldt, P. H., Embury, J. D., and Weatherly, G. C., "Room Temperature Microindentation of Single-crystal $MoSi_2$," Materials Science and Engineering, Vol. A155, pp. 251-258 (1992).

9. Ghosh, A. K., and Basu, A., "The Effect of Grain Size and SiC Particulate on the Strength and Ductility of $MoSi_2$," Materials Research Society Symposium Proceedings, Vol. 322, pp. 215-222 (1994).

10. Fitzer, E. "Molybdandisilizid als Hochtemperaturwerkstoffe," Warmfest und Korrosionbestandige Sinterwerkstoffe, 2nd Plansee Seminar, June 19-23, (1955).

11. Berztiss, D. A., Cerchiara, R. R., Gulbransen, E. A., Pettit, F. S. and Meier, G. H., "Oxidation of $MoSi_2$ and Comparison with Other Silicide Materials," Materials Science and Engineering, Vol. A155, pp. 165-181 (1992).

12. Nowotny, H., Parthe, E., Kieffer, R., and Benesovsky, F., "Das Dreistoffsystem: Molybdan-Silizium-Kohlenstoff," Monatshefte fur Chemie, Vol. 85, pp. 255 (1954).

13. Gokhale, A. and Abbaschian, G. J., "The Mo-Si (Molybdenum-Silicon) System," Journal of Phase Equilibria, Vol. 12, pp. 493-498, (1991).

14. Parthe, E., Jeitschko, W., and Sadagopan, V., "A Neutron Diffraction Study of the Nowotny Phase $Mo_{\leq 5}Si_3C_{\leq 1}$," Acta Crystallographica, Vol. 19, pp. 1031-1037, (1965).

15. Thibauld, N. W., "Morphological and Structural Crystallography and Optical Properties of Silicon Carbide (SiC)," American Mineralogist, Vol. 29, No. pp. 327-362, (1944).

16. Olesinski, R. W. and Abbaschian, G. J., "The C-Si (Carbon-Silicon) System," Bulletin for Alloy Phase Diagrams, Vol. 5, pp. 486-89, (1984).

17. McCarron, E. M., "β-MoO_3: A Metastable Analogue of WO_3," Journal of the Chemical Society, Chemical Communications, pp. 336-338, (1986).

18. Wade, R. K. and Petrovic, J. J., "Fracture Modes in $MoSi_2$," Journal of American Ceramic Society, Vol. 75, pp. 1682-84 (1992).

19. Cherniack, G. B. and Elliot, A. G., "High-Temperature Behavior of $MoSi_2$ and Mo_5Si_3," Journal of American Ceramic Society, Vol. 47, pp. 136-41 (1964).

20. Gokhale, A. B. and Abbaschian, G. J., "Molybdenum-Silicon," in Binary Alloy Phase Diagrams, Vol. 2, pp. 1631-32 Edited by Massalski, T. B. American Society for Metals, Metals Park, OH, (1986).

21. Maloy, S. A., Lewandowski, J. J., Heuer, A. A., and Petrovic J. J., "Effects of C Additions on the High Temperature Mechanical Properties of Molybdenum Disilicide," Materials Science and Engineering, Vol. A155, pp. 159-163 (1992).

22. Kisly, P. S. and Kodash, V. Y. "The Mullite Coatings of Heaters Made of Molybdenum Disilicide," Ceramic International, Vol. 15, pp. 189-191 (1989).

23. Wirkus, C.D. and Wilder, D. R., "High Temperature Oxidation of Molybdenum Disilicide, Journal of American Ceramic Society, Vol. 49, pp. 173-177 (1966).

24. Richardson, K. K., and Freitag, D. W., "Mechanical Properties of Hot Pressed SiC Platelet-reinforced $MoSi_2$," Ceramic Engineering Science Proceedings, Vol. 12, Vol. 9-10, pp. 1679-1689 (1991).

25. Carter, D. H. , Gibbs, W. S., and Petrovic, J. J., "Mechanical Characterization of SiC Whisker-Reinforced MoSi$_2$," LA-UR_883776, Los Alamos National Laboratory, Los Alamos, NM, November, (1988).

26. Cotton, J. D., Kim, Y. S., and Kaufman, M. J. "Intrinsic Second-phase Particles in Powder-processed MoSi$_2$," Materials Science and Engineering, Vol. A144, pp. 287-291 (1991).

27. Cotton, J. D., Kim, Y. S., and Kaufman, M. J., Department of Materials Science and Engineering, University of Florida, Gainsville, FL 32611.

28. Gac, F. D., and Petrovic, J. J., "Feasibility of a Composite of SiC whiskers in an MoSi$_2$ Matrix," Journal of American Ceramic Society, Vol. 68, C-200-C-201 (1985).

29. Personal communication, Rich Hexemer, Advanced Refractory Technologies, Inc.

30. Pennings, E. C. M. and Grellner, W., "Precise Nondestructive Determination of the Density of Porous Ceramics," Journal of American Ceramic Society, Vol. 72, pp. 1268-70 (1989).

31. ASTM Standard E 112-84, "Standard Methods for Determining Average Grain Size," Annual Book of ASTM Standards, American Society for Testing Materials, Philadelphia, 1986.

32. Costa e Silva, A., and Kaufman, M. J., "Phase Relations in the Mo-Si-C System Relevant to the Processing of MoSi$_2$-SiC Composites," Metallurgical and Materials Transactions A, Vol. 25A, pp. 5-15 (1994).

33. Kruse, S., "The Analysis and Minimization of Oxygen Contamination in the Powder Processing of Molybdenum Disilicide," M.S. Thesis, Iowa State University, April 24, (1994).

34. Knudsen, F. P., "Dependence of Mechanical Strength of Brittle Polycrystalline Specimens on Porosity and Grain Size," Journal of the American Ceramic Society, Vol. 42, pp. 376-387 (1959).

35. Spriggs, R. M., and Vasilos, T., "The Effect of Grain Size and Porosity on the Transverse Bend Strength and Elastic Modulus of Hot Pressed Alumina and Magnesia," as cited by Carnahan, R. D., and Knapp, W. J. in "Ceramics for Advanced Technologies," edited by Hove, J. E., and Riley, W. C., John Wiley & Sons, Inc., New York, NY, pp. 87-90 (1965).

36. Anstis, G. R., Chantikul, B. R., Lawn, B. R., and Marshall, D. B., "A Critical Evaluation of Indentation Techniques for Measuring Fracture Toughness: I,

Direct Crack Measurements," Journal of the American Ceramic Society, Vol. 64, pp. 533-538 (1981).

37. Nakamura, M., Matsumoto, S., and Hirano, T., "Elastic Constants of $MoSi_2$ and WSi_2 Single Crystals," Journal of the American Ceramic Society, Vol. 75, pp. 3160-3162 (1992).

Appendix A

A theoretical analysis was done to quantify the phases present after sintering with the powder compositions, as stated previously. The atomic percentages of Mo, Si, and C contained in each of the powders were calculated assuming there is only $MoSi_2$ and C (See Table A1). The atomic percentages were used to determine what phases should be present at equilibrium using the 1600 °C isotherm ternary phase diagram done by Nowotny [24] (Figure A1). The powder compositions used lie on a tie-line that represents the $MoSi_2$ and C pseudobinary system, shown as a dashed line in Figure A1. All the powder compositions used lie in the region that contains $MoSi_2$, SiC, and $Mo_xSi_3C_y$. $Mo_xSi_3C_y$ is called the Nowotny phase. The x and y subscripts vary but their dependence is not known.

The first reaction in the $MoSi_2$ powder occurs when it exposed to the O_2 in the atmosphere during powder processing forming an SiO_2 layer on the surface of the powder particles. This reaction can be represented by this chemical reaction,

$$A \, MoSi_2 + B \, O_2 \Rightarrow C \, MoSi_2 + D \, Mo_5Si_3 + E \, SiO_2 \tag{1}$$

where the letters A through E represent the coefficients. The next chemical reaction occurs during sintering and can be written as,

$$C \, MoSi_2 + D \, Mo_5Si_3 + E \, SiO_2 + F \, C \Rightarrow G \, MoSi_2 + H \, SiC + I \, Mo_xSi_3C_y + J \, O_2 \tag{2}$$

where F through J represent the coefficients. The first three products were the compounds determined using Nowotny's ternary phase diagram. Smaller quantities of O

Table A1: Atomic compositions of the powders.

	Weight % C	Atomic % Mo	Atomic % Si	Atomic % C
PRBCSE	1.21	31.7	63.4	4.9
ADF	2.88	29.6	59.2	11.1

were found in the sintered samples with C compared to those without C indicating that the

O was given off in a gaseous form.

A stoichiometric analysis was done to determine the weight percentages of the

solid products. A molar balance was done for each of the elements in EQ. 1. For Mo,

$$A = C + 5D \tag{3}$$

for Si,

$$2A = 2C + 3D + E \tag{4}$$

for O,

$$2B = 2E \tag{5}$$

The number of moles of SiO_2 and $MoSi_2$ in the starting powder can be calculated

assuming that 2.41 wt% O is present in the starting powder from previous research [33].

$$E = \frac{2.41 \text{ g O} \cdot 1 \text{ mol O} \cdot 1 \text{ mol SiO}_2}{16 \text{ g O} \cdot 2 \text{ mol O}} = 0.0753 \text{ mole} \tag{6}$$

After substituting EQ. 3 into EQ. 4 and solving for D,

$$D = \frac{E}{7} = 0.0108 \text{ mole} \tag{7}$$

Doing a mass balance for the remaining powder (ie. $MoSi_2$, Mo_5Si_3 and the Si in the SiO_2),

$$(100 - 2.41) \text{ g} = C \text{ ATW}_{MoSi2} + D \text{ ATW}_{Mo5Si3} + E \text{ ATW}_{Si} \tag{8}$$

where ATW_{MoSi2}, ATW_{Mo5Si3} and ATW_{Si} are the molecular weights of $MoSi_2$, Mo_5Si_3 and

Si, respectively. Solving for C,

$$C = \frac{(100 - 2.41) - D \cdot \text{ATW}_{Mo5Si3} - E \cdot \text{ATW}_{Si}}{\text{ATW}_{MoSi2}} = 0.5878 \text{ mole} \tag{9}$$

After substituting EQ. 6 into EQ. 5,

Table A2: Percentage of phases after oxidation of the $MoSi_2$ powder.

	$MoSi_2$	Mo_5Si_3	SiO_2
wt%	89.4	6.1	4.5
vol%	83.6	4.3	12.1

$$B = E = 0.0753 \text{ mole} \tag{10}$$

substituting EQ. 7 and EQ. 9 into EQ. 3,

$$A = C + 5D = 0.6416 \text{ mole} \tag{11}$$

weight percent of $MoSi_2$, Mo_5Si_3 and SiO_2 can be calculated,

$$wt\%_i = 100 \cdot \frac{MOL_i \cdot ATW_i}{\sum_j MOL_j \cdot ATW_j} \tag{12}$$

where $wt\%_i$ represents the weight percentage of phase i, MOL_i and MOL_j represent the number of moles of phase i and j in the reaction, and ATW_i and ATW_j represents the atomic weight of phase i and j. The volume percent can also be calculated,

$$vol\%_i = 100 \cdot \frac{\dfrac{MOL_i \cdot ATW_i}{\rho_i}}{\sum_j \dfrac{MOL_j \cdot ATW_j}{\rho_j}} \tag{13}$$

where $vol\%$ represents the volume percentage of phase i and ρ_i and ρ_j represent the density of phase i and j respectively. These values have been tabulated in Table A2.

Another stoichiometric analysis was done on the second chemical reaction (EQ. 2) which occurs during sintering. A molar balance is done for all the elements in the reaction. For Mo,

$$C + 5D = G + xI \tag{14}$$

for Si,

$$2C + 3D + E = 2G + H + 3I \tag{15}$$

for C,

$$F = H + yI \tag{16}$$

for O,

$$2E = 2J \tag{17}$$

where x and y are the stoichiometric subscripts in the Nowotny phase compound. The subscripts x and y were assumed to be 4.7 and 0.56, respectively. These values were obtained from a WDS spot analysis. An equation can also be written for the weight percent of C that was added,

$$WTC = 100 \frac{F \cdot ATW_C}{C \cdot ATW_{MoSi2} + D \cdot ATW_{Mo5Si3} + E \cdot ATW_{SiO2} + F \cdot ATW_C} \tag{18}$$

where WTC represents the weight percent C added, and C through F represent the number of moles of each phase. Solving for F,

$$F = \frac{WTC \cdot \left(C \cdot ATW_{MoSi2} + D \cdot ATW_{Mo5Si3} + E \cdot ATW_{SiO2}\right)}{ATW_C \cdot (100 - WTC)} \tag{19}$$

Solving EQ. 16 for H,

$$H = F - yI \tag{20}$$

Substituting EQ. 20 into EQ. 15 and solving for I,

$$I = \frac{2C + 3D + E - 2G - F}{3 - y} \tag{21}$$

Substituting EQ. 21 into EQ. 14 and solving for G,

$$G = \frac{C + 5D - x\left(\dfrac{2C + 3D + E - F}{3 - y}\right)}{1 - \dfrac{2x}{3 - y}} \qquad (22)$$

Solving EQ. 14 for I,

$$I = \frac{C + 5D - G}{x} \qquad (23)$$

EQ. 12 and EQ. 13 were used to calculate the weight and volume percentage for the phases in the sintered samples (ie. $MoSi_2$, SiC, and $Mo_xSi_3C_y$). These values are tabulated in Table A3.

Table A3: Percentage of phases after sintering of the $MoSi_2$ with C for PRBCSE and ADF processed powders.

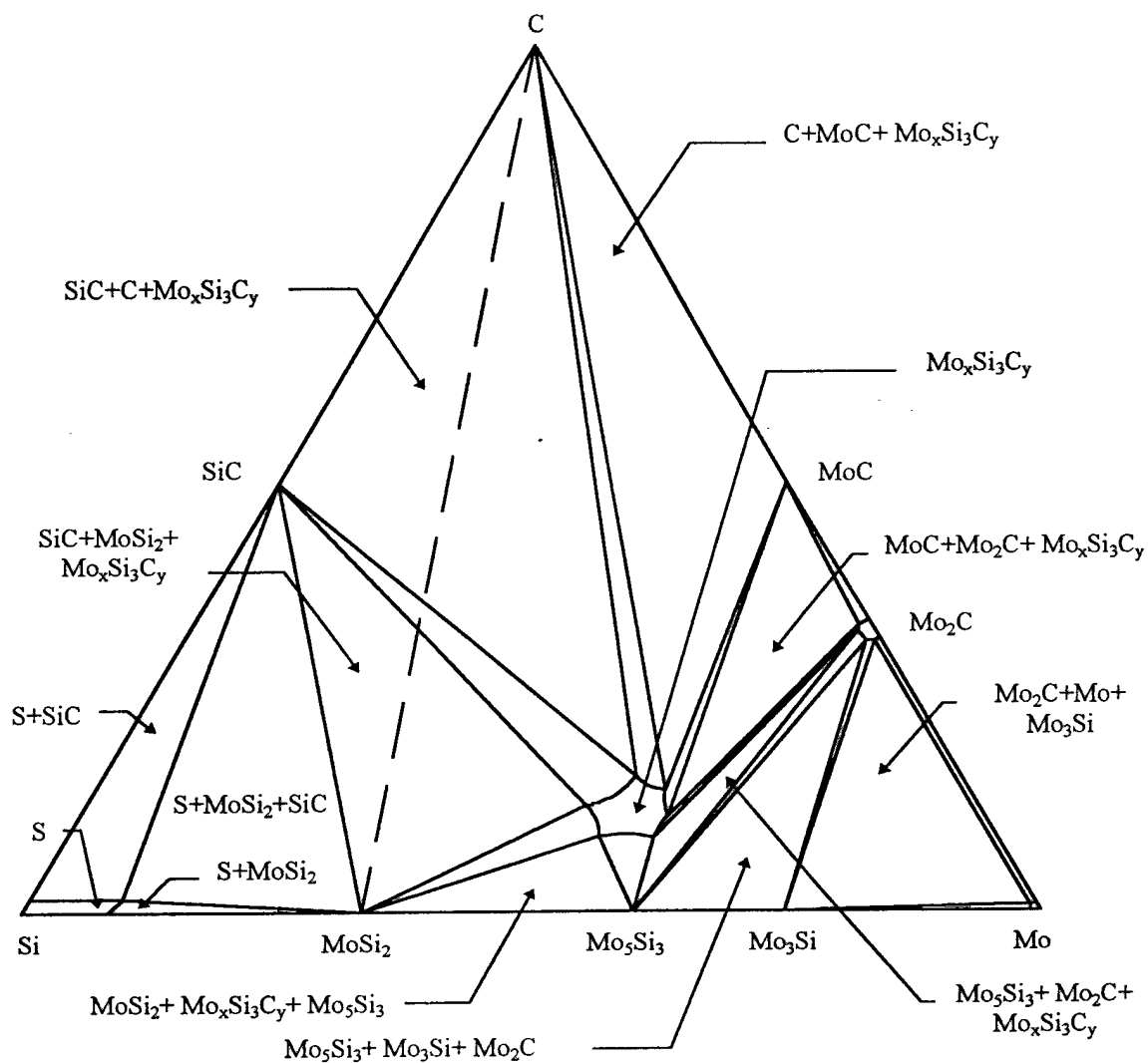|	C (wt%)	$MoSi_2$ vol% (wt%)	SiC vol% (wt%)	$Mo_{\leq 4.8}Si_3C_{\leq 0.6}$ vol% (wt%)
PRBCSE	1.21	86.4 (88.2)	7.3 (3.8)	6.3 (8.0)
ADF	2.88	68.6 (71.8)	16.9 (9.1)	14.5 (19.1)

Figure A1:   Isothermal section of the ternary phase diagram at 1600 °C for the Mo-Si-C system, the dashed line represents the MoSi$_2$-C pseudobinary system [24].

REPORT DOCUMENTATION PAGE

1. AGENCY USE ONLY *(Leave blank)*	2. REPORT DATE April 1, 1997	3. REPORT TYPE AND DATES COVERED Final report covering 5/26/96 – 2/28/97

4. TITLE AND SUBTITLE

Reactively sintered molybdenum disilicide-based composites

5. FUNDING NUMBERS

PR 96 PR 05910-00

6. AUTHOR(S)

K.K. Chawla

7. PERFORMING ORGANIZATION NAMES(S) AND ADDRESS(ES)

New Mexico Tech
801 Leroy Place
Socorro, NM 87801

8. PERFORMING ORGANIZATION REPORT NUMBER

9. SPONSORING / MONITORING AGENCY NAMES(S) AND ADDRESS(ES)

Office of Naval Research
Arlington, VA 22227
Program Manager: Dr. A.K. Vasudevan, code 332

10. SPONSORING / MONITORING AGENCY REPORT NUMBER

11. SUPPLEMENTARY NOTES

a. DISTRIBUTION / AVAILABILITY STATEMENT

APPROVED FOR PUBLIC RELEASE

12. DISTRIBUTION CODE

13. ABSTRACT *(Maximum 200 words)*

The objective of this research was to identify the phases formed and determine some mechanical properties of reactively sintered $MoSi_2$ and $MoSi_2$ composites with carbon additions. The carbon additions were made via polymeric coatings on $MoSi_2$ particles. Carbon was added to form silicon carbide particles (SiC_p) in situ and to reduce the inherent presence of SiO_2 in $MoSi_2$. The in situ formation of SiC_p would increase the low temperature toughness of $MoSi_2$ by using it as a reinforcement and also reduce the high temperature creep by reducing grain boundary sliding caused by viscous flow of SiO_2. The carbon coating of the $MoSi_2$ powder was obtained by: phenolic resin based carbon by solvent evaporation and aqueous dispersion flocculation. The sintering temperatures and times ranged from 1600 to 1800 °C and 1 to 100 h, respectively. The addition of carbon did reduce the presence of SiO_2 and there was formation of SiC_p. However, the SiC_p formation was less than expected and, therefore, did not increase toughness significantly. The Nowotny phase ($Mo_{4.8}Si_3C_{0.6}$) was also found in less than expected amounts.

14. SUBJECT TERMS	15. NUMBER OF PAGES 87
	16. PRICE CODE

17. SECURITY CLASSIFICATION OF REPORT UNCLASSIFIED	18. SECURITY CLASSIFICATION OF THIS PAGE UNCLASSIFIED	19. SECURITY CLASSIFICATION OF ABSTRACT UNCLASSIFIED	20. LIMITATION OF ABSTRACT

GENERAL INSTRUCTIONS FOR COMPLETING SF 298

The Report Documentation Page (RDP) is used in announcing and cataloging reports. It is important that this information be consistent with the rest of the report, particularly the cover and title page. Instructions for filling in each block of the form follow. It is important to *stay within the lines* to meet *optical scanning requirements.*

Block 1. Agency Use Only *(Leave blank).*

Block 2. Report Date. Full publication date including day, month, and year, if available (e.g. 1 Jan 88). Must cite at least the year.

Block 3. Type of Report and Dates Covered. State whether report is interim, final, etc. If applicable, enter inclusive report dates (e.g. 10 June 87 - 30 June 88.

Block 4. Title and Subtitle. A title is taken from the part of the report that provides the most meaningful and complete information. When a report is prepared in more than one volume, repeat the primary title, add volume number, and include subtitle for the specific volume. On classified documents enter the title classification in parentheses.

Block 5. Funding Numbers. To include contract and grant numbers; may include program element number(s), project number(s), task number(s), and work unit number(s). Use the following labels:

C -	Contract	**PR** -	Project
G -	Grant	**TA** -	Task
PE -	Program Element	**WU** -	Work Unit Accession No.

Block 6. Author(s). Name(s) of person(s) responsible for writing the report, performing the research, or credited with the content of the report. If editor or compiler, this should follow the name(s).

Block 7. Performing Organization Name(s) and Address(es). Self-explanatory.

Block 8. Performing Organization Report Number. Enter the unique alphanumeric report number(s) assigned by the organization performing the report.

Block 9. Sponsoring/Monitoring Agency Names(s) and Address(es). Self-explanatory.

Block 10. Sponsoring/Monitoring Agency Report Number. *(If known)*

Block 11. Supplementary Notes. Enter information not included elsewhere such as: Prepared in cooperation with...; Trans. of ...; To be published... When a report is revised, include a statement whether the new report supersedes or supplements the older report.

Block 12a. Distribution/Availability Statement. Denotes public availability or limitations. Cite any availability to the public. Enter additional limitations or special markings in all capitals (e.g. **NOFORN, REL, ITAR**).

DOD	-	See DODD 5230.24, "Distribution Statements on Technical Documents."
DOE	-	See authorities.
NASA	-	See Handbook NHB 2200.2.
NTIS	-	Leave blank.

Block 12b. Distribution Code.

DOD	-	Leave blank.
DOE	-	Enter DOE distribution categories from the Standard Distribution for Unclassified Scientific and Technical Reports.
NASA	-	Leave blank.
NTIS	-	Leave blank.

Block 13. Abstract. Include a brief *(Maximum 200 words)* factual summary of the most significant information contained in the report.

Block 14. Subject Terms. Keyword or phrases identifying major subjects in the report.

Block 15. Number of Pages. Enter the total number of pages.

Block 16. Price Code. Enter appropriate price code *(NTIS only).*

Blocks 17. - 19. Security Classification. Self-explanatory. Enter U. S. Security Classification in accordance with the U.S. Security Regulations (i.e., UNCLASSIFIED). If form contains classified information, stamp classification on the top and bottom of the page.

Block 20. Limitation of Abstract. This block must be completed to assign a limitation to the abstract. Enter either UL (unlimited) or SAR (same as report). An entry in this block is necessary if the abstract is to be limited. If blank, the abstract is assumed to be unlimited.